

FAKULTÄT FÜR MASCHINENWESEN

DER TECHNISCHEN UNIVERSITÄT MÜNCHEN

Promotion in Luft- und Raumfahrt

**Development of a Rocket Engine Injection
System with Throttling Capability Based on
the LO_2/LCH_4 Propellant Combination**

Brunno Barreto Vasques

Vollständiger Abdruck der von der Fakultät für Maschinenwesen der Technischen Universität München zur Erlangung des akademischen Grades eines

Doktor-Ingenieurs (Dr.-Ing.)

genehmigten Dissertation.

Vorsitzender:

Prof. Dr.-Ing. Hans-Jakob Kaltenbach

Prüfer der Dissertation:

1. Prof. Dr.-Ing. Oskar J. Haidn

2. Prof. Dr.-Ing. Stefan Schleichtriem

Die Dissertation wurde am 27.02.2018 bei der Technischen Universität München eingereicht und durch die Fakultät für Maschinenwesen am 30.01.2019 angenommen.

Não tenhas nada nas mãos
Nem uma memória na alma,
Que quando te puserem
Nas mãos o óbolo último,
Ao abrirem-te as mãos
Nada te cairá.
Que trono te querem dar
Que Átropos to não tire?
Que louros que não fanem
Nos arbítrios de Minos?
Que horas que te não tornem
Da estatura da sombra
Que serás quando fores
Na noite e ao fim da estrada.
Colhe as flores mas larga-as,
Das mãos mal as olhaste.
Senta-te ao sol. Abdica
E sê rei de ti próprio.

– Fernando Pessoa

Abstract

Liquid oxygen and liquid methane are leading options for space propulsion systems requiring high propellant bulk density, low-toxicity and similar thermal management characteristics. For the majority of applications, the benefit resulting from smaller, lighter tanks and low boil-off losses counterweight the disadvantage in terms of theoretical specific impulse, for instance if compared to the liquid oxygen/liquid hydrogen propellant combination. Compared to highly toxic space storable propellants, such as N_2O_4 and UDMH, oxygen and methane can be more easily handled, leading to a substantial reduction in the operational costs. Besides, due to the presence of methane in the Martian atmosphere, the possibility of in-situ production through, e.g. the Sabatier process, for long duration missions is envisioned.

Of particular interest are those missions involving planetary landing and orbit maneuvers, which usually impose a degree of thrust modulation capability over the propulsion system. Strictly from the standpoint of the thrust chamber injection system, the pintle injector is an attractive choice in this case, due to its inherent combustion stability characteristics, proven design and simple manufacture. Having being qualified for use with storable, hypergolic propellants, very little design criteria is available for design of pintle type injectors for rocket engines running on LO_2/LCH_4 propellants.

A combustion performance experimental investigation was conducted with the objective of filling this gap. The variables investigated were injector (1) skip distance, (2) LO_2 orifice shape, and (3) injection angle of the annular fuel sheet. Tests were made using a 50-[mm] diameter heat-sink combustor at chamber pressures between 0.5 and 1.5 [MPa] and over the range of circa 2 to 4 oxidizer-to-fuel mixture ratios. The experimental hot-firing effort was undertaken in two parts. First, the baseline injector design characteristics were investigated with the primary goal of assessing chamber ignition characteristics and test stand operation. In the second part, injector design modifications were implemented, both to examine injector durability and performance effects. Characteristic velocities of 80% to 92% were measured totaling six injector versions and two combustion chamber configurations with different combustor lengths and contraction ratios, resulting in each case in an approximately equal characteristic length L^* of 1.50 [m]. All injector configurations were cold-flow tested using water as simulants to measure spray angle and compute the discharge coefficients, and to allow for comparison with hot-firing data. A description of the miniature cryogenic test stand designed and built for the injector characterization is provided as well as the methods used for propellant production, flow measurement and temperature conditioning.

A survey of mission requirements in terms of engine throttling ratio, burn duration, number of burns, ΔV and thrust program for various applications is presented. For the pre-

sent research, the mission model defining basic propulsion system requirements was established on the basis of an unmanned Mars soft-landing vehicle. Analytical studies defining descent propulsion system delivered performance employing single- and dual- propellant regenerative cooled thrust chambers as well as fuel film-cooling are presented with a qualitative discussion of applicable engine cycles. A discussion of the methods to achieve the required thrust modulation is introduced, together with the advantages and disadvantages of each concept, and with use of a decision matrix to gauge their relative merit. A design procedure for pintle type elements is described, along with the design features of the series of pintle injectors that were tested. The injector design changes implemented in this research resulted in excellent overall injector durability and reasonable characteristic combustion efficiency η_{C^*} at the design mixture ratio. The present effort also helped establish an empirical knowledge base for future throttling injector development studies.

Zusammenfassung

Flüssiger Sauerstoff und flüssiges Methan sind führende Optionen für Raumfahrt Antriebssysteme, die eine hohe Treibstoffdichte, geringe Toxizität und gute thermische Eigenschaften erfordern. Der Vorteil kleinerer, leichter Treibstofftanks gleicht den Nachteil eines geringen spezifischen Impulses aus, etwa im Vergleich zur Kombination flüssiger Sauerstoff und flüssiger Wasserstoff. Im Vergleich zu hochgiftigen lagerfähigen Treibstoffen wie N_2O_4 und UDMH können Sauerstoff und Methan leichter gehandhabt werden, was zu einer erheblichen Senkung der Betriebskosten führt. Aufgrund des Vorhandenseins von Methan in der Marsatmosphäre besteht außerdem die Möglichkeit einer in-situ-Produktion für Langzeitmissionen, die beispielsweise den Sabatier-Prozess verwenden. Von besonderem Interesse sind die Missionen, die planetare Lande- und Orbit-Manöver beinhalten, die normalerweise eine gewisse Schubmodulationsfähigkeit über das Antriebssystem auferlegen. Streng vom Standpunkt des Einspritzsystems aus betrachtet, ist der Pintle-Injektor in diesem Fall aufgrund seiner charakteristischen Verbrennungsstabilität, bewährten Konstruktion und einfachen Herstellung eine attraktive Wahl. Da diese Einspritzelemente am meisten für die Anwendung mit lagerfähigen, hypergolischen Treibstoffen qualifiziert wurden, sind sehr wenige Entwurfskriterien für die Konstruktion von Injektoren des Pintle-Typs für Raketentriebwerke verfügbar, die mit LO_2 und LCH_4 betrieben werden.

Eine experimentelle Untersuchung der Verbrennungsleistung wurde mit dem Ziel durchgeführt, diese Lücke zu schließen. Die untersuchten Variablen waren (1) der sogenannte "skip distance" des Injektors, (2) die Form der LO_2 Öffnung und (3) der Einspritzwinkel der ringförmigen Brennstoffplatte. Die Experimente wurden unter Verwendung einer kapazitiven Brennkammer mit 50 [mm] Innendurchmesser in einem Betriebsbereich zwischen 0,5 und 1,5 [MPa] Brennkammerdrücke und Verhältnis von Oxidationsmittel zu Brennstoffgemisch von etwa 2 bis 4 durchgeführt. Die experimentelle Heißtests wurden in zwei Teilen durchgeführt. Zuerst wurden die Konstruktionsmerkmale der Basiskonfiguration untersucht mit dem Hauptziel, Kammerentzündungseigenschaften und Prüfstandbetrieb zu bewerten. Im zweiten Teil wurden Variationen von konstruktiven Details am Basis Injektordesign implementiert, um sowohl die Auswirkungen auf Lebensdauer des Einspritzelementes als auch auf dem Verbrennungswirkungsgrad zu untersuchen. Es wurden Verbrennungswirkungsgrade von 80% bis 92% gemessen, insgesamt sechs Injektorversionen und zwei Brennkammerkonfigurationen mit unterschiedlichen Brennkammerlängen und Kontraktionsverhältnissen, die jeweils zu einer annähernd gleichen charakteristischen Länge L^* von 1,50 [m] führten. Alle Injektorconfigurationen wurden durch Wassertests charakterisiert zur Messung des Sprühwinkels und zur Berechnung der Durchflusskoeffizienten zwecks Abstimmung mit den Verbrennungsversuchen. Eine Beschreibung des für die

Injektorcharakterisierung konzipierten und gebauten Miniatur-Tieftemperaturteststandes sowie der Verfahren zur kryogenen Treibstoffherstellung, Durchflussmessung und Temperaturkonditionierung wird gegeben.

Eine Übersicht der Missionsanforderungen in Bezug auf Regelbarkeit, Brenndauer, Anzahl der Verbrennungen, Geschwindigkeitsvariation ΔV und Schubprogramm für verschiedene Anwendungen wird vorgestellt. Für die vorliegende Forschung wurde das Missionsmodell, das die grundlegenden Anforderungen an das Antriebssystem definiert, auf der Basis einer unbemannten Mars-Mission festgelegt.

Das Weiteren wurden analytische Studien vorgestellt, die die Leistungsfähigkeit des Antriebssystems unter Verwendung verschiedener regenerativen Kühlkonzepte sowie Film Kühlung definieren mit einer qualitativen Diskussion über die anwendbaren Antriebskonzepte für Treibstoffförderung. Eine Übersicht über die Methoden zur Erreichung der erforderlichen Schubmodulation wurde ebenfalls gegeben. Die Auslegungsmethoden von Pintle-Injektoren wurden beschrieben, zusammen mit den Konstruktionsmerkmalen der Reihe von untersuchten Konfigurationen.

Das Design der Injektoren und deren Modifikationen, die in diesem Forschungsprojekt implementiert wurden, führten zu einer ausgezeichneten Injektorhaltbarkeit und einem vernünftigen Verbrennungswirkungsgrad η_{C^*} bei dem geforderten Konstruktion Mischungsverhältnis. Die vorliegende Arbeit unterstützte ebenso, eine empirische Wissensbasis für zukünftige Studien zur Entwicklung von Injektoren für regelbare Raketentriebwerke.

Nomenclature

a	Velocity of a Disturbance, [m/s]
A	Area, [m ²]
A	Geometric Constant of Swirl Atomizers, [-]
B	Bias Error
BF	Blockage Factor, [-]
Bi	Biot Number, [-]
C	Specific Heat, [J/kg K]
C_d	Discharge Coefficient, [-]
D	Diameter, [m]
d	Orifice Diameter, [m]
dh	Differential Height
dt	Differential Time
f	Friction or Correction Factor, [-]
f_k	Contraction Ratio, [-]
F	Force, [N]
F_o	Fourier Number, [-]
g	Gravitational Acceleration, [$\frac{m}{s^2}$]
H	Enthalpy, [J/kg]
h	Height, [m]
h	Heat Transfer Coefficient, [W/m ² K]
I	Ito Parameter, [-]
I_{sp}	Specific Impulse, [$\frac{m}{s}$]
I_t	Total Impulse, [N·s]
K	Mass coefficient, [-]
K_m	Oxidizer-to-Fuel Mixture Ratio (O/F), [-]
K_{mn}	Initial Oxidizer-to-Fuel Mixture Ratio (O/F), [-]
K_p	Thrust Coefficient, [-]
k	Conductivity, [W/m·K]
L	Length, [m]
L_{mix}	Mixing Length, [m]
L^*	Characteristic Length, [m]
m	Mass, [kg]
\dot{m}	Mass flow rate, [kg/s]
M	Momentum, [N]
Ma	Mach Number, [-]

Nu	Nusselt Number, [-]
\dot{m}	Mass Flow Rate, $\left[\frac{\text{kg}}{\text{s}}\right]$
n	Number of Tangential Channels, [-]
N	Number of Orifices or Number of Samples, [-]
p	Pressure, $\left[\frac{\text{N}}{\text{m}^2}\right]$
P	Thrust, [N]
Pr	Prandtl Number, [-]
\dot{q}	Local Heat Flux, $[\text{W}/\text{m}^2]$
Q	Heat Rate, [W]
R	Radial Location, [m]
Re	Reynolds Number, [-]
St	Stanton Number, [-]
r	Radius, [m]
r	Recovery Factor, [-]
s	Specific Entropy, $[\text{J}/\text{kg}\cdot\text{K}]$
S	Precision Index, [-]
S	Distance between Adjacent Orifices, [m]
T	Temperature, [K]
t	Thickness, [m]
t	Time, [s]
t_{95}	t-Student's Parameter
TMR	Momentum Ratio (O/F), [-]
U	Velocity, $\left[\frac{\text{m}}{\text{s}}\right]$
U	Uncertainty, [-]
V	Injection Velocity, $\left[\frac{\text{m}}{\text{s}}\right]$
W	Width, [m]
x	Segment Length, [m]
X	Parameter in a Sample
Z	Axial Distance, [m]

Greek Letters

α	Spray Cone Half-Angle, [degrees]
α	Thermal Diffusivity of Plate Material, $[\text{m}^2/\text{s}]$
β	Line Contraction, [-]
Δ	Differential
Δp	Pressure Drop, [Pa]
ΔV	Velocity Change, [m/s]
δ	Throttling Ratio, [-]
ϵ	Coating Emissivity, [-]
η	Efficiency, [-]
θ	Thickness or Influence Coefficient, [-]
μ	Dynamic Viscosity, $[\text{Pa}\cdot\text{s}]$
ξ	Coefficient for Frictional Losses, [-]
κ	Thermodynamic Property

π	Pi, (≈ 3.1415)
ν	Degree of Freedom
ρ	Fluid Density, $\left[\frac{\text{kg}}{\text{m}^3}\right]$
σ	Stefan-Boltzmann Constant, $5.67 \cdot 10^{-8}$, $[\text{W}/\text{m}^2 \cdot \text{K}^4]$
ϕ	Correction Factor, [-]
Ψ	Turbulent Mixing Coefficient, [-]

Subscripts

0	Stagnation
1	Upstream conditions or First Swirl Atomizer Stage
1D	One-dimensional
2	Outlet or Second Swirl Atomizer Stage
3	Third Swirl Atomizer Stage
4	Fourth Swirl Atomizer Stage
2D	Two-dimensional
av	Average
aw	Adiabatic
BO	Burn-out
c	Curved, Coolant or Core
ch	Tangential Channel
d	Dynamic
div	Divergence
e	Exit, Empty, Earth or Enhanced
eng	Engine
eq	Equivalent
equip	Equipment
exp	Experimental
f	Fuel or Friction
g	Gas
H	Atmospheric
h	Heat, Horizontal or Hydraulic
i	i th Parameter
id	Ideal Condition
inj	Injector
in	Inlet or Input
k	Chamber
kin	Kinetics
kp	Critical
l	Liquid
m	Mars or momentum
max	Maximum
min	Minimum
n	Nozzle
num	Numerical

<i>o</i>	Stagnation condition, Initial or Oxidizer
<i>out</i>	Outlet
<i>p</i>	Propellant, Pressure
<i>r</i>	Radial Direction
<i>ref</i>	Reference
<i>s</i>	Straight
<i>sat</i>	Saturation
<i>sub</i>	Subcooled
<i>T</i>	Total
<i>tc</i>	Thrust Chamber
<i>theo</i>	Theoretical
<i>v</i>	Vertical or Vaporization
<i>vac</i>	Vacuum
<i>visc</i>	Viscous
<i>w</i>	Wall
<i>z</i>	Zonal

Contents

Abstract	iii
Zusammenfassung	v
Nomenclature	vii
Outline of the Thesis	xv
I. Introduction	1
1. Introduction	3
1.1. Problem Statement	3
1.1.1. Why LO ₂ /LCH ₄ ?	3
1.2. Status of Technology	5
1.3. Scope and Research Goals	5
2. Literature Review	6
2.1. Literature on Green Propellants	6
2.2. Literature Review on Throttling Rocket Engines	7
2.3. Relevant Literature on Injectors for Thrust Variations	9
2.3.1. Fixed-Area Swirl Injectors	9
2.3.2. Variable-Area Injectors	11
2.3.3. Experimental Investigations	13
2.3.4. Other Types of Injectors for Thrust Variations	14
II. Requirements Definition	15
3. Mission Requirements	17
3.1. Mission Characteristics	17
3.2. Mars Lander Requirements	18
3.2.1. Assumptions	18
3.3. Thrust Level Selection Based on Payload Optimization	19
3.3.1. Basic Assumptions and Equations	20
3.3.2. Relative Payload Determination	20
3.4. Conclusions	24
4. Propulsion System Concept Selection	27
4.1. Propellant Properties and Theoretical Performance	27

4.2.	Assumptions for the Attainable I_{sp}	27
4.3.	Thrust Chamber Cooling Analysis	29
4.3.1.	Baseline Engine Contour	30
4.3.2.	Gas-side heat transfer	30
4.3.3.	Radiation Cooling Analysis	33
4.3.4.	Regenerative Cooling Analysis	33
4.3.5.	Film-Cooling Analysis	40
4.4.	Performance Sensitivity	45
4.5.	Applicable Engine Cycle	45
4.6.	Thermal Analysis Summary	46
4.6.1.	Final System Recommendation	47
 III. Throttling Concept Selection		55
 5. Potential Throttling Concepts		57
5.1.	Background	57
5.1.1.	Methods of Rocket Engine Throttling	57
5.2.	Throttling Concept Candidates	61
5.2.1.	Flow Control	61
5.2.2.	Injectors	62
5.3.	Design Concept Comparison and Selection	69
5.3.1.	Discussion and Recommendation	71
5.4.	Conclusions	71
 IV. System Design		72
 6. Hardware Design and Description		74
6.1.	Injector Design	74
6.1.1.	Injection and Combustion Design Considerations	75
6.1.2.	Design Criteria	76
6.1.3.	Design Summary	80
6.1.4.	Sensitivity Analysis	83
6.1.5.	Injector Manufacturing and Assembly	83
6.1.6.	Instrumentation	84
6.2.	Experimental Thrust Chamber Design	84
6.2.1.	General	84
6.2.2.	Instrumentation	88
 V. Experimental Approach		89
 7. Experimental Results		91
7.1.	Injector Cold-Flow Studies	91
7.1.1.	Hydraulic Characteristics	91
7.1.2.	Use of the Mechanical Patternator Technique	95

7.2. Injector Hot-Fire Characterization	96
7.2.1. Experimental Facility	96
7.2.2. Basic Pintle Injector Development	102
7.2.3. Injector Modifications	112
7.3. Conclusions	120
VI. Conclusions and Future Work	123
8. Conclusions and Recommendations	125
8.1. Analytical Results	125
8.2. Experimental Results	125
8.2.1. Operating Conditions	126
8.3. Future Research	126
Appendix	130
A. Propellant Physical and Transport Properties	130
A.1. Liquid Oxygen Physical and Transport Properties	130
A.2. Liquid Methane Physical and Transport Properties	130
B. Computer Routines	131
B.1. Computer Program for Thrust Chamber Cooling Analyses	131
B.1.1. Input-Output Subroutines	131
B.1.2. System Subroutines	131
B.1.3. Data-Handling Subroutines	131
B.2. One-Dimensional REGEN Code Listing	132
C. Calculation of Characteristic Velocity Efficiency	141
C.1. Methods of Computation	141
C.1.1. Chamber Pressure Method	141
C.1.2. Calculations Based on Thrust	142
D. Mass Flow Computation from Venturi Meter Measurements	143
D.1. Data Reduction Procedure	143
E. Uncertainty Analysis	145
E.1. Total Uncertainty of a Measurement	146
E.1.1. Characteristic Velocity	146
E.1.2. Discharge Coefficient from Cold-Flow Tests	149
F. Test Instrumentation	151
F.1. Hot-Fire Test Instrumentation	151
G. Injector Hardware	154
G.1. Injector hardware	154

Outline of the Thesis

Part I: Introduction and Literature Search

CHAPTER 1: INTRODUCTION

This chapter presents an overview of the thesis and its scope.

CHAPTER 2: LITERATURE REVIEW

This chapter presents pertinent literature on the various aspects of rocket engine throttling, flow control techniques, liquid oxygen and methane propellant applications and recent research in the area of injector technology applicable to engine thrust variations.

Part II: Requirements Definition

CHAPTER 3: MISSION CHARACTERISTICS

The chapter acquaints the reader with the mission model, vehicle and propulsion system features. Propulsion system requirements are discussed in terms of thrust level, thrust-to-weight ratio and thrust modulation.

CHAPTER 4: PROPULSION SYSTEM CONCEPT SELECTION

Based on mission analysis and requirements, propulsion system conceptual studies were conducted. Studies were performed to determine thrust chamber cooling limits, using both regenerative and film cooling. Coolant passage geometry and wall temperature data was calculated for selected thrust chamber configurations. Candidate engine cycles are recommended for further study.

Part III: Throttling Concept Selection

CHAPTER 5: POTENTIAL THROTTLING CONCEPTS

This chapter presents a discussion of rocket engine throttling methods applicable to the proposed mission model and propulsion system concept. Criteria is established to aid in the final throttling concept selection.

Part IV: System Design

CHAPTER 6: HARDWARE DESIGN AND DESCRIPTION

This chapter details the design process for pintle injectors and presents a summary of dimensional suggestions from various sources, along with a description of all injector configurations tested. An overview of the hardware designed for the hot-fire experimental effort is provided.

Part V: Experimental Approach

CHAPTER 7: EXPERIMENTAL RESULTS

This chapter provides an account of the cold-flow experiments conducted with all pin-tle injector configurations. The experiments collected basic hydraulic information such as spray angle and injector discharge coefficients. A discussion of the designed miniature cryogenic test facility is provided. Hot-fire results are then presented in terms of characteristic velocity efficiency as a function of mixture ratio and injection force and velocity ratios.

Part VI: Conclusions and Future Work

CHAPTER 8: CONCLUSIONS AND RECOMMENDATIONS

This chapter sets a more detailed discussion of results and additional recommendations for future work.

Bibliography

Appendices

Part I.

Introduction

1. Introduction

1.1. Problem Statement

Historically, cryogenic rocket engines have not been used for long term in-space applications due to their complexity, the mission requirement for high reliability and the challenges associated with propellant boil-off and ignition. On the other hand, cryogenic rocket engines offer the potential for higher performance and greater mission flexibility.

1.1.1. Why LO₂/LCH₄?

It is appropriate to consider the reasons for the LO₂/LCH₄ propellant selection. In Figure 1.1, specific impulse is plotted as a function of the bulk density of the propellant combination for a number of combinations. Specific impulse is a figure of merit much like

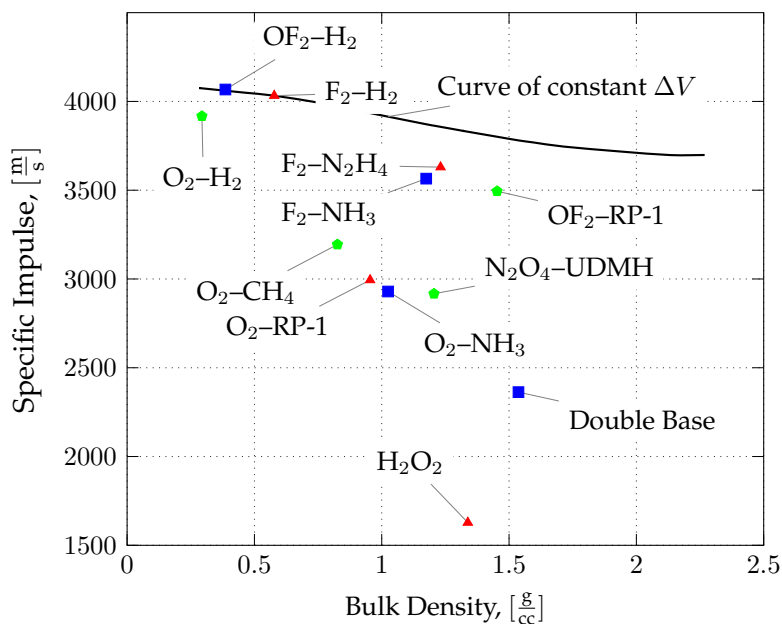


Figure 1.1.: Performance characteristics of typical propellant combinations.

gas mileage of an automobile. It is equal to the thrust produced for each kilogram-per-second of propellant flow. It will be seen that the maximum values of specific impulse are achieved with OF₂-H₂ and F₂-H₂, followed by O₂-H₂. These propellant combinations are, of course, of considerable interest since they give significantly higher values of impulse than the O₂-RP-1 used in the *Soyuz* or the N₂O₄-UDMH currently used in the *Proton*.

1. Introduction

By itself, however, specific impulse is not a singular figure of merit – other factors must be considered, such as the bulk density shown in the abscissa. The overall objective of a missile stage is to impart a maximum change in velocity to the stage and its payload. The expression relating these factors is:

$$\Delta V = I_{sp} \ln \left(\frac{m_o}{m_e} \right). \quad (1.1)$$

where:

- ΔV = velocity change, $\left[\frac{\text{m}}{\text{s}} \right]$;
- I_{sp} = specific impulse, $\left[\frac{\text{m}}{\text{s}} \right]$;
- m_o = mass of stage loaded with propellant, [kg];
- m_e = empty mass (at burnout), [kg].

Inspection of this equation shows that the velocity can be increased by increasing specific impulse, but also, it can be increased by decreasing the vehicle empty weight or structural weight. In this regard then, the use of higher density propellants will result in smaller propellant tanks and, hence, a lower structural weight. The trade-off between specific impulse and bulk density is indicated in Figure 1.1 by the curve of constant ΔV . From this, it may be seen that $\text{F}_2\text{-H}_2$ will produce a greater velocity change than will $\text{OF}_2\text{-RP-1}$ (for an equal velocity change, $\text{OF}_2\text{-RP-1}$ would have to show a specific impulse of 380 seconds instead of 350). Thus, the ΔV produced is not simply given by the ratio of the specific impulse values, but is also affected by the bulk density.

With $\text{O}_2\text{-CH}_4$ the specific impulse can be in relation to $\text{O}_2\text{-RP-1}$ only about 200 to 300 [m/s] higher, resulting in a system that is probably slightly heavier. The temperature interval in which methane can be maintained as a liquid is only ca. 20 [K]. Does that gain in specific impulse compensate for the extra complexity associated with the handling of a cryogenic fluid like methane? The answer is probably *no* for most of the booster applications. The advantages of methane as a fuel seem to lie more over hydrogen than over kerosene. Because of the low density of hydrogen, tank volumes are smaller with methane and the pump power required decreases. Moreover, for long missions to the Moon and Mars LO_2/LCH_4 has favorable characteristics for long storage time and re-usability when compared to hydrogen/oxygen engines. Some of these characteristics are listed below:

1. Non-toxic, non-corrosive and self-venting;
2. Storage temperatures for oxygen and methane allow for a common propellant tank bulkhead or simplified propellant tank interface, reducing vehicle structural weight;
3. No extensive decontamination process required as compared with toxic propellants, such as UDMH and NTO;
4. High vapor pressure supporting good vacuum ignition characteristics;
5. Superior performance than currently used earth storable propellants.

The possibility of in-situ production places methane as the preferred fuel on Mars. Other hydrocarbon fuels such as methanol, ethanol and aromatic hydrocarbon blends can also possibly be produced on Mars, but most studies and technology development activities

have focused on methane [1]. Despite the aforementioned advantages, cryogenic storage in space still poses some problems. These issues might be partly remedied by, for example, passive techniques, such as shielding and spacecraft orientation, or active means, such as refrigeration to keep propellants within the liquid range. Additionally, among all hydrocarbon fuels, methane possesses the lowest heat capacity as a liquid. As a result, regenerative cooling can only be effected at supercritical pressures (above ca. 45.8 [MPa] for methane) where problems of boiling heat transfer can be avoided.

1.2. Status of Technology

Interest in methane as a rocket fuel is not new - at least in Russia, where the propellant has been studied since the late 1940s by Glushko [1]. A summary of recent development efforts is presented in Table 1.1.

Table 1.1.: Recent liquid rocket engine developments based on the oxygen/methane propellant combination.

Propulsion system	Raptor	BE-4	ACE-42R	LE-8	MIRA
Country	USA	USA	France	Japan	Italy
Organization	SpaceX	Blue Origin	ESA/CNES	JAXA	Avio
Vehicle	-	Vulcan	Spaceplane	-	VEGA
Thrust, [kN]	3500	2500	420	107	98
Specific impulse (vacuum), [s]	382	330	340	315	364
Engine cycle	Full-flow staged-combustion	Staged-combustion	Gas-generator	Gas-generator	Expander
Chamber cooling approach	Regenerative	Regenerative	Regenerative	Ablative	Regenerative

1.3. Scope and Research Goals

This research devotes attention to the development of injection systems based on the LO_2/LCH_4 propellant combination and that additionally offer the potential throttling capability required by planetary landing missions. The primary goal of this research is to broaden the injector technology and to establish engineering database for developing a variable thrust oxygen/methane propulsion system that will deliver:

1. Stable operation;
2. Wide thrust range;
3. High combustion performance.

2. Literature Review

The literature review was divided in three parts: first an overview on the application of green propellants is given, followed by an outline of throttling rocket engine developments. Finally, the area regarding injectors for thrust variations is reviewed in more detail.

2.1. Literature on Green Propellants

Based on various past studies [2], [3] and [4], green propellant combinations such as liquid oxygen and liquid methane have been identified as promising options for some future space vehicle systems. To date, the application of the LO₂/methane bi-propellant combination in the low-thrust level range assumes a position in a Technology Readiness Level scale of 6 (TRL 6) [5]. As an example, in the East, prototype engines have been hot-fire tested and their performance demonstrated by the Russians (KBKha RD-0146 engine) and in the West, by the Americans [6], but no developed propulsion system has yet been flown in space. Previous studies [4] demonstrated the applicability of methane regenerative cooling and methane-film cooling to rocket engines in the 445 [N] to 13000 [N] thrust range and chamber pressures from 150 to 6800 [kPa]. Here, the study revealed limitations of the regenerative cooled and film-cooled concepts due to the operating criteria, which required that channel sizes meet minimum dimensional size and were thus limited to the, then, state-of-the-art fabrication limits.

Wesley and colleagues [7] present various conceptual studies for liquid methane densification systems intended for the cryogenic ascent stage of a lunar lander vehicle. A trade study was carried out to assess the most suitable method of producing, filling and conditioning the subcooled, densified liquid methane onboard the spacecraft, with special consideration to ground equipment and associated operations.

Kozlov [8] presented in an unpublished report, the application of various green propellant combinations, including hydrogen peroxide and kerosene, oxygen and ethanol and hydrogen and oxygen. The selection of the most suitable propellant combination is determined in terms of the ballistic efficiency of the particular propellant combination. The ballistic efficiency weighs both the specific impulse and vehicle mass, using the well-known Tsiolkovskii equation. In this work are also presented new perspectives in the area of resonance and glow ignition, as well as the application of vacuum bonding techniques to injector head manufacturing.

A study conducted by Orton and Mark [9] is an example of the early effort to define the most attractive liquid oxygen and hydrocarbon fuel suitable to replace the toxic OMS and RCS of the Space Shuttle. Under the same constraints of packaging and mission profiles of the toxic OMS-RCS counterpart, four candidate fuels were considered, with ethanol and methane offering best system advantages. Both RCS fuels were to be fed through use of electric pumps. The OMS system was assessed in terms of a gas-generator cycle with

ethanol as a fuel and as an expander cycle with methane. The study concluded that ethanol affords the highest ΔV and total impulse due to its high bulk density. Methane provides the lowest system wet-weight and is the preferred fuel, when the system is sized for a fixed ΔV and total impulse requirement (highest payload capability).

Another early study by Martin [10] investigated the potential of hydrocarbon propulsion systems, namely RP-1, methane and propane in combination with liquid oxygen for application in single-stage-to-orbit vehicles. In this particular study, the dry-mass of the vehicle is used as the characteristic to be minimized. Based on this criterion, propane presented somewhat better performance than RP-1 and is considerably better than methane. In addition, staged-combustion cycles with oxidizer reach preburners and oxygen cooling of the thrust chamber presented better weight reducing potential than a fuel rich preburner or fuel cooling.

Zurbach and colleagues [11] describe early research and technological advances of a program called VOLGA, whose objective was the conception of a LO_2/LCH_4 engine for RLV or large liquid reusable booster applications. A discussion of the differences in combustion and injection characteristics between LO_2/LH_2 and LO_2/LCH_4 is briefly presented. Experimental activities were conducted in a subscale combustor using single-element injectors, aimed at preburner development. Theoretical studies involved at the time the modelling of LO_2/LCH_4 turbulent combustion, for prediction of temperature and density fields.

Another project whose objective was the development of propulsion system technologies for non-toxic propellants was conducted by Smith et al. [12]. The Propulsion and Cryogenics Advanced Development (PCAD) emphasized on thruster designs, ascent main engines and descent engines for lunar missions, focusing primarily on ignition and performance testing. A lunar descent engine was envisioned using LO_2/LH_2 and a ascent stage and reaction control system (RCS) with LO_2/LCH_4 was selected. The oxygen-hydrogen engine for the lunar module descent stage provides throttling capability by utilizing similar technology of its predecessor RL-10 engine, and employing a pintle injector. Some problems encountered in the (RCS) development were those related to cooling-channel flow instability due to sub-critical LCH_4 conditions. For the LO_2/LH_2 engine, the nucleate boiling in the injection manifolds led to low-frequency combustion instabilities ("chug") during the low-thrust regime. This was remedied by use of thermal barrier coating on the oxygen side of the inner propellant manifold.

Envisioning savings in both performance and safety over traditional hypergolic propellants, Melcher and Allfred [13] conducted a series of altitude simulated tests employing LO_2 /methane and the RS-18 lunar ascent engine hardware adapted to operate with cryogenics. The objectives were to collect vacuum ignition data on torch and pyrotechnic igniters and provide nozzle kinetics data to support numerical simulations.

2.2. Literature Review on Throttling Rocket Engines

Throttling was originally incorporated in the early 1930s primarily for control of aircraft rocket engines [14]. A detailed survey of liquid rocket engine throttling established around engines from the United States is provided by reference [15]. In this paper several throttling methods are discussed. Dressler [16] also describes nine methods that have been

2. Literature Review

used in the control of liquid rocket thrust, focusing on the key technological features of the Lunar Module Descent Engine (LMDE). During the 1970s, the requirements of space storability, high specific impulse, high bulk density and hypergolicity have directed attention to the FLOX/methane propellant combination for use in upper stage propulsion systems, as described in reference [17]. This study indicated that a propulsion system for deep space missions should be designed to be pump-fed, have a regeneratively cooled combustion chamber, deliver a nominal 22.24 [kN] thrust at an absolute chamber pressure of 3.448 [MPa] and have a 10 to 1 throttling range capability. The mentioned research was probably one of the first efforts made to broaden the throttling technology with regard to combustor performance characteristics, materials compatibility, fabrication techniques and system operating experience with this propellant combination. Performance evaluation criteria included combustion efficiency and stability. More recently, Betts [18] conducted a research aimed at validating a workable LO_2 /methane turbopump-fed rocket for a Mars lander with a 10:1 thrust ratio capacity. In this analytical study, chamber pressure was varied from 800 [psia] down to 80 [psia] with a constant mixture ratio of 3.3 throughout the throttling envelope. Injector stiffness was maintained at 20% at all thrust levels.

With respect to the techniques used for thrust control, the most prominent effort in the East is attributed to Bazarov [19]. According to his investigation, through the use of controllable swirl atomizers, it is possible to obtain deep thrust variations while maintaining combustion efficiencies as high as 96% and stable regime within all the range of thrust. Bazarov has applied the classic swirl theory to dual-channel tangential orifice injectors thus providing a throttling system that requires no moving parts. A brief description of the hardware, with special attention to the cavitating venturi valve designs used for the Lunar Module Descent Engine and the TRW MIRA 150 Engine are given in reference [20]. Experimental results are discussed which include pressure recovery, mixture ratio control, gas saturation effects and boundary layer effects. Using water as the flowing medium, Baker [21] developed an inert calibration technique in which the inlet pressures, line flows, as well as engine throttle position are varied and measurements are taken of pressure drops, flow rates and corresponding valve strokes. This technique led to a reduction in the amount of hot-fire tests and yielded to a more economical means to indicate that the engine is calibrated. A comprehensive review of the techniques and capabilities of throttling engines is given by Casiano et al. [15]. The cited reference is in itself a literature review of the many efforts dedicated to the application of variable thrust engines in the West and in the East. Attention is given primarily to the techniques employed whereas not too much emphasis on the requirements definition is pursued. An early attempt to establish throttling requirements for various applications is given by Welton [22]. General throttling requirements for specific missions such as rendezvous, lunar landing and de-orbit and weapons systems are generally discussed. The paper also presents basic throttling techniques and their drawbacks, focusing on the injection of inert gas in the low throttle regime. This was a technique developed by Rocketdyne at the time and considered as an alternate option for the American lunar module descent engine. Another early research devoted to elucidating and applying throttling techniques was conducted by Cardullo and Rickerson [23]. The paper discusses both theoretical and experimental results. Three throttling techniques are presented: throat throttling, injection throttling and a combination of both. The analysis revealed under certain assumptions that for an engine to be able to maintain constant chamber pressure during throttling, the ratio of throat area-to injection area must remain

constant. The study confirmed that this could only be achieved by an engine with combined throat and injection throttling.

Carey [24] presented experimental results for a dual-mode spacecraft manoeuvring engine. The engine employed a fixed geometry triplet injection system, demonstrating 8:1 pure thrust modulation and up to 100:1 thrust ratio during short impulse bits. Stable operation was successfully achieved, however at the price of a rather low combustion efficiency in the low thrust level. The author describes the reasons for a fixed area injection head, among them, design simplicity, reliability and faster response time required for pulsed-mode operation.

The closed-loop throttling control of a laboratory scale hybrid rocket engine was demonstrated in the work of Whitmore et al. [25]. The objective was to mitigate the performance variability inherent to hybrid engine systems and implement a precise control using "off-the-shelf" components. The initial approach employed open-loop hot-fire runs to essentially characterize the system in terms of valve position and engine thrust level. High fidelity modelling and simulation of the various engine components was combined with the experimental runs to tweak the closed-loop gains of the controller. The authors were able to reduce mean run-to-run thrust variability from $\pm 9.1\%$ to less than $\pm 3.9\%$. When throat erosion are accounted for, the closed-loop thrust variability reduces to $\pm 1.5\%$.

2.3. Relevant Literature on Injectors for Thrust Variations

2.3.1. Fixed-Area Swirl Injectors

Although the fundamentals of swirling flow dynamics were established more than 60 years ago by Abramovich [26] in 1944 and independently by Taylor [27] in 1947, the hydraulic characteristics of a liquid swirl atomizer remains a complicated problem since fluid properties and element geometry have strong influence on injector performance. For example, the mass flow through a swirl injector increases with an increase in liquid viscosity, while the situation is reversed in jet injectors, despite the fact that the general trend of the two types of injectors is identical for ideal fluids. Motivated by these early works, Chinn [28] demonstrated that the principle of maximum flow – *minimum entropy* – can be adequately applied to swirl atomizers, under certain simplifying assumptions. Later on, the theoretically derived functions for the air core diameter, discharge coefficient and spray cone half-angle were charted and compared with experimental results from the literature [29]. This comparison led to the conclusion that the inviscid theory may be of benefit in the basic understanding of the flow physics of swirl atomizer internal flow, being of limited value for the detailed description of the flow regime as it does not consider variations in the supply pressure, viscosity, turbulence, wall effects or fluid-gas interactions.

Coaxial swirling spray-type injectors have been predominantly used since the 1930s in most of the Russian LPRE and gas generators [14]. As a consequence, the design of these elements is widely covered in the Russian literature, including, for example, the work of Khavkin [30] who describes the extensive research related to theoretical as well as experimental investigation of swirl injectors in the former Soviet Union. Kurpatenkov and Kessaev [31] and Dobrovolski [32] established a straightforward design methodology for swirl atomizers. The up-to-date discussion of the classical theory and the injector design

criterion, were presented by Bazarov et al. [33] and Bayvel and Orzechowski [34]. In the West, swirl injectors have come into wider use in the past few decades. An effort was undertaken by Long et al. [35] to study swirl injectors for use with non-toxic hypergolic propellants. Several injector iterations were designed and subjected to cold flow and engine tests. The injector spray cone angle and discharge coefficient were then compared to theoretical predictions. Significant burning inside of the injector elements was observed during hot-fire tests. The study continued into the research of swirl injectors for the oxidizer rich staged combustion cycle [36]. This effort was focused on developing alternative injector designs aiming to obtain their stability margins.

Given the difficulty to describe the flow behaviour in swirl atomizers, publications on the effect of injector geometric and operating parameters on spray characteristics often report contradictory results [37]. Sasaki et al. [38] performed a comparative study regarding recessed and non-recessed swirl coaxial injectors, under cold flow and combustion tests. The recessed oxidizer post injector resulted in a significant increase in heat load on chamber walls and unstable combustion. In a recessed injector, because the liquid sheet generated by the swirl motion impinged on the outer wall of the annular fuel passage, its spray angle narrowed with a deformed pattern. The liquid sheet, which blocked the annular passage, was blown off in the shape of a mushroom and with a screaming sound known as self-pulsation phenomena. Using water and kerosene as simulants, Han et al. [39], investigated the mixing and mass distribution of swirl atomizer spray. Employing a phase Doppler particle analyser (PDPA) and mechanical patternator, the median droplet size, spray angle and breakup length were measured. Their results indicated that an optimal recess length existed to obtain a maximum mixing efficiency. The effect of recess on the spray characteristics of swirl injectors was also investigated by Kim et al. [40]. It was found that the recess length has a strong influence on the mixing and spray characteristics by varying the interaction point between two liquid sheets. According to this investigation, the recess length resulted in different injection regimes: the external injection regime which is mainly governed by the merging phenomenon and momentum balance between the liquid sheets, and the internal injection mixing regime, which generates impact waves due to impingement of the inner spray on the outer liquid film inside the injector chamber. The attenuation of the impact wave, caused by fluid viscosity and in accordance with recess length, could possibly affect the stability of a liquid sheet.

As mentioned earlier, quantitative experimental information about atomization mechanism of swirl injectors is essential to improve the accuracy of computational models that predict the performance of liquid propellant rocket engines. The spray characteristics of swirl injectors was experimentally investigated by Inamura and Miyata [41]. The spray formation model was obtained by using the theoretical analysis of a liquid film flow on the inner wall of the injector center post and the breakup model of a liquid film. The liquid film thickness at the injector exit was obtained using a contact needle probe and the spray characteristics were measured by a Doppler particle analyser. The flow regime predicted numerically using a simplified approach showed good agreement with the measurements. Cold flow experiments were conducted by Ramezani and Ghafourian [42] in order to develop a theoretical model based on momentum balance that is able to predict combined spray angle behavior. The experimental observations indicated that inner and outer sprays are pulled together and interact to produce an overall mixing that is different from the summation of each individual spray characteristic. To account for ambient gas

density effects on atomization of swirling liquid sheets, Kim et al. [43] measured the spray cone angle and breakup length as the Weber number and ambient pressure were substantially increased. As a result of these adverse effects, the disturbances on the annular liquid sheet surface were amplified by the increase of the aerodynamic forces, and thus the liquid sheet disintegrated from the injector exit. This same effect caused the breakup length to decrease. Recently, Moon et al. [44] employed a film model and a droplet trajectory model to simply estimate the film breakup length from measured spray angle. By linking the film model and droplet trajectory model, the spray angle was calculated and the breakup location determined.

The dynamic characteristics of swirl injectors were thoroughly studied by Bazarov and Yang [45]. The overall response function of the swirl injector could be represented in terms of the transfer characteristics of each individual element (tangential passage, vortex chamber and discharge nozzle), analysed independently and then combined together. The resultant amplitude-phase characteristics were very complicated; however, they guided the designers to obtain any desired pulsation characteristics by either suppressing or amplifying flow oscillations. Based on this work, it becomes possible to control the engine combustion dynamics by changing the injector dynamics alone, regardless of other combustion chamber parts. In addition, various mechanisms for driving self-pulsations in both liquid and gas-liquid injectors were analysed and discussed in detail. The self-pulsation boundary at different operating conditions was also illustrated. Those results are essential to the engineering design. Toward the objective of better understanding the self-pulsation phenomena, Im et al. [46] measured the acoustic and dominant frequency of a swirling liquid sheet. It was found that the frequencies of the scream and the spray oscillation are linearly proportional to the liquid and gas axial Reynolds number, and the self-pulsation frequency is determined by the unstable wave of the liquid sheet. This study concluded that self-pulsation occurred due to the dominant wave of the liquid sheet.

2.3.2. Variable-Area Injectors

An interesting approach to the application of variable-area injectors is that presented by [19]. This work presents the analysis and experimental results of dual channel swirl atomizers for thrust variations. During full-thrust operation, propellant is fed by two stages of tangential channels. Throttling is achieved by regulating the mass flow in the second stage, either through valves or through partial drainage of the propellants. The ratio of flow passage areas is dependent essentially upon the desired throttling ratio, the first stage being sized for the lowest thrust regime. The great advantage of this configuration is the absence of moving parts and the possibility to achieve smooth transition of thrust regimes by appropriate design of the atomizer vortex chamber. A clear disadvantage is the wide variation in spray angle across the throttling regime. This can be remedied, partially, by adequate design of the nozzle outlet profile. The author claims a 10:1 throttling ratio with only around 50% of injection velocity loss. Bararov [47] also presented new techniques for manufacture of swirl and spray injection heads. The proposed scheme uses injection head plates bonded together through vacuum (or diffusion) bonding in a highly compact assembly. Comparatively small cavity volumes can be encountered in such a scheme and due to the plurality of elements, a high level of atomization quality can be obtained. The design is not too sensitive to pressure drop variations and manufacturing tolerances, pro-

viding both good combustion stability and possibility to vary the thrust widely.

Aiming at replacing toxic propellant reaction control systems, Calvignac and colleagues [48] presented a brief investigation of coaxial pintle injectors utilizing LO_2/LH_2 as propellants. A copper heat sink chamber was used initially for injector screening followed by a flight-weight Haynes 188[®] thrust chamber using liquid hydrogen as a coolant to keep material temperatures within limits. Two thrust settings were investigated (70% and 100%) at a mixture ratio of 4.0, resulting in a somewhat poor average combustion efficiency of 85%, indicating that performance is a strong function of momentum ratio.

A student project conducted at Purdue by Bedard et al. [49], designed, built and tested a throttlable liquid methane-liquid oxygen rocket engine intended for a prototype lunar lander. The engine uses a fixed geometry pintle injector for a shallow 3:1 thrust variation at a maximum injection pressure of approximately 2.0 [MPa]. Wall thermal protection is achieved by injecting methane through the annular slot in conjunction with a film cooling skirt. Design criteria for the pintle injector are presented. Final design configuration was ultimately defined by means of water cold-flow test iterations and visual observation of flow distribution in the pintle tip and annulus. Uncooled thrust chamber was to be used to collect information for thermal analysis, i.e. inner wall temperature profile. Numerical simulations were also tentatively run to estimate the amount of film cooling required.

A historical and technological account of the application of pintle coaxial injectors is given by Dressler and Bauer [50]. In this work are emphasized the potential scalability of pintle injectors, their great suitability to throttling and inherent combustion stability characteristics. Pintle injectors have been used with a variety of propellant combinations, including liquid oxygen and hydrogen and fluorine-oxygen and methane. Efforts to replace toxic propellants nitrogen tetroxide and monomethyl hydrazine, led to investigations using green hypergolic propellants. In the work conducted by Austin and his colleagues [51], good performance was achieved employing the pintle injector and the combination of hydrogen peroxide and a colloidal suspension of manganese oxide Mn_3O_4 in methanol, known as "block 0". This fuel can theoretically approach 93% of the vacuum specific impulse and 99% of the density specific impulse of NTO/MMH when used with 98% rocket grade H_2O_2 [51]. In this research, fuel was injected through 16 primary and secondary holes of 0.58 [mm] and 0.38 [mm] in diameter, respectively. Hydrogen peroxide was injected through an annular gap of 0.55 [mm]. This pintle design resulted in a blockage factor of 0.5 and a ratio of pintle-to-chamber diameter of 4.65, with a hemispherical external and internal tip built out of stainless steel. A fuel-centered pintle was selected primarily on the basis of a slight fuel lead required to avoid hard-starts and, additionally, due to manufacturing tolerances, which precluded the use of very small annular gaps needed to achieve optimal fuel injection velocities. An acrylic chamber was adopted to assess the initial flow patterns and startup transient. Differences in the length of receded wall revealed penetration of the fuel flow into the oxidizer flow and successful cooling of the walls aft of the injector face. Parametric studies were also carried out with different chamber characteristic lengths and diameters, momentum rates between propellants, pintle length and size of holes. Optimum momentum ratio (or more rigorously, a *force* ratio) for this propellant combination was determined to be around 0.7. Increasing the secondary-to-primary hole diameter ratio leads to decrease of characteristic velocity with apparently no influence on the specific impulse. However, when pintle length is increased, a large decrease in specific impulse was observed. The authors attribute this behaviour to lower residence

time resulting from the use of longer pintle lengths.

Gromski and his colleagues [52] present the development status of a new $\text{LO}_2/\text{hydrogen}$ engine using pintle coaxial injectors. Initially an ablative thrust chamber was employed to demonstrate successful ignition and combustion stability at discrete points. A second phase of tests used a calorimetric combustion chamber to obtain injector performance and heat transfer information. Test data was then correlated to engine conceptual design and formed a database for cryogenic pintle injector application.

2.3.3. Experimental Investigations

A fundamental study covering the effect of gas-density, molecular weight and acoustic velocity on liquid-gas spray droplet size and liquid film breakup length was conducted by Ingebo [53]. The study concluded that gas injection velocity and acoustic mass-flux have the greatest effect of all liquid- and gas-phase properties on the process of liquid-jet breakup in a high velocity atomizing gas flow. The inverse of the Sauter mean drop diameter produced with two atomizers was greater for helium than for nitrogen, due to the higher acoustic and molecular velocity of helium.

Baker [21] presents a calibration technique proposed for the LMDE. Using water as simulants and an appropriate test bench, the propellant flows and pressures along all the system components are measured in terms of throttle valve and injector position, leading to simulated static test conditions. The technique proved useful in reducing the costs associated with disposable engine parts as well as a means to mechanically check the propulsion system.

The atomization and breakup of cryogenic propellants under high-pressure subcritical and supercritical conditions were assessed by Mayer et al. [54]. Studies involved characterization of coaxial flow as well as detailed investigations of ligament and drop breakup and mixing. Revealed in the experiments was the effect of injection pressure on fluid surface tension. As pressure increases, the fluid reaches a transcritical regime where breakup and mixing are no longer influenced by surface tension. Further on, the fluids seemed to behave like viscous miscible fluids. The authors could not establish a clear value for the pressure in which this transition occurs; no clear definition can be deduced in terms of the critical pressure of the species alone, however, it is believed that the initial injection conditions and ambient composition play a major role. Transcritical injection of liquid oxygen led to no indication of surface tension and the droplets were unable to resist deformation. It was observed that the clustered mass of fluid can eventually break off at unpredictable times leading to enhancement of mixing.

An experimental study conducted by Kenny and his colleagues [55] aimed at characterizing coaxial injection and primary atomization for scaling and throttling purposes. With the argument that differential velocity plays a major role in the primary atomization of LO_2/LH_2 and the good agreement between cold flow and hot-fire tests, a test rig was used as a tool to simulate the reacting sprays in a more friendly cold flow environment. It was identified, however, that the use of water and gaseous nitrogen can be only acceptable in terms of injection and primary atomization simulation if the injector elements can operate within the same atomization conditions of the actual propellant sprays.

Combustion performance, heat transfer and stability characteristics of swirl, pintle and impinging type injectors were performed in an early study performed by Woodward et

al. [56] aimed at replacing the OMS (Orbital Maneuvering System) of the Space Shuttle. Several swirlers were tested in an optically accessible square chamber. For the pintle injectors, a conventional cylindrical chamber with an elliptical head end was employed for the hot-fires. Line-of-sight CH-radical emission assessment was used to map the combustion profile and shadowgraph imaging to evaluate the liquid spray profile. Combustion efficiencies larger than 100% was attributed to the low quality LO₂ supplied to the chambers. The effect of recess length proved useful in improving mixing in one of the swirl injectors tested. The pintle injector operated in stable mode and supplied acceptable performance and showed less sensitivity to LO₂ quality.

High speed visualization techniques were employed by Locke and his colleagues [57] in an attempt to investigate the primary atomization and combustion characteristics of a liquid oxygen and gaseous hydrogen shear coaxial injection element. Both cold-flow and hot-fire tests were recorded with the same injector type and chamber arrangement. Hot-fires revealed a long LO₂ core region breaking into large dense-oxygen structures indicating that a fragmentation model would be more suitable in describing the primary atomization behaviour at actual conditions. Cold-flows showed a clear difference among supercritical and sub-critical chamber pressures in terms of mixing phenomena.

Lux and Haidn [58] investigated the near-injector region flame stabilization in a sub-scale high-pressure liquid oxygen/gaseous methane rocket engine. Effective flame anchoring is necessary to avoid blowoff and combustion instability initiation. The authors employed optical diagnostics techniques to assess sub-, trans- and supercritical operating conditions with respect to oxygen and for a variety of injector element geometries. OH radical identification was used to detect the flame anchoring point near the LO₂ post tip during ignition and steady-state operation. Even though theoretical investigations indicate a different flame behaviour among LO₂/methane and LO₂/hydrogen combustion, no significant deviation was visible in the emissions associated with sub- and supercritical injection conditions. Near-injection flame shape is influenced by the injection parameters and is in agreement with LO₂/hydrogen combustion studies, where an increasing momentum flux ratio leads to a more constricted flame and smaller spreading angle. The use of a recessed LO₂ post was also assessed by the authors [59], using the same experimental setup described previously. This arrangement resulted in flame anchoring inside the recessed region, leading to increased pressure drop and flame expansion right after injection, which decreases with increasing momentum flux ratio. The recessed post also led to smoother combustion.

2.3.4. Other Types of Injectors for Thrust Variations

A new set of possibilities for porous type injectors was presented by Bazarov [60]. The paper describes features, experimental results, advantages and drawbacks of swirl and jet atomizers with porous inserts. Also recommends values of permeability for the many different configurations. According to the author, the non-repeatability of some porous materials characteristics, their tendency to contaminate and the somewhat unpredictable hydraulic behaviour may impose some difficulties, especially in multi-injector configurations. In general, however, the improved atomization with relatively low associated pressure drop suggests a good potential for throttling.

Additional details can be found in the cited references.

Part II.

Requirements Definition

3. Mission Requirements

The performance requirements for any propulsion system are dictated by the specific application considered. A survey of mission requirements in terms of engine throttling ratio, burn duration, number of burns, ΔV and thrust program for various applications is presented in Table 3.3. The mission model for the proposed variable thrust propulsion system has been considered an unmanned Mars landing vehicle. In this framework, basic propulsion system requirements were determined in terms of thrust level, thrust-to-weight ratio and throttle profile.

3.1. Mission Characteristics

For the purposes of this study a low lift-to-drag ratio vehicle configuration was chosen. This is based on cost, testing requirements, simplicity and the absence of mission requirements that might dictate another choice (such as a requirement for direct entry from orbit). The Mars Science Laboratory Mission (MSL) [61], [62] is an example of the application of this concept. A representative Mars landing mission profile is illustrated in Figure 3.1 where a step-wise deceleration technique is used. During the first stage, deceleration is initiated by a de-orbit rocket burn and the vehicle orientation is adjusted to the correct angle for entry into Martian atmosphere. This maneuver is followed by the parachute deployment which settles the propellants in the tanks and alleviates the propulsion system total impulse requirement. The terminal descent is then finally accomplished entirely by the lander propulsion system with ignition occurring at an altitude of 1 to 5 [km].

A hypothetical thrust profile from de-orbit to landing is presented in Figure 3.2. Representative system characteristics for a mission with a spacecraft initial mass of 850 [kg] using a set of four LO_2/LCH_4 engines are shown in Table 3.1.

Table 3.1.: Assumed Spacecraft and System Characteristics

Parameter	Value
Initial spacecraft mass, [kg]	850
Final mass on Mars, [kg]	400
Assumed thrust-to-weight ratio	2.5
Mass of heat-shield, [kg]	250
Mass of parachute, [kg]	100
Mass of propulsion system, [kg]	100
Heat-shield ballistic coefficient, [kg/m^2]	35
Parachute ballistic coefficient, [kg/m^2]	6

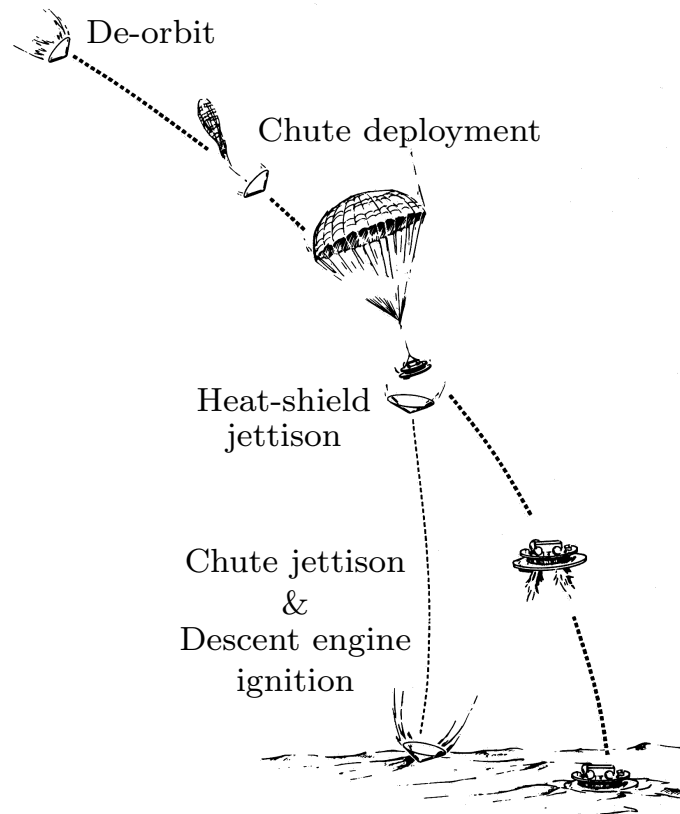


Figure 3.1.: Terminal deceleration sequence.

3.2. Mars Lander Requirements

The parameters defining ΔV requirements for a Mars landing are dependent on mission profile and guidance characteristics during the final terminal phase. As an example, for the Mars Rover Sample Return (MRSR) Mission considered in reference [63], an initial vehicle mass of 4082 [kg], with a lift-to-drag ratio of 0.98 and a ballistic coefficient of 397 [kg/m²] requires a total ΔV of 350 [m/s]. The study showed that the value is dependent, for instance, on the wind component present on the landing phase, on the guidance requirements (whether a "pinpoint" or a "soft-landing" is practiced), on the atmospheric density profile and on parachute deployment height. The proposed throttle profile of Figure 3.2 shows constant thrust fractions resulting in a total impulse, and therefore in a corresponding vehicle size, which is a direct function of the selected thrust level of the engine. This approach was adopted instead of considering a given constant vehicle size with variable thrust engines, as will be discussed in Section 3.3.

3.2.1. Assumptions

Since it was not within the scope to conduct a complete flight control study which would by necessity include attitude control and guidance component considerations, only

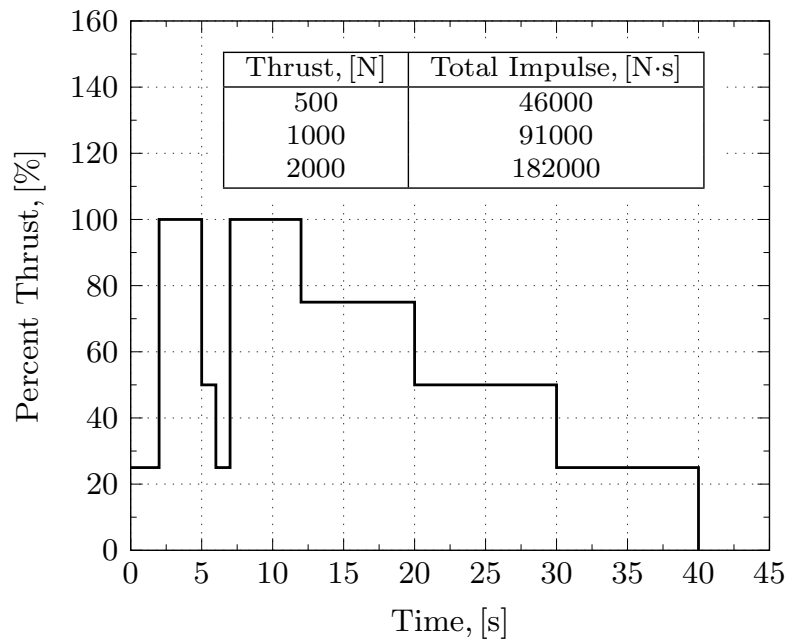


Figure 3.2.: Baseline Throttle Profile.

the requirements for achieving null horizontal and vertical velocity components at lander touchdown were considered in the calculations. It was also assumed that the parachute, heat-shield or other decelerating devices would provide the following initial conditions at engine ignition:

- Total lander mass;
- Vertical velocity;
- Horizontal velocity;
- Altitude above the surface.

By fixing these initial conditions, the effect of engine thrust level on landed payload can be evaluated. The study is based on typical Mars vehicle configurations where the engines are used to provide some pitch and yaw stabilization as well as velocity vector control. The following sections present the basic assumptions and equations used in the analysis and the resulting conclusions.

3.3. Thrust Level Selection Based on Payload Optimization

As previously outlined, the analysis evaluates the effect of thrust level on lander payload capability without considering explicitly the requirements resulting from attitude stabilization or the guidance and control loops. This approach is reasonable in that engine

3. Mission Requirements

differential throttling provides vehicle stability, and therefore, requires that only some additional thrust be added to the nominal thrust level without substantially changing the total impulse requirement.

3.3.1. Basic Assumptions and Equations

In order to achieve the desired results of this study, the following assumptions were made:

1. Flat planet;
2. Constant gravitational acceleration;
3. Constant thrust landing;
4. Zero aerodynamic forces.

Naturally, variations in each of these parameters would be of interest for guidance, navigation and control purposes, but it is believed these factors do not considerably affect the results of the present analysis. It was also assumed that the vehicle could be aligned with the lander velocity vector such that both the vertical and horizontal velocity components could be canceled. The conventional equations describing the vertical profile as a function of thrust level P , specific impulse I_{sp} , vehicle initial landing mass m_i and landing or engine burn time t , were re-arranged for handier use and are respectively (3.1), (3.2) and (3.3):

$$\frac{d(dh/dt)}{dt} = g_m + \frac{\dot{m}g_e I_{sp}}{m}. \quad (3.1)$$

$$\dot{h}_o = g_e I_{sp} \ln \left[\frac{m_i}{m_i + \dot{m}t} \right] - g_m t. \quad (3.2)$$

$$h_o = \frac{1}{2} g_m t^2 + \dot{h}_o t + \frac{g_e I_{sp} m_i}{\dot{m}} \left[\frac{m_i + \dot{m}t}{m_i} \right]. \quad (3.3)$$

where g_e and g_m are the Earth and Mars gravitational accelerations, respectively. Calculation of the rate of vehicle mass change \dot{m} is determined from Equation (3.4) assuming that propellant expenditure is the only source of that change:

$$\dot{m} = -4 \frac{P}{I_{sp}}. \quad (3.4)$$

An average engine I_{sp} of 3200 [m/s] was adopted for the analysis. Using these basic equations and assumptions, an overall understanding of the effect of engine thrust level on landed payload can be gained.

3.3.2. Relative Payload Determination

Figures 3.3a and 3.3c show the effect of thrust level on landing time and total impulse as a function of ignition altitude. The mass of the lander after parachute and heat-shield separation is taken as being in the order of 500 [kg]. As can be seen, for a fixed total

impulse there is a maximum ignition altitude which occurs at an engine thrust level of about 1000 [N]. As thrust level increases, the burn time and ignition altitude converge to zero and as thrust level is reduced to a certain point where the total thrust-to-Mars-weight ratio approaches unit, the ignition altitude as well as the initial vertical velocity must again near zero. This is best shown in Figure 3.3b and 3.3d. The former is simply a cross plot of Figure 3.3a where landing time is replaced by initial vertical velocity and the latter is the same plot, but for an initial lander mass of 1000 [kg]. Clearly, as initial lander mass increases twofold, the thrust level at maximum ignition altitude also increases twofold. Typical free fall lines have been included in the curves. Free fall line (2) in Figure 3.3b corresponds to a lander whose initial conditions are given by:

- Ignition altitude: 1500 [m];
- Vertical velocity: 85 [m/s];
- Horizontal velocity: 75 [m/s].

It can be seen from these figures that as the lander free-falls from the initial altitude and vertical velocity, the thrust level required to land increases continuously and the total impulse decreases initially but then tends to an almost constant value as the free fall line begins to parallel the total impulse lines. This behavior is also represented in Figure 3.4 and Figure 3.5a. The former shows the variation in gross landed mass fraction as a function of ignition altitude and thrust level and suggests the existence of a maximum value. The latter shows the same mass fraction plotted against thrust level for the two different vehicles masses and the two different free fall lines. It can be concluded that the curve shifts vertically as a function of initial velocity and altitude and horizontally according to initial lander mass.

In order to determine the maximum payload mass fraction, the increase in propulsion system weight with thrust level and total impulse must be considered. Reference [64] proposes equations and methods for estimation of various propulsion system component weights. For the preliminary design stage, however, the more direct approach provided by [65] was adopted. This is based on statistical mass coefficients for the tanks, engine and associated equipment, as given by Equations (3.5) through (3.7).

$$m_T = K_T m_p. \quad (3.5)$$

$$m_{eng} = K_{eng} \left(\frac{P}{g_e} \right). \quad (3.6)$$

$$m_{equip} = K_{equip} m_i. \quad (3.7)$$

where the corresponding mass coefficients are given in Table 3.2.

Using the recommended parametric engine, tank and equipment mass data of Table 3.2, Equation (3.8) was used to adjust the results of Figure 3.5a.

$$\frac{\Delta m}{m_i} = -4 \frac{(\partial m_{eng} / \partial P) \Delta P + (\partial m_T / \partial m_p) \Delta \dot{m}}{m_i}. \quad (3.8)$$

3. Mission Requirements

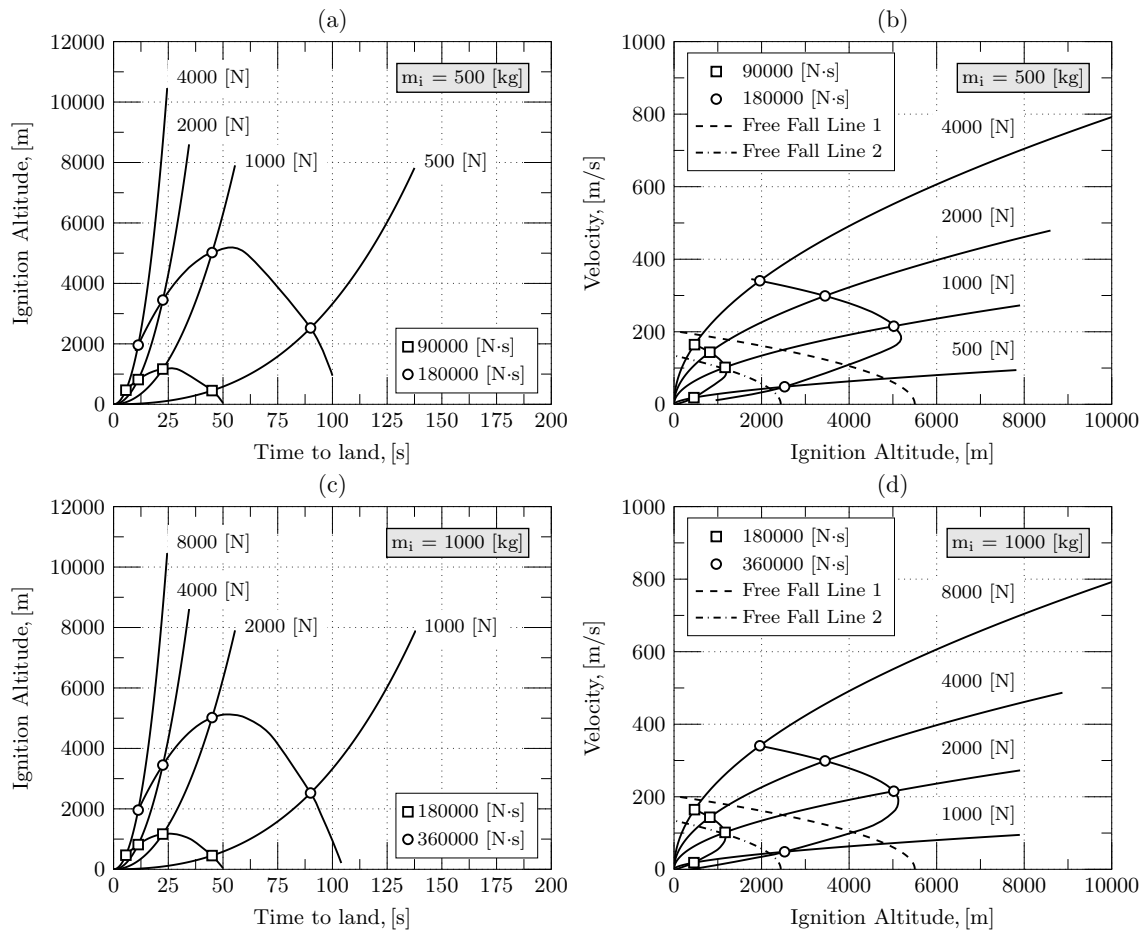


Figure 3.3.: Lander vertical velocity and ignition altitude.

Table 3.2.: Mass Coefficients [65]

Coefficient	Recommended range	Adopted value
Propellant Tank, K_{tank}	0.03...0.06	0.06
Engine, K_{eng}	0.015...0.05	0.05
Equipment, K_{equip}	0.03...0.07	0.03

This adjustment produces the results of Figure 3.5b which shows that an optimum engine thrust level of approximately 1000 [N] exists based solely on vertical velocity. This results in a total thrust-to-initial-Mars-weight ratio of approximately 2.2:1. As can be seen, as the initial vehicle mass is doubled (to 1000 [kg]), the optimum thrust appears to double (ca. 2000 [N]) but the peak becomes less pronounced because the sensitivity of total engine mass to thrust level does not change. The mass fractions presented in Figure 3.5b are relative values; the fixed mass for a propulsion system using e.g. 500 [N] engines must be introduced to determine absolute "useful payload" values. To include the effect of the hori-

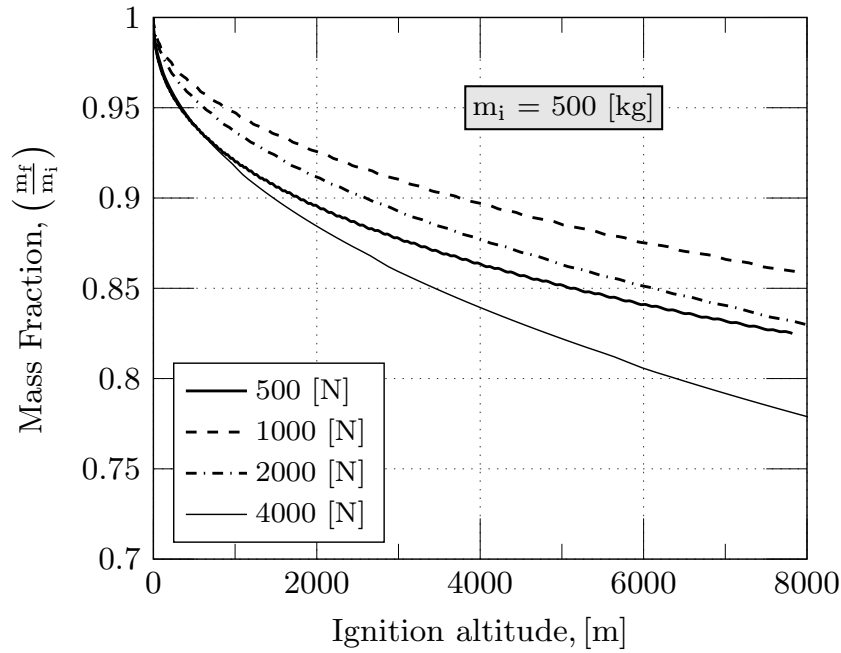


Figure 3.4.: Mass fraction versus ignition altitude for a lander initial mass of 500 kg.

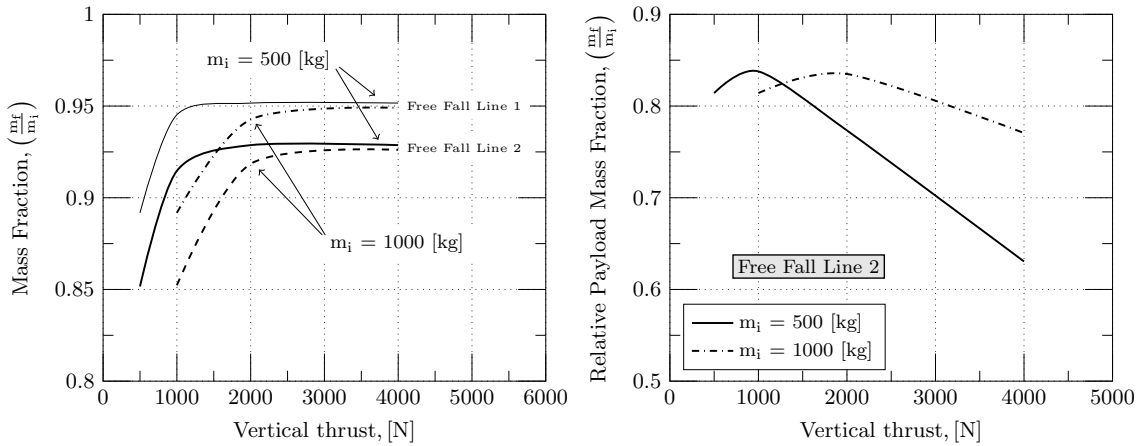


Figure 3.5.: Payload mass fraction.

zontal velocity, Equation (3.9) was solved, taking into account the initial value of 75 [m/s]. This results in an additional propellant mass of about 12 [kg] and a total horizontal impulse requirement of approximately 38000 [N·s] while the total vertical impulse required is on the order of 105000 [N·s]. This leads to an actual total impulse requirement of about 112000 [N·s].

$$\Delta V = I_{sp}g_e \ln \left(\frac{m_i}{m_f} \right). \quad (3.9)$$

Since the vehicle uses a single set of four fixed thrust engines, the relation between total

3. Mission Requirements

thrust and vertical thrust can be evaluated by Equations (3.10) and (3.11).

$$\frac{P}{P_v} = \frac{[(P_{vt})^2 + (P_{ht})^2]^{1/2}}{P_{vt}}. \quad (3.10)$$

$$= \frac{[(I_{tv}^2) + (I_{th}^2)]^{1/2}}{I_{tv}}. \quad (3.11)$$

Solving this equation results in a ratio of 1.1 which implies that the actual engine thrust level should be about 1100 [N], with a thrust-to-initial-Mars-weight ratio of 2.4:1 excluding any additional stability and control considerations. This value compares with ca 2.1:1 for the MSL mission [62] during the landing phase and with roughly 3:1 for Viking class vehicles [66].

3.4. Conclusions

Based on the results of payload optimization study and overall mission requirements, the conclusions are:

- A maximum thrust level of about 1100 [N] (thrust-to-Mars-weight ratio of 2.4:1) is desirable for a 500-[kg] class Lander using four engines based on payload optimization;
- An optimum lander thrust-to-weight ratio exists which is more or less independent of vehicle size;
- A more detailed evaluation would be required to assess the effects of aerodynamic forces and required landing maneuvers on the value of the thrust level;
- Regarding thrust variability, fixed thrust engines will yield acceptable landing velocities if the various errors (starting, trajectory, terminal landing) can be held sufficiently small. However, it is believed that considerably larger errors can be tolerated if the engines possess some thrust modulation capability.

It can be concluded that a fixed thrust-to-Mars-weight ratio of at least 2.4:1 shall be used and that a fixed engine duty cycle is valid for determining initial system requirements. A minimum value of 6:1 thrust variability seems adequate [62], [66] and shall be adopted for subsequent engine design analysis.

Table 3.3.: Mission and Propulsion System Requirements.

Space Mission	Basic Mission Requirements							
	Range of ΔV , [fps]	Range of desirable P/W_{earth} , [N/N]	Allowable impulse cutoff accuracy $\Delta I_t/M_t$, [N·s/kg]	Required thrust variability	Restart requirements	Typical minimum service life, [s]	Thrust Program	Storability Requirements
	1	2	3	4	5	6	7	8
1. 600-km Orbit								
A. Orbit Correction								
▶ Orbital perturbation	100 to 1000	0.05 to 1.0	1.5	None	Multiple	240	1/3	Months
▶ Eccentricity control	100 to 5000	0.05 to 1.0	2.5	None	None	60	1	Months
▶ Orbital plane change	200 to 19000	0.15 to 2.0	1.0	None	None	60	1	Months
▶ Orbital altitude variation	200 to 14000	0.1 to 2.0	1.0	None	1 to 2	60	1/3	Months
▶ Orbital epoch change	100 to 20000	0.1 to 2.0	0.5	None	1 to 2	60	1/3	Months
▶ Correction of injection error	50 to 1000	0.01 to 0.5	0.03	None	1 to 2	125	1/3	5 days
B. Orbital Rendezvous								
▶ Nominal injection errors	50 to 1000	0.01 to 1.5	0.15 to 0.5	100:1	0 to 2	40	2/3	5 days
▶ Dog-leg maneuver	500 to 18000	0.01 to 3.0	0.15 to 0.5	1000:1	1 to 2	85	2/3	5 days
▶ Emergency rendezvous	1000 to 25000	0.01 to 3.0	0.15 to 0.5	1000:1	1 to 2	100	2/3	1 day
2. Geostationary Orbit								
A. Correction of injection errors	100 to 450	0.0004 to 0.2	2.0 to 15	None	Multiple	-	1/3	1 Month
B. Station keeping	50 to 130	0.0002 to 0.02	0.55 to 3.25	None	Multiple	-	1/3	2 Years
C. Attitude control	-	-	-	None	Multiple	-	1/3	2 Years
3. Lunar Flights								
A. Trajectory correction								
▶ Midcourse - flight	25 to 250	0.025 to 0.25	0.02	None	3	62	1/3	3 Days
▶ Terminal - flight	25 to 500	0.020 to 0.5	0.03	None	2	62	1/3	3 Days
▶ Terminal - return	50 to 500	0.015 to 1.0	0.15 to 0.30	None	3	62	1/3	Months
B. Lunar Orbit	2000 to 5500	1.0 to 2.0	0.15 to 1.0	None	None	110	1	3 Days
C. Lunar Landing								
▶ Direct	9800 to 9900	1.0	-	6:1	None	330	2	3 Days
▶ From orbit	5700 to 6000	1.0	-	6:1	1	200	2/3	3 Days
D. Lunar Take-off								
▶ To orbit	6000 to 6500	1.0 to 1.6	0.15	None	1	140	1/3	Weeks
▶ Direct to Earth	9000 to 11000	1.0 to 1.5	0.30	None	None	130	1	Weeks

Table 3.3.: Mission and Propulsion System Requirements. (continued)

Space Mission	Basic Mission Requirements							
	Range of ΔV , [fps]	Range of desirable P/W_{earth} , [N/N]	Allowable impulse cutoff accuracy $\Delta I_t/M_t$, [N·s/kg]	Required thrust variability	Restart requirements	Typical minimum service life, [s]	Thrust Program	Storability Requirements
	1	2	3	4	5	6	7	8
4. Mars Flights								
A. Trajectory correction								
▶ Midcourse - flight	50 to 1000	0.025 to 0.50	0.05	None	6	300	1/3	250 Days
▶ Terminal - flight	100 to 1000	0.020 to 1.0	0.3	None	3	62	1/3	250 Days
▶ Midcourse - return	50 to 1000	0.025 to 0.50	0.05	None	6	310	1/3	3 Years
▶ Terminal - return	200 to 1500	0.03 to 1.0	0.1 to 0.25	None	3	62	1/3	3 Years
B. Mars Orbit								
▶ No atmospheric braking	5000 to 20000	1.0 to 3.0	0.5 to 2.0	None	None	104	1	250 Days
▶ With atmospheric deceleration	≈ 1000	0.5 to 1.0	0.03	None	5 to 10	30	1/3	250 Days
C. Mars Landing								
▶ Direct	13000 to 21000	1.0 to 2.0	-	10:1	0 to 1	300	2/3	250 Days
▶ From orbit	11000 to 15000	2.0 to 4.0	-	10:1	1	140	2/3	250 Days
D. Mars Take-off								
▶ To orbit	15000 to 17000	0.7 to 1.0	0.3	None	1	170	1/3	Years
▶ Direct to Earth	20000 to 35000	-	0.3	None	None	-	1	Years
• 1st Stage	-	1.5 to 2.0	-	-	-	100	-	-
• 2nd Stage	-	1.0 to 2.0	-	-	-	120	-	-

Notes to each column:

- ¹ Estimated range of ideal velocity increments for each maneuver [67].
- ² The thrust and acceleration requirements for the various applications [67].
- ³ The allowable total impulse error per unit mass at cutoff [67].
- ⁴ Control of thrust level or total impulse per unit time [67].
- ⁵ Possible number of starts required [67].
- ⁶ Typical burning time required for a fixed thrust level and total impulse maneuver [67].
- ⁷ Typical thrust program for mission [67]. (1 = Constant, 2 = Variable, 3 = Pulse)
- ⁸ Propellant space storability requirements [67].

4. Propulsion System Concept Selection

The intent of this chapter is to evaluate potential propulsion concepts in the context of the mission model and recommend a system to be designed, fabricated and tested. The main goal is to determine the applicability and limitations of regenerative cooling at the nominal engine thrust and indicate potential engine cycle concepts.

4.1. Propellant Properties and Theoretical Performance

Since a large quantity of data were generated during the analysis and since it was not convenient or necessary to present all of the data in the following discussion, all the theoretical propellant performance for LO₂/LCH₄ generated was extracted by referring to Gordon and McBride [68]. Representative propellant thermodynamic and transport properties are summarized in table form in Appendix A. Additional data for the regenerative and film-cooling analysis was taken directly from the REFPROP database [69].

4.2. Assumptions for the Attainable I_{sp}

The following discussion presents the technique used to estimate propellant performance in terms of attainable specific impulse. For the purposes of this analysis, the performance loss factors were separated in two categories [70]:

- Thrust chamber performance losses;
- Injector combustion efficiency losses.

It is possible to define engine efficiency ($\eta_{I_{sp}}$) as:

$$\eta_{I_{sp}} = \frac{I_{sp}^{del}}{I_{sp}^{th}} = \eta_{C^*} \eta_{tc}. \quad (4.1)$$

where:

- η_{C^*} = combustion efficiency, dimensionless;
- η_{tc} = thrust chamber efficiency, dimensionless;
- I_{sp}^{del} = delivered engine performance, [m/s];
- I_{sp}^{th} = theoretical equilibrium performance, [m/s].

For a perfect injector and sufficiently high characteristic length values, η_{C^*} is assumed to be unit [70]. The thrust chamber efficiency includes recombination losses (kinetic losses), nozzle divergence losses, viscous losses (combination of friction and heat transfer losses) and zonal losses. The thrust chamber efficiency is defined as follows [70]:

4. Propulsion System Concept Selection

$$\eta_{tc} = \frac{I_{sp}^{TC}}{I_{sp}^{th}} = \eta_{kin}\eta_{vis}\eta_{div}\eta_z. \quad (4.2)$$

where:

- I_{sp}^{tc} = delivered thrust chamber performance
for an ideal injector (100% combustion efficiency), [m/s];
- η_{kin} = recombination losses, dimensionless;
- η_{div} = nozzle divergence losses, dimensionless;
- η_{visc} = viscous losses, dimensionless;
- η_z = zonal losses, dimensionless.

It is assumed that each of the performance losses listed above are uncoupled.

Recombination (Kinetic) Losses

Because of the high theoretical combustion temperatures (well above 2000 [K]) and the resultant dissociated gas species, it is anticipated that the LO_2/LCH_4 may have relatively large recombination (kinetic) losses. Tables for calculation of kinetic losses for various propellant combinations can be found in the work of Bender et al. [71]. For the present analysis, the effect of non-equilibrium chemistry was assumed to produce a loss of 1% compared to shifting equilibrium chemistry.

Divergence Losses

Divergence loss is essentially a loss due to nozzle geometry in that the gases leave the nozzle exit at some angle with respect to the nozzle axis. The momentum loss to any non-axial alignment of the exit momentum vector results in the divergence loss. The divergence loss coefficient (η_{div}) is determined as follows:

$$\eta_{div} = \frac{K_{p2D}}{K_{p1D}}. \quad (4.3)$$

where K_{p2D} is the two-dimensional inviscid thrust coefficient for the bell nozzle and K_{p1D} is the one-dimensional inviscid thrust coefficient. The divergence loss coefficient was used as a constant throughout the analysis and set equal to 0.98.

Viscous Losses

The combined friction and heat transfer losses which are defined as the viscous losses can be computed using the technique of reference [72]. This reference considered the simultaneous solution of the integral momentum and integral energy equations for the turbulent boundary layer in a rocket engine. From the solution of these equations, the momentum efficiency at the exit of the nozzle due to the boundary layer can be determined.

$$\Delta M_x = \frac{\rho U^2}{2g} 2\pi r_e (\theta \cos \alpha_e). \quad (4.4)$$

where:

$$\begin{aligned} \Delta M_x &= \text{axial component of momentum deficiency due to boundary layer, [N];} \\ \frac{\rho U^2}{2g} &= \text{inviscid momentum flux at the edge of the boundary layer, [N/m}^2\text{];} \\ r_e &= \text{nozzle exit radius, [m];} \\ \theta &= \text{momentum thickness, [m] ;} \\ \alpha_e &= \text{nozzle exit angle, [}^\circ\text{].} \end{aligned}$$

The viscous loss parameter is then computed as:

$$\eta_{visc} = 1 - \frac{\Delta M_x}{P}. \quad (4.5)$$

where the thrust P is the inviscid vacuum thrust based on the equilibrium thrust coefficient. In this analysis, a constant average value of 0.98 was adopted for preliminary purposes.

Zonal Losses

Performance levels are sensitive to variations in mass and mixture ratio distributions across the chamber. This parameter is highly dependent on the cooling approach and injector type used. Multi-zone models are described in the literature by Kurpatenkov and Kessaev [72] and by Dobrovolski [32]. In the case of film-cooling, a rather complex interaction between the core gas flow and near-wall liquid film exists, and that complicates the estimation of zonal losses. For this analysis, it was assumed that a maximum of 3% performance losses are present, as long as the central core can be maintained at the global equilibrium mixture ratio.

4.3. Thrust Chamber Cooling Analysis

The cooling techniques considered for this concept study were:

- ▶ Regenerative cooling;
- ▶ Film-cooling;
- ▶ Radiation cooling.

Ablative cooling was omitted because of the extra difficulties involved in characterizing the material for e.g. char rate and mechanical behavior. Conventional single-mode cooling concepts having the highest performance potential, such as radiation and regenerative cooling using only LCH_4 were first considered. These were followed by (a) regenerative cooling with LO_2 and (b) regenerative cooling with both propellants (dual-regen). The lower-performance film-cooling approach was regarded as a backup option whenever the limits of regenerative cooling had been reached or its applicability had fallen outside what is feasible in terms of low-development time and cost. Radiation cooling was considered only for the nozzle extension part of the thrust chamber.

4.3.1. Baseline Engine Contour

The basic non-dimensional thrust chamber contour used in the conceptual studies is shown in Figure 4.1. This was largely based on chamber design information given by reference [73] for LO₂/kerosene and LO₂/LH₂ engines and on experimental data provided in the work of Kurpatenkov and Kessaev [72]. A design chamber pressure of $p_k = 2.5$ [MPa] was selected, which is based on the minimum chamber pressure level at low thrust that would ensure stable (chugging free) operation [72],[64]. A baseline characteristic length (L^*) of 1.50 [m] was considered. The convergent section contour was defined so as to minimize boundary layer turbulence within the limits of standard design practice. The upstream radius ratio R_2/R_k determines the surface length of the peak heat flux location and, therefore, a small value of 1.0 was taken. A high convergence ramp angle could result in local boundary layer separation and resultant increase in heat fluxes. Generally, an average maximum convergence angle of 35 degrees to prevent flow separation and local perturbations in the local heat-transfer coefficient is considered adequate. Kurpatenkov and Kessaev [72] propose an empirical expression for the value of chamber contraction ratio given by:

$$f_k = \frac{500 \cdot 10^3}{\sqrt{10p_k d_{kp}}} \quad (4.6)$$

where p_k is the chamber pressure in Pascals and d_{kp} is the throat diameter in millimeters. Equation (4.6) seems to be more appropriate for high-thrust, high chamber pressure engines. However, benchmark data provided by Kozlov [8] indicate that values up to 13:1 are normal for low-thrust engines running on light hydrocarbons and liquid oxygen. Practical considerations regarding engine size and chamber diameter appropriate for injector design, igniter installation and fabrication resulted in a recommendation of a minimum contraction ratio of 8.

A conventional nozzle contour for a 60:1 area ratio, 5° exit wall angle was selected for the conceptual studies. Non-dimensional coordinates were established on the basis of the method of characteristics outlined by Kurpatenkov [74]. The cooled surface area, length and local diameters were then a function of the throat diameter calculated for the specific thrust, chamber pressure and mixture ratio, using preliminary specific impulse and nozzle thrust coefficient values. The contour immediately upstream of the throat was taken as a circular arc of radius equal to $1.0 \cdot r_{kp}$. The divergent section nozzle contour was made up of a circular entrance section of radius equal to $0.450 \cdot r_{kp}$ instead of the usual 0.382 value [75]. According to Dobrovolski [32], this nozzle contour arrangement provides good aerodynamic performance.

4.3.2. Gas-side heat transfer

Gas-side heat transfer rates were computed using an effective gas-side heat transfer coefficient and temperature difference as the potential for heat transfer as shown by Equation (4.7).

$$\ddot{q}_g = h_g (T_{aw} - T_{wg}) \quad (4.7)$$

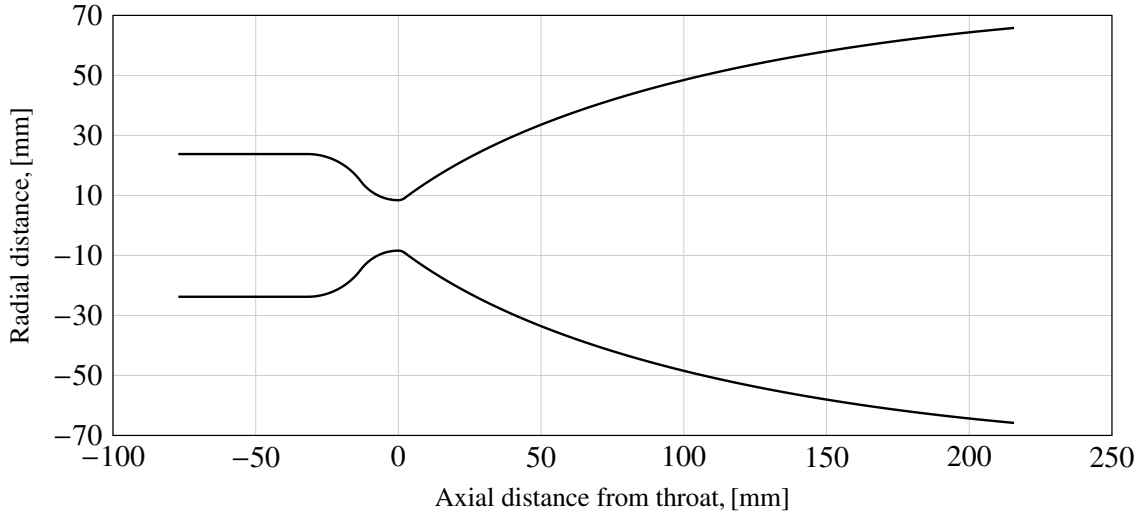


Figure 4.1.: Baseline thrust chamber contour.

where:

- \ddot{q}_g = local heat flux, [W/m²];
- h_g = effective gas side heat transfer coefficient, [W/m² K];
- T_{aw} = local driving temperature for heat transfer, including recovery effects, [K]; and
- T_{wg} = gas-side wall temperature limited by the chamber material.

The adiabatic wall temperature or the driving temperature for heat transfer was calculated as follows:

$$T_{aw} = T_{0k} \left[\frac{1 + r \left(\frac{\gamma-1}{2} \right) Ma^2}{1 + \left(\frac{\gamma-1}{2} \right) Ma^2} \right]. \quad (4.8)$$

where:

- T_{0k} = total gas temperature, [K];
- γ = gas specific heat ratio, dimensionless;
- Ma = free stream Mach number, dimensionless;
- r = recovery factor.

The recovery factor was generally taken as that of turbulent boundary layers [76] and is given as:

$$r = \sqrt[3]{Pr}. \quad (4.9)$$

The gas convection coefficient was computed using the Siniarev correlation with variable coefficients as described by Gross [77] and as shown by Equation (4.10) below.

$$h_g = C_g C_{p_g} \mu_g^{0.18} \left(\frac{\dot{m}}{D} \right)^{0.82} \left(\frac{T_{aw}}{T_{wg}} \right)^{0.35}. \quad (4.10)$$

4. Propulsion System Concept Selection

where:

- C_g = correlation coefficient, dimensionless;
- C_{p_g}, μ_g = combustion gas specific heat and viscosity,
computed at the gas-side wall temperature, [J/kg K], [Pa·s];
- D = thrust chamber sectional diameter, [m];
- \dot{m} = mass flow rate of combustion gases, [kg/s].

Throat Reynolds numbers for the present analysis are considered to remain in the turbulent range, although during low-thrust engine operation the boundary layer might indeed transition to laminar flow or to a transitional state [32]. In this case, computation of h_g is more complex than that given by Equation (4.10). At high Reynolds numbers, heat transfer coefficients calculated from Equation (4.10) simply reflect those of a standard pipe correlation. However, to account for the effects of flow acceleration in the throat region, the value of the correlation coefficient C_g was adjusted as a function of the ratio of axial distance from the throat and throat radius ($\frac{\Delta Z}{r_{kp}}$) as shown in Figure 4.2.

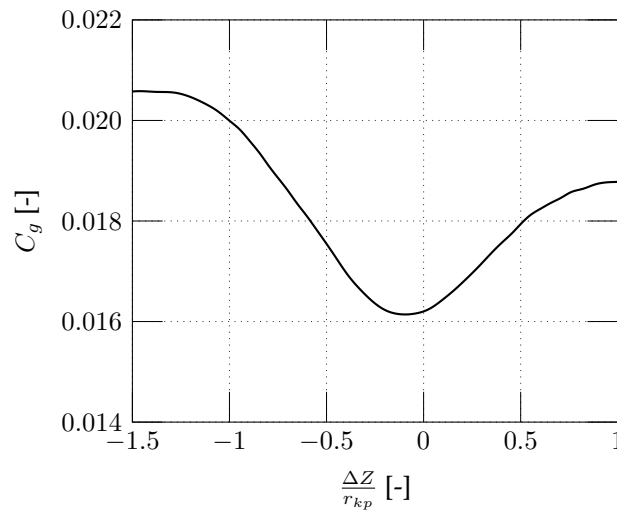


Figure 4.2.: Gas-side heat transfer - correlation coefficient.

The existence of a gas-side carbon layer can substantially reduce the local heat flux and coolant heat input through the insulating characteristic of the carbon layer. However, the presence of a carbon layer subsequent to an engine thrust reduction or shut-down and its transient build-up to sufficient protective thicknesses is questionable, and therefore the thermal resistance caused by the carbon deposition was neglected in the computations. The modeling of radiation emitted from gaseous species in the combustion mixture, specially CO_2 , CO and H_2O and intermediate products is complicated by the fact that significant variations in energy level may cause oscillations in temperature and the geometry of emitting gaseous species is difficult to predict. Barrere [76] and Dobrovolski [32] proposed simplified approaches for estimation of the aforementioned parameters, but it was felt that the additional complexity in the calculations would not necessarily ensure better results. For these reasons and for the purposes of this preliminary analysis, the

contributing factor of radiation to the total gas-side heat input has been disregarded. No attempt was also made to include the enhancement of the heat transfer coefficient due to the dissociation of gas species and their recombination. Using Equation (4.10), gas-side heat transfer coefficient distributions were calculated for the range of mixture ratios and chamber pressures proposed for the individual thrust chamber designs and are presented in the Regenerative Cooling Analysis Section.

4.3.3. Radiation Cooling Analysis

Radiation cooling uses a high-temperature, high-emissivity material and has been mostly applicable to engine nozzle extensions. The wall material radiates heat to the surroundings through the external surface and from the internal nozzle surface. Molybdenum and columbium are typical materials for use up to 1940 [K]. Due to their low emissivity and for corrosion resistance, an additional coating of MoSi_2 is usually applied to the inner and outer walls [75]. The area ratio at which a radiation-cooled nozzle extension can be attached to was calculated by assuming 1750 [K] as the maximum operating temperature for the skirt material. Predicted wall temperatures were based on a simple energy balance:

$$h_g (T_{aw} - T_{wg}) = \sigma \epsilon T_{wg}^4. \quad (4.11)$$

where:

- σ = Stefan-Boltzmann radiation heat transfer constant, $5.67 \cdot 10^{-8}$ [W/m²K⁴];
- ϵ = coating emissivity (assumed value = 0.85), dimensionless.

The proper attachment area ratio was then calculated separately for each operating point and is dependent on mixture ratio and chamber pressure. At the lowest chamber pressure studied, however, this point moves down to the throat region. In order to eventually eliminate a flange near the throat station for these cases, the nozzle cooling channels are extended to an area ratio of at least 6:1, at which point manufacturing methods for joining the nozzle extension to the cooled chambers are simpler.

4.3.4. Regenerative Cooling Analysis

Combining the thrust chamber contour, the gas-side heat transfer distribution, thrust chamber material properties (thermal conductivity, yield strength) and the thrust chamber design conditions (propellant properties, thrust, chamber pressure, mixture ratio, coolant flowrate), regenerative cooling analyses were performed for a number of cases using a computer program developed in MATLAB (see Appendix B). This computer program solves the steady-state one-dimensional heat transfer equations (as described, for example, in the work of Omori et al. [78]) and is capable of either designing or evaluating channel-wall coolant passages in different configurations. Program output includes coolant heat input, coolant pressure and bulk temperature distribution and chamber wall temperature profiles. The design of the copper chamber liner was based upon the gas- and liquid-side heat transfer correlations and taking the fin effectiveness model of reference [79]. These analyses were used to more accurately determine the regenerative cooling limits and can

4. Propulsion System Concept Selection

provide more realistic reference data in the generation of parametric coolant heat input and coolant pressure drop required to perform the engine cycle balances.

Channel Design Constraints

The typical cooling channel configuration for regeneratively-cooled designs utilizes rectangular coolant passages milled axially in a copper alloy (e.g. CuCr1Zr) liner and covered with electroformed nickel. This finned construction add enough area to the coolant side and transform the gas-side heat flux in a lower coolant-side flux and is therefore the preferred configuration. Cooling channels milled in a helix arrangement can be an option in situations which require additional area for heat exchange. These channel-walled chambers normally extended up to a certain area ratio at which the radiation-cooled nozzle could be utilized. The analysis did not impose a minimum channel width due to manufacturing reasons, but assumes a minimum value of 0.25 [mm] because of the clogging potential, since particles in the coolant cannot be entirely filtered. A maximum channel aspect ratio of 20 was generally adopted as the upper limit for state-of-the-art manufacturing methods.

Coolant Correlations and Burnout Limits

Coolant heat transfer correlations for single-phase fluids in forced convection are semi-empirical; as a result, the uncertainties regarding their use beyond the range of supporting test data can be large and must be considered. The critical points, normal boiling points and typical temperatures for LO₂ and LCH₄ are presented in Table 4.1.

Table 4.1.: Representative coolant data.

Parameter	Oxygen	Methane
Critical pressure, [MPa]	51.02	45.98
Critical temperature, [K]	154	191
NBP, [K]	90.17	111.66
Typical inlet temperature, [K]	90	115

Two types of analyses for methane and oxygen at subcritical pressures were performed. In the first, it was assumed that a "vaporizer" section of the nozzle extending aft from an area ratio of ca. 7:1 vaporizes the inlet coolant, so that heat transfer on the coolant side can be taken as forced convection cooling with a gas. The Hines correlation [77] was used in this situation for both propellants:

$$Nu_l = 0.005 Re_l^{0.95} Pr_l^{0.4}. \quad (4.12)$$

where:

Nu_l = coolant Nusselt number;
 Re_l = coolant Reynolds number;
 Pr_l = coolant Prandtl number.

The second analysis considered the inlet liquid oxygen to be either at its normal boiling point (i.e., a saturated liquid) or in a sub-cooled state. Thus analyses for oxygen considered a liquid state at inlet temperatures of ca. 90 [K]. In this case, forced convection was characterized by the standard Colburn correlation:

$$Nu_l = 0.023 Re_l^{0.8} Pr_l^{0.4}. \quad (4.13)$$

where the local coolant Reynolds and Prandtl numbers are assessed at the coolant bulk temperature. This approach does not apply for methane because of the proximity of its boiling and freezing points. Burnout heat flux correlations for methane are given by [77]:

a. For $(V_l \Delta T_{sub}) \leq 1000$:

$$\ddot{q}_{BO} = 0.3 + 0.0004 (V_l \Delta T_{sub}). \quad (4.14)$$

b. For $(V_l \Delta T_{sub}) > 1000$:

$$\ddot{q}_{BO} = 0.58 + 0.00012 (V_l \Delta T_{sub}). \quad (4.15)$$

where:

V_l = coolant velocity, [ft/s];
 ΔT_{sub} = coolant subcooling, [°F].
 \ddot{q}_{BO} = burnout heat flux, [BTU/in²s] (1 BTU/in²s \approx 1634 W/m²).

These expressions suggest that heat transfer by nucleate boiling in the nozzle high heat flux region is rather impractical. The use of methane as a coolant is therefore limited to the supercritical pressure range or as a superheated vapor at subcritical pressure.

Heat transfer to methane at supercritical pressures can be characterized by a correlation originally developed for C₃H₈ [77]:

$$Nu_l = 0.00545 Re_l^{0.90} Pr_l^{0.40} \left(\frac{\rho_l}{\rho_{wl}} \right)^{0.11} \left(\frac{k_l}{k_{wl}} \right)^{0.27} \left(\frac{C_p}{C_{pl}} \right)^{0.53} \left(\frac{\mu_l}{\mu_{wl}} \right)^{0.23} \left(1 + \frac{2}{L/D} \right). \quad (4.16)$$

where:

ρ = density, [kg/m³];
 k = conductivity, [W/m·K];
 C_p = specific heat, [J/kg·K];
 μ = viscosity, [Pa·s];
 L/D = length/diameter for initiation of heating.

with subscripts:

4. Propulsion System Concept Selection

- l = denoting property evaluated at bulk temperature;
 wl = denoting property evaluated at liquid-side wall temperature;

Equation (4.16) was established for coolant pressures from 3.0 to 12.0 [MPa], heat fluxes from 327 to 16342 [W/m^2] and wall temperatures from ambient to 920 [K]. This correlation is able to predict 95% of the data within $\pm 24\%$. Alternatively, a correlation for methane flowing in smooth heated copper tubes is equally suitable for high heat fluxes and coolant operating pressures [80]:

$$Nu_l = 0.022 Re_l^{0.8} Pr_l^{0.4} \left(\frac{T_l}{T_{wl}} \right)^{0.45}. \quad (4.17)$$

Equation (4.17) is applicable between 2.62 to 138.90 [kW/m^2] and for fluid pressures ranging from 26.0 up to 33.0 [MPa]. Reference [80] states that the correlation is consistent within $\pm 10\%$ of experimental error. For computational simplicity and due to the broader experimental base, Equation (4.17) was adopted throughout the analysis.

For oxygen at supercritical pressures, the results of heated-tube tests [81] over a pressure ratio range of 0.39 to 6.76 and a heat flux range of 1.961 to 89.881 [kW/m^2] led to the following "LOX" correlation:

$$Nu_l = Nu_{ref} \left(\frac{\rho_l}{\rho_{wl}} \right)^{-0.5} \left(\frac{k_l}{k_{wl}} \right)^{0.5} \left(\frac{\overline{C_p}}{C_{p_l}} \right)^{0.67} \left(\frac{P_l}{P_{crit}} \right)^{0.2}. \quad (4.18)$$

where P_l/P_{crit} is the coolant pressure ratio with respect to the critical value and the reference Nusselt number is given by:

$$Nu_{ref} = 0.0025 Re_l Pr_l^{0.4}. \quad (4.19)$$

Over 95% of the data used fits Equation (4.18) to within $\pm 30\%$ [81].

In the analysis, heat transfer enhancement factors due to cooling channel curvature were considered following the work of Ito [82]. In general terms, the effect of a curved duct is to enhance the coolant heat transfer coefficient due to secondary flows. Equation (4.20) was employed to calculate such factors:

$$\frac{f_c}{f_s} = Re_l (r/R)^2 = I^{0.05}. \quad (4.20)$$

where:

- f_c = curved pipe friction factor, dimensionless;
 f_s = straight pipe friction factor, dimensionless;
 r = pipe radius, [m];
 R = radius of curvature, [m];
 I = Ito parameter, dimensionless.

The application of the Ito parameter assumes the following forms:

a. For concave surfaces:

$$Nu_e = Nu_l I^{0.05}. \quad (4.21)$$

b. For convex surfaces:

$$Nu_e = Nu_l I^{-0.05}. \quad (4.22)$$

where Nu_e is the modified Nusselt number and Nu_l is given by Equations (4.13) through (4.18).

Coolant Limitations

Oxygen and methane require a limit to the allowable coolant-side wall temperature. Methane can thermally decompose and form the so-called "coke" between a range of temperatures from 1030 to 1370 [K], but since these temperatures are well above the wall temperature limited by structural reasons, no consideration was given in this respect. Although copper oxidation is not expected to occur below about 530 [K], the oxidation rate becomes pronounced at a temperature of 755 [K] [83]. In this analysis, therefore, a maximum temperature of 590 [K] was taken as the maximum allowable temperature for copper materials in contact with oxygen.

With regard to coolant bulk temperatures, one limiting factor for methane is the rapid decrease in density with increasing temperature at small pressure decreases which sets a value of ca. 500 [K] as a practical limitation. The lack of appreciable sub-cooling also limits the channel design. However, the pressure effect is rather strong; for this reason, cooling with methane at high pressures was made without regard to a bulk temperature limit. For supercritical oxygen and methane, maximum acceptable fluid velocity was not allowed to exceed a Mach number of 0.3 locally. For subcooled conditions, and especially for oxygen, the maximum velocity was taken as 80 [m/s].

Coolant Pressure Drop

The magnitude of pressure drop that can be accepted depends on the system characteristics, such as engine cycle and spacecraft weight limitations. A limiting value of pressure drop of 1.5 [MPa] was generally set for both propellants. Minimum outlet channel pressure is defined by the injector pressure drop requirement, defined here as 20% of p_k for preliminary purposes [32]. The total pressure drop in the coolant channels was calculated by the sum of frictional, momentum ("dynamic") and localized (manifold) losses. For each channel segment Δx , the frictional pressure drop Δp_f was calculated as:

$$\frac{\Delta p_f}{\Delta x} = \xi_l \frac{\rho V_l^2}{D_h}. \quad (4.23)$$

where ρ is the fluid density, V_l is the fluid velocity, D_h the hydraulic diameter and ξ_l the coefficient for frictional losses, given by:

4. Propulsion System Concept Selection

$$\xi_l = 0.0055 \left[1 + \left(2 \cdot 10^4 \frac{k_s}{D_h} + \frac{10^6}{Re} \right)^{\frac{1}{3}} \right]. \quad (4.24)$$

where k_s is the surface rugosity, which for channel milling operations can be taken as 1.5 [μm].

The momentum pressure drop reflects the change in kinetic energy of the flow and is generally given by:

$$\Delta p_d = \frac{\rho_{out} V_{out}^2 - \rho_{in} V_{in}^2}{2g}. \quad (4.25)$$

where subscripts *in* and *out* denote inlet and outlet of the channel segment, respectively.

Localized pressure losses, such as those encountered in manifolds and entrances were estimated as:

$$\Delta p_m = K \frac{\rho V^2}{2}. \quad (4.26)$$

where K is the resistance coefficient.

When treating the flow of compressible fluids across a manifold, a correction factor has to be accounted for [84]:

$$\Delta p_m = K \frac{\dot{m}^2}{2847Y \rho_1 d_1^4}. \quad (4.27)$$

where ρ_1 is the fluid density at upstream conditions, d_1 is the upstream flow (hydraulic) diameter, \dot{m} is the coolant mass flow rate and Y is a compressibility factor, taken as equal to 0.60 for both propellants.

Analysis Guidelines and Methodology

The nominal engine design conditions for the analyses were 1100 [N] (vacuum) thrust with a specified nozzle expansion ratio of 60. Parametric specific impulse and thrust coefficient data at the selected expansion ratio and thrust level were generated as functions of chamber pressure and mixture ratio and then input directly to the thermal analysis program. The computer program finally calculated the propellant mass flow rates, throat sizes and chamber coordinates. The study envelope for the analysis is summarized in Table 4.3.

In preparing these guidelines, essentially three factors have been used to identify limitations on regenerative cooling of the thrust chamber. These are a coolant supply pressure requirement, a minimum practical cooling passage dimension and a maximum coolant temperature rise. Additionally, the maximum chamber gas-side wall temperature was limited to 850 [K] for structural reasons.

Methane cooling was evaluated at mixture ratios 2, 3 and 3.5, while oxygen cooling was assessed at $K_m = 3.5$ up to a value of 5. Significant trends are shown graphically in Figure 4.4.

Results for Single-Propellant Regenerative Cooling (Fuel/Oxidizer)

For the proposed LO_2/LCH_4 engine system, there is a slight advantage for oxygen at higher mixture ratios. Methane cooling seems more adequate at lower mixture ratios and chamber pressures. Oxygen cooling can be made at the optimum engine mixture ratio of 3.5 and above, while methane can be potentially used up to mixture ratios of 3.0. Figure 4.4 is a plot of significant parameters at the nominal engine thrust level of 1100 [N] across the range of mixture ratios investigated.

At 1.0 [MPa] chamber pressure, methane gives low pressure drops for mixture ratios ranging from 2 to 3.5. As chamber pressure increases to 2.5 [MPa], an accompanying increase in pressure drop is observed; this tendency also increases with increasing mixture ratios. With oxygen cooling, pressure drop decreases as mixture ratio is increased for a given chamber pressure. Figure 4.4d shows that in order to remain within the bulk temperature rise limit for oxygen, reduced combustor lengths are needed at mixture ratios below 3.5. As less methane is available at higher mixture ratios, combustor length must also be reduced to stay within pressure drop limits as the outlet bulk temperature increases. These limitations can be overcome by cooling with both propellants as will be discussed later. Figure 4.4e shows the trend in channel size versus mixture ratio. Because of lower density, methane channel widths are larger than for oxygen but the difference tends to decrease as mixture ratio increases. Since methane becomes limited by the bulk temperature at higher mixture ratios due to increasing pressure drops, it seems that oxygen cooling is preferred from the engine cycle point of view, even though channel dimensions are smaller.

Various simulations were made starting with LCH_4 as a coolant and using different channel configurations. At the design chamber pressure and thrust (2.5 [MPa]/1100 [N]), cooling with subcritical methane was only feasible at very low mixture ratios (below 2.0). In this case, after being superheated in the lower heat flux region of the nozzle (at an area ratio of about 6), gaseous methane was used to cool the remainder of the chamber. At higher mixture ratios, the coolant bulk temperature exiting the regenerative-cooled portion of the thrust chamber was above 450 [K] for the baseline characteristic length of 1.5 [m]. This bulk temperature makes cooling of the chamber below the allowable Mach number of 0.3 very difficult, if not impossible. Besides, pressure drop with methane as a coolant tends to increase with increasing mixture ratios (see Figure 4.4a). Therefore, it was concluded that within analysis guidelines, cooling with methane at subcritical pressures was not feasible without additional measures, such as the use of thermal barrier coating or a special injector design approach.

Oxygen cooling at subcritical pressures was attempted at the optimum engine mixture ratio of 3.5 using the Colburn (Equation (4.13)) correlation for subcooled LO_2 . The results of this analysis are shown in Figure 4.5. To achieve reasonable cooling with oxygen at this regime, a $0.5 \mu\text{m}$ MnSi_2 thermal barrier was applied to the nozzle extension, with the regenerative-cooled portion starting at the minimum expansion ratio of 6. To help increase the area for heat-pickup, the contraction ratio was increased from 8 to 13 and the cooling channels in the throat region were twisted in 45 degrees with respect to chamber axis (helix flow pattern). To stay within gas-side wall temperature limits a large coolant velocity in the area of the throat is needed, with accompanying large pressure drops.

A different scenario is observed for oxygen cooling at supercritical pressures. Temperature profiles at the optimum mixture ratio of 3.5 are shown in Figure 4.6 for a contraction

ratio of 8. As mentioned previously, to remain within the bulk temperature limit for oxygen, the characteristic length was decreased from 1.5 to 1.1 [m]. Coolant velocities and pressure drops remain well within limits.

Results for the Dual-Propellant Regenerative Cooling

Single propellant cooling seems to be rather limited by oxygen or methane heat absorption capability, as a direct or indirect result of the coolant discharge bulk temperatures. These limitations appear to be significant at low thrust levels, intermediate chamber pressures and optimum engine mixture ratio where the total heat flux is high. Operation at reduced L^* expands the single propellant cooling feasibility; however, the accompanying performance decay makes this approach less desirable. These difficulties can be overcome by (1) use of dual-regen cooling in which both propellants are used in series flow, or (2) use of thermal resistance liners in the thrust chamber to reduce the heat input to the coolant. The simulated dual-regen cooling scheme is shown in Figure 4.7. The calculations show that the use of methane to cool only the combustor section, allows a greater bulk temperature rise and a longer cylindrical section with a potential increase in combustion efficiency. A reduction in coolant discharge temperature from the chamber by either dual-regen cooling which distributes the total heat load to both propellants, or use of chamber coating or liners which reduce the heat flow to the coolant, also increases the feasibility of cooling at higher chamber pressures, which, as a result, tend to reduce engine physical size (and weight).

The use of dual-regenerative cooling has a minor effect on the minimum channel size, since cooling channel hydraulic diameter is controlled by the flow velocities required to maintain wall temperatures in the throat region below the allowable maxima and is not limited by bulk temperature rise, such as in the single-regen case.

4.3.5. Film-Cooling Analysis

The film-cooling analysis had the sole purpose of defining trends in the amount of film coolant required and estimating the corresponding losses in specific impulse. Film-cooling data with methane is meager in the literature; on the other hand, design information with use of space storable propellants is relatively well documented. As an example, Stechman [85] presents useful design criteria for preliminary design purposes and trade-off studies. Curves are presented which define the amount of film coolant required to maintain a certain combustion chamber temperature level. Experimental results indicated that up to 25% of the total available fuel was used to cool the combustor when MMH is used as the coolant. To assess the loss of performance due to gas stratification, the authors employed a model in which no mixing of the flow streams in the core and in the film occurs, whereas still considering the thrust provided by the coolant. This simple model is represented by Equation (4.28):

$$I_{sp} = \frac{(\dot{m}I_{sp})_g + (\dot{m}I_{sp})_c}{(\dot{m}_g + \dot{m}_c)}. \quad (4.28)$$

This expression is valid only if the ratio of specific heats is approximately the same for both the gas and coolant flow streams.

Probably the most important aspect of film cooling is the engine mixture ratio. A decrease in mixture ratio (below the optimum) results in a decrease in the flame temperature and an increase in the relative amount of fuel available for cooling. In the case of LO_2/LCH_4 , the lower fuel density can lead to penalties in system weight, due to the loss of propellant bulk density.

The most desirable condition for film cooling is to minimize the total heat transfer to the coolant, by essentially minimizing the characteristic length. In most cases, however, there is a limit to this decrease, since the combustion efficiency is a function of L^* . In addition, the chamber pressure level will significantly affect the film cooling requirements since the surface area, i.e., heat transfer load and the chamber pressure level, is not linear for a constant L^* . Hydrogen and methane (and similar LPG's), do not have very large heats of vaporization. They do have high specific heats in the gaseous phase, which result in fairly good cooling, but in most cases, this favorable characteristic is negated by the high mixture ratios at which systems using these fuels must operate. For preliminary combustion chamber design purposes, the following equation, based on the work of Kinney et al.[86] and [87] can be used for establishing the liquid coolant amount:

$$\frac{\dot{m}_c}{\dot{m}_k} = 2St_o \left[\frac{L^* C_{pg} (T_{aw} - T_{wg})}{f_k^{1.5} \Delta H_v} \left(\frac{\pi K_p p_k}{P} \right)^{0.5} \right]. \quad (4.29)$$

where:

- \dot{m}_c = coolant mass flow, [kg/s];
- \dot{m}_k = total mass flow, [kg/s];
- St_o = Stanton number, dimensionless;
- C_{pg} = specific heat of the gas, [J/kg·K];
- ΔH_v = methane heat of vaporization (at T_{sat}), [J/kg];

and the Stanton number is that corresponding to smooth pipe flow.

The total propellant flow rate is proportional to the thrust and for a fixed core mixture ratio the film coolant flow rate is proportional to the thrust, i.e.:

$$\dot{m}_c \propto P. \quad (4.30)$$

With the throat area given by:

$$A_{kp} \propto \frac{P}{p_k}. \quad (4.31)$$

or in terms of chamber cross-sectional area:

$$A_k \propto f_k \frac{P}{p_k}. \quad (4.32)$$

The area associated with heat input to the combustion chamber can be generally written as:

$$A_h \propto D_k L_k. \quad (4.33)$$

and assuming that $L_k \approx D_k$:

4. Propulsion System Concept Selection

$$A_h \propto D_k^2 \propto A_k. \quad (4.34)$$

The Siniarev heat transfer correlation (Equation (4.10)) can be reduced to the following terms:

$$h_g \propto \frac{\dot{m}_k^{0.82}}{D_{kp}^{1.82}}. \quad (4.35)$$

$$\propto \frac{\dot{m}_k^{0.82}}{A_{kp}^{0.91}}. \quad (4.36)$$

$$\therefore h_g \propto \frac{\dot{m}_k^{0.82}}{P^{0.91}}. \quad (4.37)$$

For a constant driving temperature ($T_{aw} - T_{wg}$), the amount of heat input per unit time becomes:

$$Q_{in} \propto h_g A_h. \quad (4.38)$$

Hence,

$$Q_{in} \propto f_k \frac{P^{0.09}}{p_k^{0.18}}. \quad (4.39)$$

Equation (4.39) relates the effect of chamber pressure and thrust on the chamber heat input. However, the heat absorption capability is also related to the thrust by

$$Q_{absorb} \propto \dot{m}_c \propto P. \quad (4.40)$$

Using this approach, the required film coolant flow percentage can be determined for various thrust and chamber pressure levels. This trend is shown graphically in Figure 4.8a. As noted, increases in chamber pressure and thrust level have a positive effect on the percentage of film coolant required to absorb the heat loads. This is because of the more rapid decrease in the heat input area than the increase in heat transfer coefficient and also because of the increase in film coolant mass flow rate with thrust level.

The model proposed by Vasiliev et al. [79] was adopted to estimate the survival length of the film and the final mixture ratio at the edge of the boundary layer. The length of film is represented by:

$$L_l = \eta_c \frac{\dot{m}_c}{\pi D_k} \left[\frac{C_{pl} (T_{sat} - T_{0c})}{h_g (T_{aw} - T_{mc})} + \frac{\Delta H_v}{h_g (T_{aw} - T_{sat})} \right]. \quad (4.41)$$

where:

- L_l = liquid film length, [m];
 η_c = film coolant efficiency, dimensionless;
 \dot{m}_c = coolant mass flow, [kg/s];
 D_k = chamber diameter, [m];
 T_{sat} = methane saturation temperature
 at the injection pressure, [K];
 T_{0c} = methane injection temperature, [K];
 ΔH_v = methane heat of vaporization (at T_{sat}), [J/kg];
 T_{mc} = $0.5 (T_{0c} + T_{sat})$, [K].

The film-cooling coefficient is a function of the Reynolds number at the point of film injection and presented in tabular form in Table 4.2:

Table 4.2.: Film-cooling coefficient η_c .

Re·10 ³ [-]	0	1	2	3	4	5
η_c [-]	1.00	0.78	0.64	0.56	0.52	0.50

It is assumed that the mass flow rates of gas and liquid are proportional to the flow areas inside the combustion chamber. In this case, the mass flow of gases in the "core" \dot{m}_{gc} is:

$$\dot{m}_{gc} = \dot{m}_k \left[1 - \frac{(D_k - 2h_0)^2}{D_k^2} \right]. \quad (4.42)$$

where:

- h_0 = thickness of the liquid film at the injection point, [m];
 \dot{m}_k = total mass flow, [kg/s].

In this model [79], the average value of the mixture ratio in the boundary layer changes gradually from an initial value K_{mn} to K'_m when the mixing is complete. The value of K'_m is given by the following expression:

$$K'_m = \frac{K_{mn}}{1 + (K_{mn} + 1) \frac{\overline{\dot{m}_c}}{\dot{m}_{gc}}}. \quad (4.43)$$

where the value $\overline{\dot{m}_c}$ is defined as:

$$\overline{\dot{m}_c} = \frac{\dot{m}_{gc}}{\dot{m}_k}. \quad (4.44)$$

For single element injectors, the value of K_{mn} can be taken as equal to the the global engine mixture ratio. For multi-element injection heads, there is a possibility to organize the mixture ratio inside the chamber so as to improve performance and/or control the chamber wall environment. The change in mixture ratio across the boundary layer from a value $K_m = 0$ to $K_m = K'_m$ (core \rightarrow wall) is given by:

4. Propulsion System Concept Selection

$$K_m^{II} = K_{mn} - (K_{mn} - K_m') \Psi. \quad (4.45)$$

where Ψ is the turbulent mixing coefficient. The mixture ratio of the sub-layer (wall \rightarrow core) is

$$K_m^I = K_m' \Psi. \quad (4.46)$$

If the mixture is formed only by fuel, the turbulent mixing coefficient Ψ varies from zero to unit. Combining Equations (4.43), (4.45) and (4.46) results in the average mixture ratio between the core and the "edge" of the boundary layer:

$$K_m^{II} = K_{mn} (1 - \Psi) + \frac{K_{mn} \Psi}{1 + (1 + K_{mn}) \frac{\dot{m}_c}{\dot{m}_{gc}}}. \quad (4.47)$$

Based on experimental work done in Russia [72] the value of the turbulent mixing coefficient is given by:

$$\Psi = 1 - e^{-k_c \bar{x}^2 \frac{\dot{m}_c}{\dot{m}_{gc}}}. \quad (4.48)$$

where k_c is an experimental factor accounting for the intensity of the turbulent mixing ranging from 0.0005 to 0.002, and

$$\bar{x} = \frac{x - L_l}{h_0}. \quad (4.49)$$

To carry-out the calculations, first a wall temperature (e.g. 1000 [K]) is assumed which allows estimation of the heat transfer coefficient h_g . With the near wall mixture ratio given by Equation (4.46) a new temperature is obtained until convergence between assumed and calculated values occurs. Knowing how the mixture ratio is distributed, Equation (4.28) can be used to estimate the value of the final specific impulse resulting from the film-cooling process. In performing the simulations, the following nominal parameters were used:

Table 4.3.: Film-cooling simulation parameters.

Chamber pressure p_k , [MPa]	2.5
Film injection pressure $p_{\text{film}0}$, [MPa]	2.75
Engine mixture ratio K_{mn} (O/F), [-]	2.8
Contraction ratio f_k , [-]	13
Percentage of coolant flow $100 \cdot \dot{m}_c / \dot{m}_k$, [%]	24.3
Injection slot height h_0 , [mm]	1.00
Methane enthalpy (heat) of vaporization ΔH_v , [J/kg]	$7.67 \cdot 10^4$
Methane injection temperature T_{0c} , [K]	114
Turbulent mixing coefficient k_c , [-]	0.002

An engine global mixture ratio of $K_{mn} = 2.8$ was selected for preliminary purposes to allow for more coolant (fuel) flow and to slightly lower the total gas temperature. Results

of the simulation are shown in Figure 4.8b. Fuel is injected below saturation (sub-cooled) conditions at a station immediately ahead of the injection head. For a slot injection height of 1.00 [mm], a length of film of ca. 32 [mm] "survives" before mixing with the core combustion gases takes place. This leads to an average mixture ratio of $K_m = 1.3$ at about 60 [mm] downstream of the injection point. The potential impact over the value of the specific impulse will be described in the following section.

4.4. Performance Sensitivity

Using the results of the previous thermal analyses and the performance loss model of Section 4.2, an estimate of the specific impulse for each of the cooling concepts was determined. Table 4.4 documents these results. To evaluate the effect of combustor length (injection head \Leftrightarrow throat) the data of reference [88] was used to "calibrate" the assumed η_C^* . In that work, experimental data for doublet injectors running on LO₂ and LNG propellants, showed an increase of roughly 0.15% in C* efficiency for every additional chamber centimeter. Dual-regen cooling produces the highest performance followed closely by supercritical LO₂ single-regen cooling. Computation of the specific impulse with use of film-cooling was made by inspection of Figure 4.8b and Equation (4.28) with additional inclusion of zonal losses.

Table 4.4.: Estimate of specific impulse for the cooling concepts considered.

Cooling concept		Mixture ratio K_m [-]	Combustor length L_{chamber} [mm]	Contraction ratio f_k [-]	Specific impulse I_{sp} [m/s]
Regenerative cooling	Single-regen (LO ₂) [†]	3.5	150.7	8	3329
	Single-regen (LO ₂) [§]	3.5	123.4	13	3310
	Dual-regen (LO ₂ /LCH ₄)	3.5	224.9	8	3347
Film-cooling		2.8	134.6	13	3113

Design chamber pressure $p_k=2.5$ [MPa], thrust $P = 1100$ [N]

Baseline combustor lengths: 202.6 [mm] ($f_k = 8$) and 134.6 [mm] ($f_k = 13$)

[†] supercritical O₂

[§] subcritical O₂

4.5. Applicable Engine Cycle

It is not the scope of this analysis to perform a complete engine power balance or weight trade-offs of potential engine cycle concepts. The discussion that follows simply presents possible options for the mission model proposed.

Applicable engine cycles initially considered were both pressure-fed and pump-fed systems. Regenerative cooling requirements at supercritical pressures rule out pressure-fed systems because of the excessive weight of the propellant pressurizing system. This concept, shown in Figure 4.9a, is more suitable for film-cooled engines and is only marginally

4. Propulsion System Concept Selection

applicable to LO₂ regenerative cooling at higher mixture ratios and subcritical pressures, possibly with use of thermal liners.

If high performance (e.g. higher payload) is desired by mission planners, a departure from conventional solutions to make full use of propellant capabilities is needed. As an example, the new advancements in battery technology, especially of the Lithium-based type for aircraft and automobile propulsion, make pump-fed systems using electric motors powered by batteries a viable alternative. However, depending on detailed mission objectives, the weight of the batteries might still be prohibitive.

It was verified for the dual-regen cooling scheme that methane outlet temperatures range from 450 to 500 [K]. This temperature range is suitable for use as a turbine drive in an expander cycle. This cycle can be modified to include electric motor-driven pumps and a turbo-alternator as the power source as shown in Figure 4.9b. A small amount of the heated methane bypasses the turbine and this bypass flow provides power control. This concept is relatively lightweight, provided that the horsepower of the pumps is low enough to keep the weight of the electrical components down.

A mixed expander/turbo-alternator concept is shown in Figure 4.9c. This concept incorporates the best features of the expander and turbo-alternator cycles. The methane pump is driven in the expander mode by a turbine which eliminates the electric motor required in the pure turbo-alternator cycle. The lower horsepower oxygen pump is driven by an electric motor. Despite these advantages, both the turbo-alternator and the mixed turbo-alternator/expander cycles would require great development time to become operational.

4.6. Thermal Analysis Summary

The applicability of regenerative cooling at the nominal thrust level of 1100 [N] is feasible but will require a departure from standard design practices. Based on the previous thermal analysis, these departures were identified as:

- the use of larger-than-normal chamber contraction ratios;
- the use of cooling channels with high aspect ratio and/or requiring advanced manufacturing techniques;
- the use of both propellants for cooling.

The small mass flow rate available at the required thrust level, combined with the need for high coolant velocities at the design chamber pressure, results in the need for very tiny cooling channel dimensions. In order to maximize the coolant surface area the channels must be rather narrow and deep, rather than shallow and wide as is normally the case in larger engines. The high cooling surface attained by high aspect ratio channels more than compensates for the reduced heat transfer coefficient as velocity is decreased. A helix arrangement of the cooling channels to cater specific zones of high heat flux might be beneficial, but the cost of additional pressure drop needs to be observed.

Use of methane as a coolant proved difficult above mixture ratios of 3.0 at the 1100-[N] thrust level and design chamber pressure of 2.5 [MPa]. For this reason, supercritical oxygen was found to be the preferred coolant due to its higher mass flow rate (LO₂ flow is

3 to 4 times that of methane at optimum engine performance).

If both propellants are used, advantages in performance are obtained. This is because the use of dual-regenerative cooling provides a good solution whenever the limit bulk temperature is exceeded. The second coolant allows an extra chamber length for high performance to be attained without use of film-cooling and permits both propellants to be preheated before injection. The use of thermal liners may additionally help relax the constraints over temperature limits. Finally, with multi-element injection heads there is not only better performance but also a possibility for better near wall temperature control. In other words, the limits of feasibility of regenerative cooling might be shifted depending on how the whole system is conceived.

4.6.1. Final System Recommendation

The final conclusion to be drawn is that the dual-regen cooling is the best cooling concept in terms of performance with single-regen with supercritical oxygen not too much worse and film-cooling delivering the lowest specific impulse. However, with the supercritical pressures needed for regenerative cooling, applicable engine cycles inevitably fall into the pump-fed type. The development of extremely compact, lightweight and reliable turbomachinery seems unrealistic in a short-term. The lower performance delivered by the film-cooled thrust chamber is compensated for by a system which is relatively reliable, low-cost and simple to develop. For these reasons, this propulsion concept became the primary choice for the Mars Lander descent propulsion system.

4. Propulsion System Concept Selection

Regenerative Cooling Analysis Guidelines	
Parameter	Guideline
Propellants	LO ₂ /LCH ₄ at mixture ratios 2 to 5
Engine size	<ul style="list-style-type: none"> ▶ Thrust: 1100 [N] as per mission requirement ▶ Chamber pressures: 1.0 and 2.5 [MPa] ▶ 60:1 area ratio bell nozzle with 5° exit wall angle
Performance	<ul style="list-style-type: none"> ▶ 96% combustion efficiency ▶ 92% thrust chamber efficiency
Combustor geometry	<p>A. Milled channel dimension limits</p> <ul style="list-style-type: none"> ▶ Minimum channel width: 0.25 [mm] ▶ Aspect ratio ≤ 20 ▶ Minimum wall thickness: 0.50 [mm] ▶ Helix angle $\leq 52^\circ$ <p>B. Contraction ratio</p> <ul style="list-style-type: none"> ▶ $8 \leq f_k \leq 13$
Thrust chamber material	<ul style="list-style-type: none"> ▶ Combustor: Copper alloy (CuCr1Zr) ▶ Nozzle: Molybdenum coated with MnSi₂
Thrust chamber temperature limits	<p>A. Gas-side wall temperature</p> <ul style="list-style-type: none"> ▶ 850 [K] for copper alloy ▶ 1750 [K] for nozzle extension <p>B. Liquid-side wall temperature</p> <ul style="list-style-type: none"> ▶ O₂ cooling: 590 [K] ▶ CH₄ cooling: not directly limited
Hot-gas side heat transfer	<ul style="list-style-type: none"> ▶ Siniarev correlation with variable coefficients ▶ Benefit of carbon deposition is neglected
Coolant side heat transfer	<p>A. Coolant inlet temperatures</p> <ul style="list-style-type: none"> ▶ O₂: 90 [K] ▶ CH₄: 114 [K] <p>B. Coolant outlet temperatures</p> <ul style="list-style-type: none"> ▶ O₂ cooling: 400 [K] ▶ CH₄ cooling: not directly limited <p>C. Cooling jacket pressure drop limit</p> <ul style="list-style-type: none"> ▶ 1.5 [MPa] based on engine cycle <p>D. Coolant discharge pressure</p> <ul style="list-style-type: none"> ▶ $\geq 1.2 \cdot p_k$ <p>E. Maximum coolant velocities</p> <ul style="list-style-type: none"> ▶ Liquid: 80 [m/s] ▶ Gas: Mach 0.3

Figure 4.3.: Analysis guidelines.

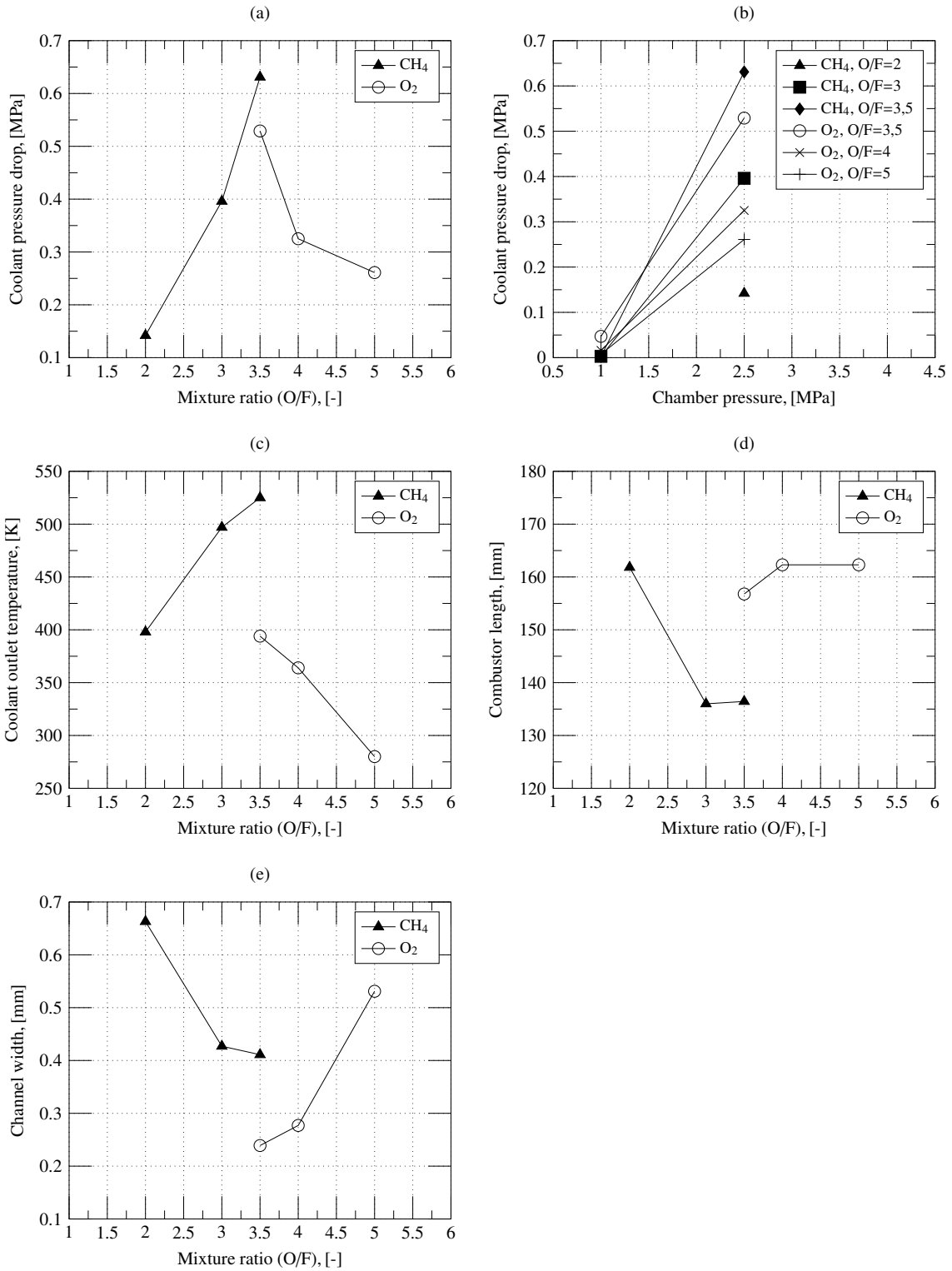


Figure 4.4.: Significant trends for single-regen cooling (fuel or oxidizer).

4. Propulsion System Concept Selection

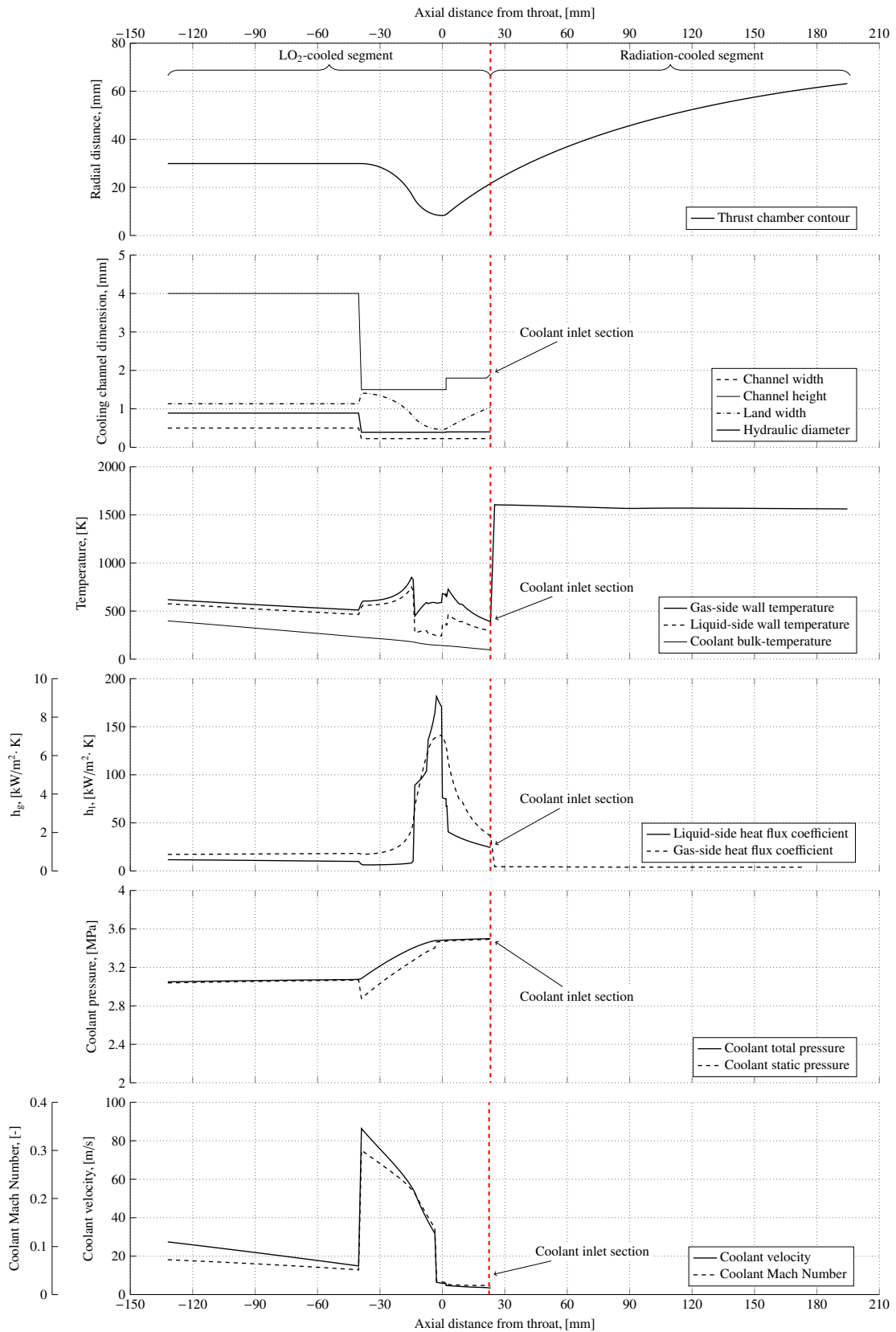


Figure 4.5.: Parameters for the LO₂/LCH₄ thrust chamber, $K_m=3.5$ (O/F), $p_k=2.5$ [MPa], $f_k=13$, subcritical LO₂ cooling.

4.6. Thermal Analysis Summary

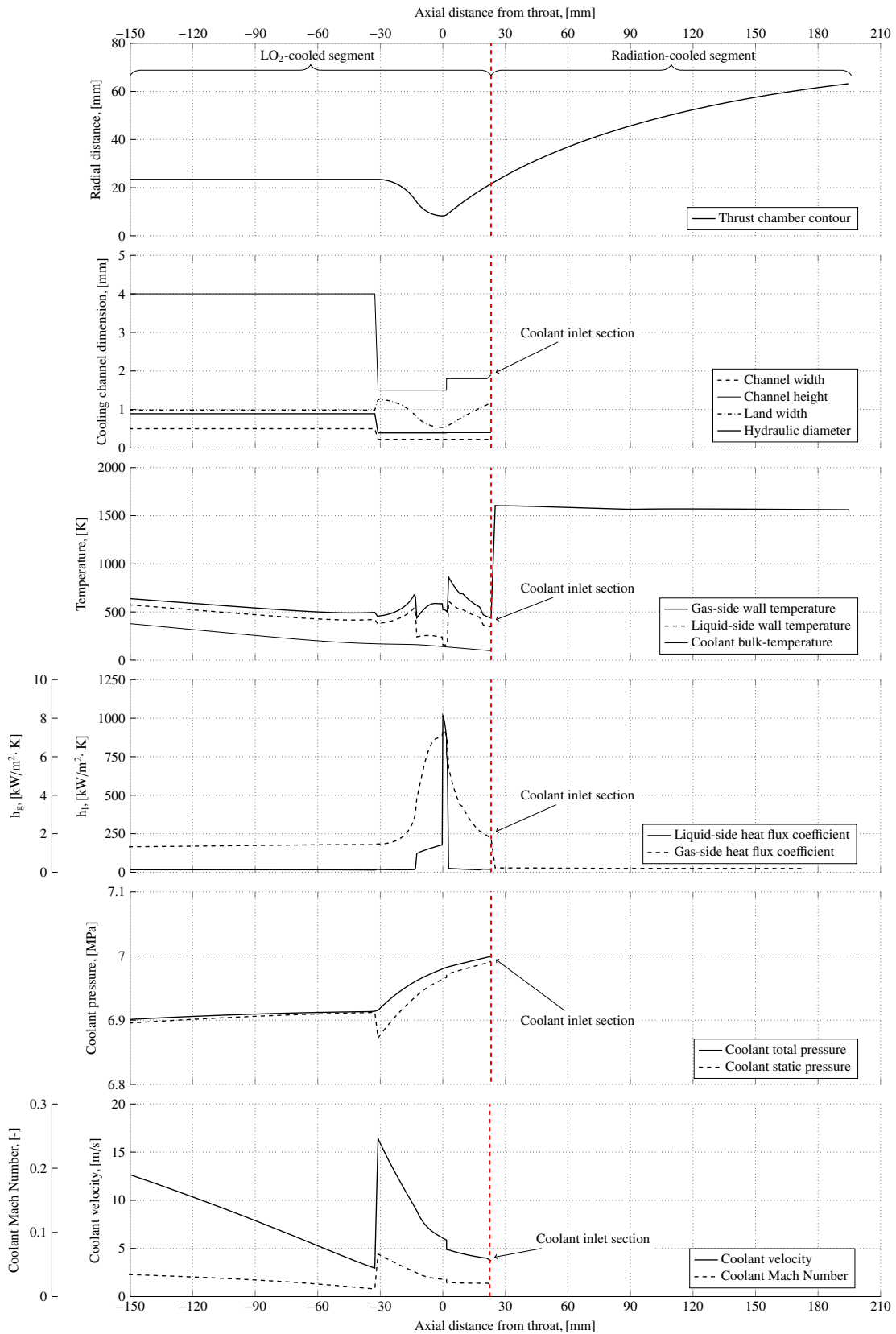


Figure 4.6.: Parameters for the LO₂/LCH₄ thrust chamber, $K_m=3.5$ (O/F), $p_k=2.5$ [MPa], $f_k=8$, supercritical LO₂ cooling.

4. Propulsion System Concept Selection

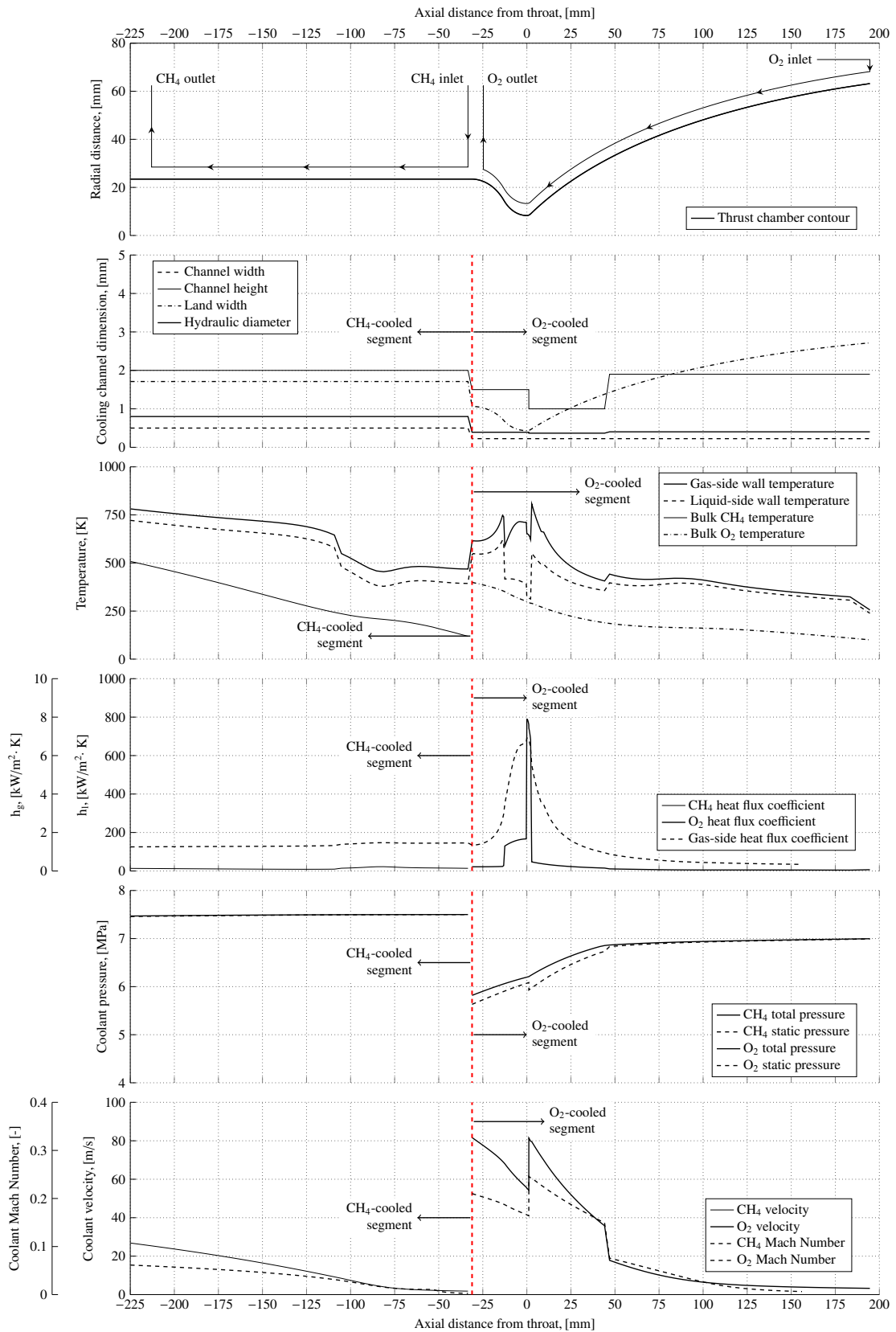
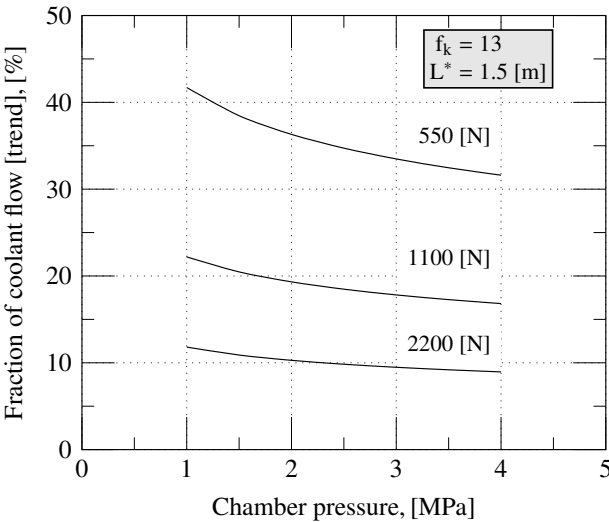
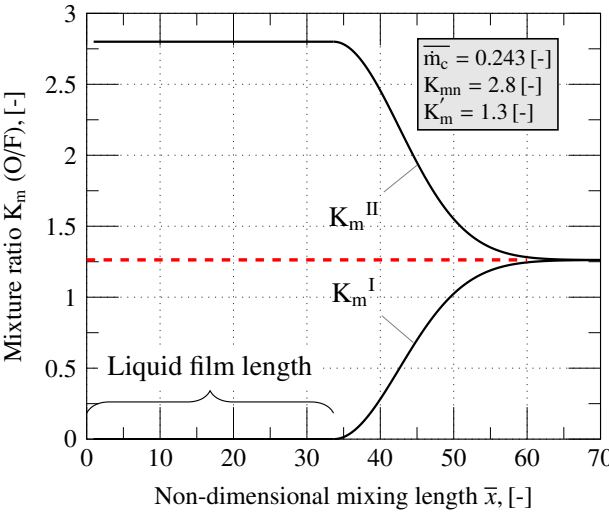


Figure 4.7.: Parameters for the dual-pass thrust chamber, $K_m=3.5$ (O/F), $p_k=2.5$ [MPa], $f_k=8$, supercritical LO₂/LCH₄ cooling.



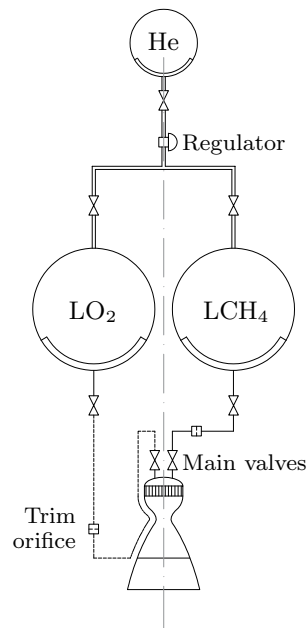
(a) Trend in film coolant flow requirements.



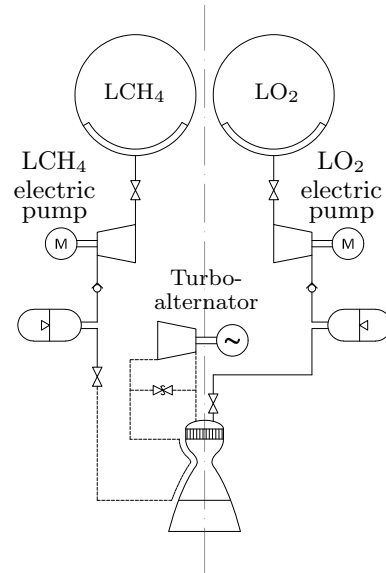
(b) Parameters of the film-cooling simulation.

Figure 4.8.: Film-Cooling Model Characteristics.

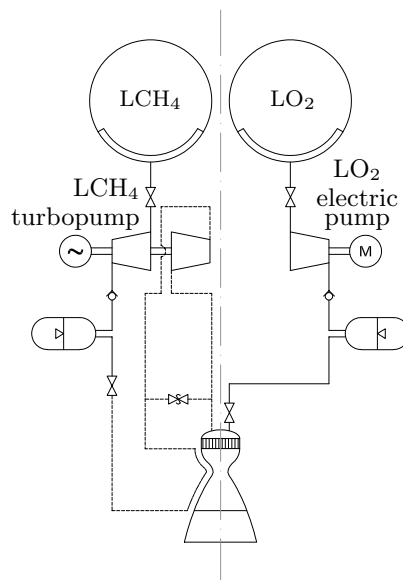
4. Propulsion System Concept Selection



(a) Pressure-fed concept.



(b) Turbo-alternator cycle concept.



(c) Turbo-alternator/expander cycle.

Figure 4.9.: Engine Cycle Concepts.

Part III.

Potential Throttling Concepts

5. Potential Throttling Concepts

Selection and mechanization of a bi-propellant engine throttling concept is basically governed by the desired throttle range, performance requirements and combustion stability issues. Additional factors which influence these decisions are (1) available tank pressure, (2) injector design requirements, (3) chamber pressure characteristics, (4) engine response requirements and (5) thrust linearity requirements. This section includes a comparison of the relative advantages of potential throttling concepts and a summary of the basic operating characteristics of each. Based on this discussion, a method will be selected and recommended for the Mars Lander descent propulsion system.

5.1. Background

5.1.1. Methods of Rocket Engine Throttling

Throttling involves a complex interaction between propulsion system components (turbo-machinery, combustion chamber, injection system, etc.) which as a consequence may severely affect total engine performance. In a general way, the main obstacles for liquid rocket engine deep-throttling (degree of thrust reduction between 8 to 10) inevitably arise from the lower pressures in the combustion chamber leading to low-frequency pressure fluctuations. In addition, in the lower thrust regime, a large decrease in performance is observed and usually only marginal cooling of the combustion chamber is possible. If a pump-fed system is employed, cavitation may occur and overall engine efficiency drops considerably. The throttling function is, therefore, dependent upon the entire rocket engine system. From the fundamental rocket theory, it is known that:

$$P = \dot{m}U_c + A_c(p_e - p_H) = K_p p_k A_{kp}. \quad (5.1)$$

and

$$\dot{m} = \frac{p_k A_{kp}}{C^*}. \quad (5.2)$$

where:

- P = thrust, [N];
- \dot{m} = total propellant mass flow rate, [kg/s];
- U_c = actual exhaust velocity, [m/s];
- A_{kp} = critical nozzle area, [m²];
- A_e = nozzle exit area, [m²];
- K_p = thrust coefficient, [-];
- C^* = characteristic velocity, [m/s];
- p_k = chamber pressure, [Pa];
- p_H = atmospheric pressure, [Pa];
- p_e = nozzle exit pressure, [Pa].

A look at these equations shows that the thrust can be adjusted in two ways: by changing the propellant mass flow rate and/or its density or by changing the geometry of the thrust chamber.

Upstream valving

A conventional throttling method consists in varying the propellant flow only. The application of flow control valves to throttling is a commonly used approach in which the throttling mechanism can be developed separate from the engine at the component level. The basic flow relationship of Equation (5.3) indicates that the flow rate can be controlled by varying either the minimum (throat) flow area or the differential pressure across the valve. The former is generally a more acceptable approach since the pressure losses can be minimized [89]. The advantage of the variable area valve is that at maximum flow rate the valve pressure loss can be reduced to a few Pascals. However, other factors such as flow linearity, engine dynamic coupling and flow controllability usually limit the minimum acceptable pressure drop.

$$\dot{m} = C_d A \sqrt{2\rho (P_{in} - P_{out})}. \quad (5.3)$$

An extension to this type of valve is one in which the pressure at the throat reaches the vapor pressure of the fluid. Through this phenomena the flow rate can be made proportional to the effective flow area ($C_d \cdot A$) of the throat and independent of any downstream resistances (injector, nozzle, filters, etc.). because once the valve has entered into cavitating regime, the lowest pressure reining in the valve is the vapour pressure of the fluid and further reductions in downstream pressure will result in no further increase in flow rate. If cavitation occurs, the pressure drop across the oxidizer and fuel elements can now be set at any value for the purposes of achieving appropriate combustion efficiency. As a consequence, that isolates the problem of controlling the flow rate from the issues of optimizing the operation of the injector. The cavitating valve as a flow control, although it eliminates one source of errors, provides no "panacea" to the throttling problem. It presents limitations and restrictions, one of which is the necessity for a relatively large head loss across the valve (usually about 15% of the upstream pressure). This is compared to a 90 percent recovery (10% loss) design guideline for non-cavitating valves. The use of a cavitating/non-cavitating valve design such as in the Lunar Module descent engine [16] combined the best features of each type. Additionally, in order to obtain good flow recovery characteristics, the length of the ducting downstream of the valve may become too large [20]. However, the achievement of good flow linearity and repeatability in the incipient cavitation or transition region is at best very difficult. The use of throttling cavitating venturi valves with cryogenic liquid fluorine and liquid hydrogen has been investigated [90] and proven feasible. Simply reducing the flow rate of propellant to the chamber will not necessarily result in a smooth reduction in chamber pressure and thrust, because mixing and combustion efficiency are reduced. Therefore, means of increasing or maintain injection velocity (to maintain mixing efficiency) as propellant flow rates are reduced, must be present.

Fixed area injectors

The primary advantage of a fixed-geometry injector is simplicity; the flow of propellants can be regulated by control valves in the propellant lines. On the other hand, there are also difficulties if a fixed injector and a separate flow control valve is used. If the mass-flow rate is reduced, there is a corresponding drop in pressure, down to a reasonable minimum that ensures good atomization and stability at the low end of thrust. Since pressure drop changes in proportion to the square of mass flow, the required initial tank pressure would be prohibitively high. Or, if starting with a feasible tank pressure value, then at the low thrust regime only a meager pressure drop across the injectors would be available and this would be just as disadvantageous. In general, experience and analysis have shown that a nominal injector stiffness ($\Delta p_{inj}/p_k$) should be around 15% to 20% to avoid combustion instability, but can range from 5% to 25% depending on injector type and thermodynamic conditions [91].

Variable area injectors

A second fundamental approach to throttle control is to use the injector element directly. Such elements combine the functions of flow control and atomization, being therefore called "throttle injectors". This type of throttling has been demonstrated with bi-propellant engines through the use of a concentric injector in which a sleeve is used to meter both fuel and oxidizer flow rates [50]. The main advantage to this approach is the total elimination of a separate throttling mechanism and associated pressure loss as well as the integral packaging of throttle actuator and injector. However, if only a variable-area injector is used, one needs to appreciate the effect of tank pressure as well. For example, with a constant tank feed pressure of 3.0 [MPa] and a nominal chamber pressure of 2.0 [MPa] and a variable-geometry element, performing a 10:1 reduction in chamber pressure would impose a high pressure drop across the injector when throttled down to ca. 0.2 [MPa] chamber pressure. As a consequence, very tiny flow passage dimensions would be needed. In small thrust engines, the associated manufacturing problems and poor uniformity of flow represent a major drawback to this approach. Additionally, if multiple injection elements are desirable, such as in a conventional impinging type arrangement, trying to vary the area of many orifices at once will be extremely difficult.

Constant pressure drop injector

As already discussed, one of the disadvantages to upstream throttling (throttle valve) is that the injector pressure drop at the low thrust levels is very small. One method of avoiding this is to use a pressure balanced injector which maintains a relatively constant pressure differential across the injector. This is most easily implemented by spring loaded poppets which are closed off as the fuel pressure downstream of the flow control valve decreases during throttling. Among the disadvantages of such an approach is the possibility of dynamic instability resulting from the combustion, hydraulic and mechanical frequency characteristics. However, efficient injector atomization over the entire throttle range is possible [92].

Combined injector and upstream valving

An entirely different process is observed in a propulsion system that combines both a valve and a throttling injector. At the 10:1 throttle point the pressure drop is $1/100^{\text{th}}$ of the value at maximum throttle or usually on the order of a few Pascals. It is then highly desirable to set the pressure drop across the oxidizer and the fuel in the injector in order to be around the optimum in performance and guarantee stability. Higher reliability and efficiency of the propulsion system is assured if the flow control and injection functions are independent [16]. As mentioned previously, one approach to separate the flow control function to that of the injector is to use cavitating control valves. This is the concept employed by the Lunar Module descent engine in which flow control is done at the throttle valves (cavitating) and optimum propellant injection is achieved by varying the injector setting; a single actuator simultaneously positioned both the valves and the injector.

Engine throat area variation

Decreasing only the throat area A_{kp} leads to an increase in p_k , U_c , K_p , temperature of combustion gases T_k and nozzle expansion ratio A_e/A_{kp} (with $A_e = \text{constant}$) as well as engine thrust. However, increase in chamber pressure at constant propellant feed pressure reduces the pressure drop across the injection elements. As a consequence the mass flow rate \dot{m} decreases and if the characteristic velocity C^* can be taken as constant, the thrust decreases accordingly. So, at first glance, thrust modulation by change of throat area seems advantageous. However, the design of a combustion chamber with a variable throat area presents great difficulties. The dramatic reduction required in A_{kp} imposes significant increase in friction losses and creates great chamber cooling issues. Thrust variations through throat-throttling are not quite effective, as significant changes in the throat area are needed to impart only slight changes in thrust [23]. This area variation can be basically made in two different ways: by use of mechanical devices (a movable pintle) or through gas-dynamic mechanisms, by injecting a gas through holes or slits in the throat and reducing the effective flow area. Additionally, to maintain the nominal operating mode of the nozzle, its expansion ratio has to remain constant. To accomplish this, changes in exit area must be made in proportion to throat area changes.

Combined injector and throat valving (fixed chamber pressure)

A logical step to thrust control is to maintain a constant engine chamber pressure while throttling the propellant flow at the injector (variable area) with concurrent reduction of nozzle throat area as the engine is throttled. This approach has the advantage of maintaining nearly constant performance over the entire throttle range while providing separate flow control. The use of a fixed pressure drop injector in this system would be best since the same pressure schedule would be maintained over the entire throttle range thus allowing complete optimization of performance. In the constant chamber pressure approach it would be necessary to include a position feedback control loop for the injector and a chamber pressure feedback for pressure control.

Gas injection and propellant density variation

From Equation (5.3), it follows that the mass flow can be adjusted by varying propellant bulk density. This method of control is qualitatively different from those considered previously. Emulsification of the propellant at a given thrust level, reduces its density and, according to Equation (5.3) increases pressure drop across the injection elements. Chugging stability margins can therefore be increased and fixed-area injectors may become a viable option. Changes in density can be accomplished, in the case of cryogenic propellants, by flowing it through heat exchangers in the spacecraft, for example, up to the level of saturation. The addition of an inert gas to the propellant, such as helium is also feasible and was demonstrated in an early research by Morrel [93] with the benefit of increased injection velocities. The introduction of gas injection may, however, lead to onset of high frequency combustion instability [92]. Propellant density can also be effected by transitioning to a different propellant type in flight, such as discussed by Kozlov et. al [94].

Pulse modulation

Pulse modulation is used primarily in small thrusters or monopropellant engine systems. This method employs on-off cycling that provides a quasi-steady state average thrust, as described, for example, by Carey [24]. Here, the main issues are related to fast response valves required, dribble volume losses in injector manifolds and feed system between pulses, and an efficient ignition system required for low width pulses, all leading to loss in performance. Thus, pulse modulation is useful for small thrust corrections, such as in spacecraft rendezvous or orbit insertion.

Other methods

Possible alternate approaches to throttling include the use of multiple chambers. The principle of throttling with multiple chambers resides in shutting down one or more chambers or varying the thrust of each chamber independently. Deeper thrust level variation can be obtained by independently throttling multiple chambers by a small amount. A clear disadvantage of this technique results from the feed system complexity and additional structural weight. This method has been adopted in an attempt to reduce manufacturing problems and combustion instabilities associated with large diameter thrust chambers [15], [91].

5.2. Throttling Concept Candidates

This section contains a discussion of the design concepts which were considered as candidates for the Mars Lander descent propulsion system.

5.2.1. Flow Control

Two general methods of throttling were initially considered: (1) those in which thrust of the engine is varied by changing the chamber pressure upstream of a constant area nozzle throat, and (2) those in which chamber pressure is maintained nearly constant by varying

5. Potential Throttling Concepts

the nozzle throat area with concomitant changes in propellant flow rate. As reviewed in Section 5.1.1, the first method is more conventional and requires only a mechanism for varying the propellant flow. The second method has never become operational because of its mechanical complexity even though it offers maximum performance (I_{sp}) at reduced thrust levels. Only those methods of varying liquid flow by mechanical adjustment are considered for further system evaluation. Gas injection, propellant density change and related methods are omitted because of the relatively massive auxiliary systems needed to implement them. Table 5.1 summarizes the throttling schemes outlined above. Such characteristics as system response, weight, actuator forces and flow range variation are used to gauge relative merit. To establish this judgment, reference to [95], [96], [92] and [75] was made.

Flow Control Design Candidates					
Method		Throttling Range	Response	Actuator Force	Weight
Upstream valving	Incremental	10 to 1 or greater	Fair	Moderate	Light
	Continuous	10 to 1 or marginal	Good	Moderate	Light
Injector valving	Incremental	Depends only on number of elements or stages	Excellent	Fairly High	Moderate
	Continuous	10 to 1 or greater	Excellent	Fairly High	Moderate
Upstream + Injector valving	Incremental	10 to 1 or greater	Excellent	Moderate	Moderate
	Continuous	10 to 1 or greater	Excellent	Moderate	Moderate
Variable area throat + Throttle valving		50 to 1 or greater with injector valving	Fair	High	Heavy

Figure 5.1.: Flow control Design Candidates.

5.2.2. Injectors

Propellant injectors considered here are limited to those which inject the propellant into the chamber as liquid jets, sheets or sprays. Mechanical adjustments and flow schemes for performing throttling functions were discussed in the previous section.

Injectors are usually classified by the type of elements used, the pattern of the element array and the manifolding scheme. Generally the type of element determines the size and hydraulic character of the jets, sheets or sprays. The pattern of the array controls the mass flux distribution and to some degree influences the local mass and mixture ratio distribution if the atomizing liquid from adjacent elements overlap. Manifolding can affect the

start and shutdown transients (rate and evenness of flow transients) as well as the hydraulic character of the atomized sprays (different cross-velocities and inlet pressures at the upstream of the elements).

The most basic rule for choosing an injector is whether or not the design supplies propellant in the manner required for highly efficient, stable and reliable operation of the combustion chamber. Practical considerations dictate careful examination of such other factors as favorable ignition conditions, system suitability and ease of fabrication. Injector concepts which permit the designer to precisely control these factors should be emphasized, and those in which they are relatively uncontrollable should be down rated.

Enhancing the reliability of the combustion chamber operation by the choice of injector concept involves secondary effects that are not always very obvious. Firstly, reliable operation implies repeatable injection characteristics; that is, hydraulic properties of the injector should be suitable for calibration, as linear as possible and not subject to wide variations as operating conditions slightly shift [97]. Secondly, the injector design might be able to provide some degree of wall thermal protection or a suitable mixture ratio profile across the chamber radius, if necessary. Reliable ignition depends upon controlled injection which does not "flood" the chamber with one propellant so severely that precludes correct ignition mixture ratio or causes excessive delays.

For this application, system suitability is defined as the pressure loss required and the range of flows over which stable operation is obtained. Minimum pressure loss is desirable in this case so that the active throttling element (valve) has sufficient authority and is as effective as possible in shaping the flow rate profile.

Finally, ease of fabrication implies not only suitability for rapid, low cost construction, but also ease of maintaining critical dimensions and surfaces so that consistency between parts is adequate. Usually these criteria are met by designs requiring no hard-to-machine or join materials, no tight tolerances and no extra smooth surfaces.

The following sections summarize some engineering judgments made relative to these factors for the three classes of injectors considered. These classes expand to form the list of candidates shown in Figure 5.2. A brief description of each type follows.

Pintle type injectors

Much of the history of pintle injector development and application is covered by Dressler and Bauer [50] and again later by Dressler [16]. The pintle injector is normally designed as a single element for the chamber. The central propellant is metered and directed radially outward as individual streams or as a plain sheet from the central pintle body. The outer propellant is injected as a hollow cylindrical or conical sheet which intercepts the central propellant streams. If multiple orifices are used, they usually assume a rectangular or circular shape with part of the outer propellant impinging the radial streams and part of it penetrating between the orifices. This injector has several unique characteristics:

1. The use of coaxial impinging sheets provides relatively uniform circumferential propellant distribution in the combustion chamber;
2. In throttling applications, the single moving sleeve can control the gaps accurately to maintain the proper absolute and relative injection stream velocities over the entire throttling range;

5. Potential Throttling Concepts

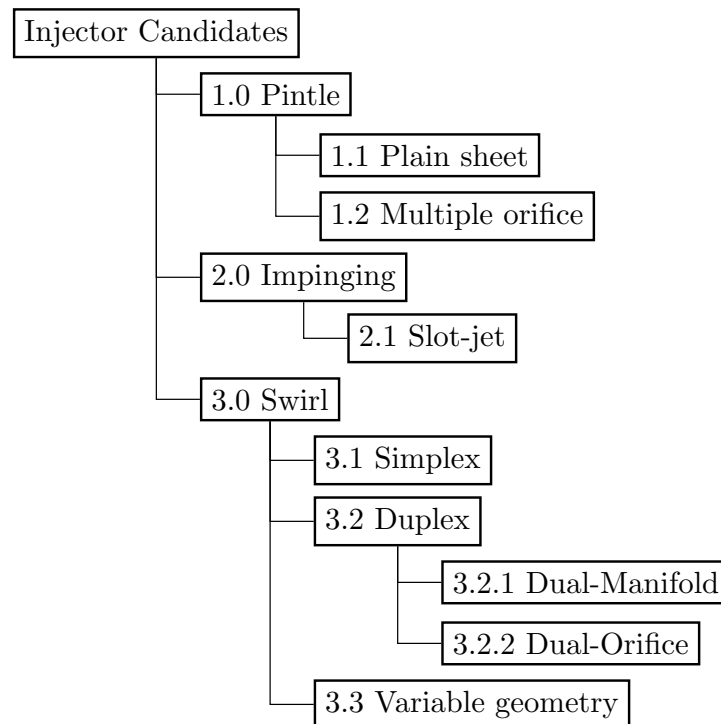


Figure 5.2.: Candidate Injector Concepts.

3. Streaking and uneven heat flux to the chamber, faceplate and throat is minimized by the type of boundary layer generated;
4. For flight-type throttling engines, the injector is not required to be a flow control mechanism - it can be linked to control valves which assume this function - and thus the injector can be adjusted for optimum combustion efficiency;
5. The injector geometry, impingement angles, pressure drops, flow rates and gaps are relatively easy to adjust and/or modify during developmental testing and calibration.

Besides that, no major combustion instability problems were encountered with this configuration. The central-element injector has an inherently stable behavior, because the energy release near the chamber walls where most high-frequency instability modes are sustained is minimized. Design is conducted by referring to traditional impinging type correlations and experimental data because the requisite equations for pintle types are scarce items in the literature. The pintle injector found use in the Lunar Module descent engine [98] and in the MIRA 150A attitude control system on the Surveyor spacecraft [15]. The injector was mechanically linked to flow control venturi valves [20] and to a servo actuator [99]. Drawbacks include a potential poor chamber wall interaction (compatibility) and a rather complex throttling mechanism, see Figure 5.3.

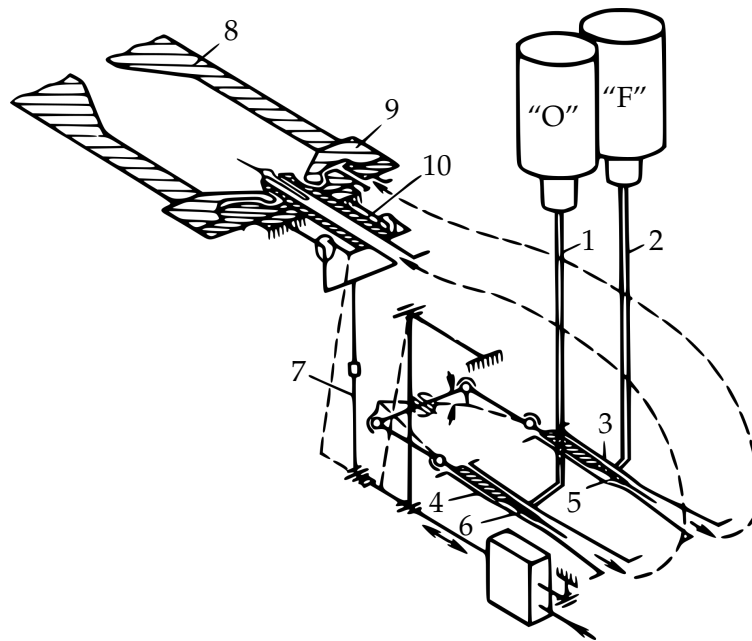


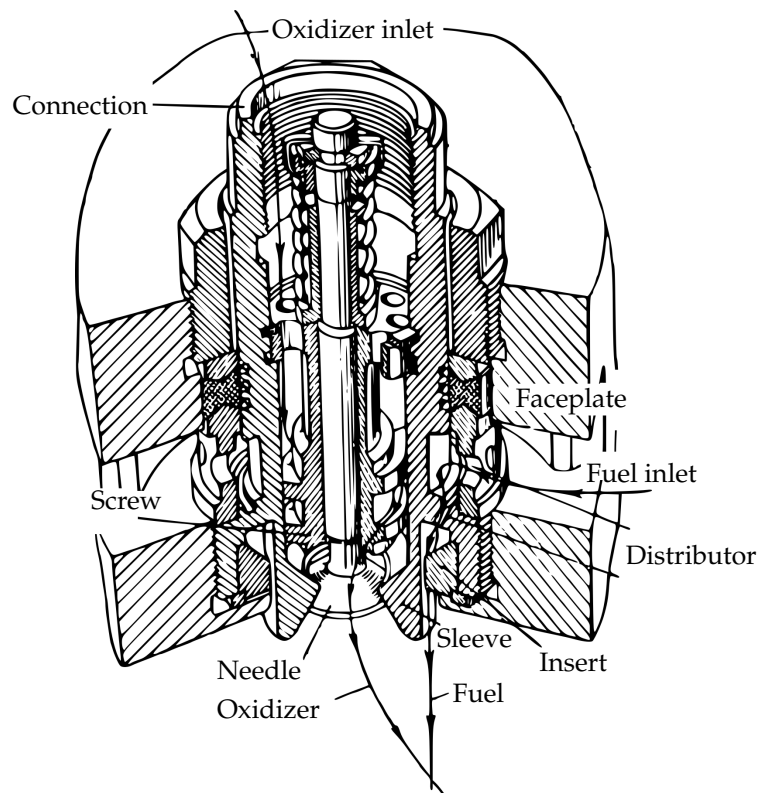
Figure 5.3.: Throttling mechanism developed for the Lunar Module descent engine [92].

Impinging (Slot-jet)

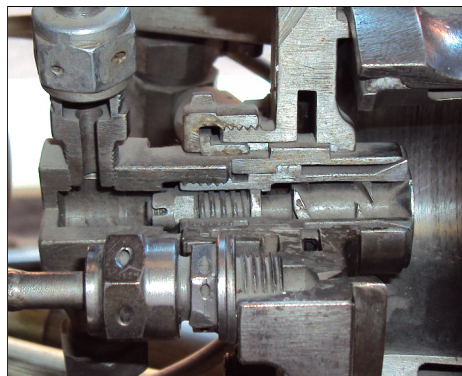
An investigation to examine the performance and operating characteristics of impinging-type variable area injectors over a wide thrust range was conducted by Tomazic [100] in 1955. Six groups of 10 triplet impinging injectors were controlled by a pneumatic valve actuator, which varied the number of triplet sets that were open. A similar mechanism had been previously used in the BMW P-3386 aircraft rocket engine. Another approach to obtain throttling via propellant impingement is to use a needle to control the gaps of fuel and oxidizer streams, such as in Figure 5.4a. That is one of the most widespread ways of throttling diesel and turbojet engines, being somewhat similar in concept to pintle injectors, where impingement provides direct mechanical mixing by dissipative exchange of momentum. The fundamental difference lies in the possibility to employ a multi-element arrangement for smoother thrust variations. The lowest thrust setting is limited by the width of the gap, which for technological reasons, should be kept greater than 0.1 [mm]. Disadvantages include difficulties in obtaining linear behavior of propellant flow as a function of stroke and disruption of stable operation of the chamber by movement of the needle [92]. This injector found special use in the German Walter HWK-109 and Russian RD-3 aircraft rocket engines [101]. In these applications, the central propellant was swirled prior to encountering the outer propellant stream (in a "swirl-jet" configuration), see Figure 5.4.

Simplex swirl type atomizers

Swirl atomizers are considered a low cost and reliable type of atomizer for propellant injection due to its good atomization characteristics and inherently simple geometry. Their design is widely covered in the literature [30], [34] and [33]. An important feature of swirl injectors is their intense dynamic interaction with upstream and downstream perturba-



(a) Swirl-jet type atomizer used in the Walter HWK-109 rocket engine [101].



(b) Similar design employed in the RD-3 rocket engine.

Figure 5.4.: Swirl-jet designs.

tions, as well as instabilities resulting from the atomizer internal flow [102]. A single swirl injector is often referred to as a simplex or pressure-swirl atomizer [103]. These consist of two types: solid-cone and hollow-cone spray simplex atomizers. The solid-cone atomizer atomizes a liquid by swirling it, while most of the flow is allowed to go through a middle cylindrical orifice, providing spray at the center of the spray pattern. The main disadvantage of solid-cone atomizers is the coarse atomization, since the drops in the center of the spray pattern are larger than the drops near the periphery. Hollow-cone atomizers

supply better atomization and their radial liquid distribution makes them the preferred configuration for combustion applications [103].

The characteristic parameters of swirl atomizers are represented by what is called the *geometric constant A*:

$$A = \frac{R_{in} r_n}{n r_{in}^2}. \quad (5.4)$$

where n is the number of inlet channels.

Figure 5.5 is a plot of atomizer discharge coefficient, spray angle and filling coefficient as a function of the geometric constant, following the inviscid swirl atomizer theory established by Abramovich [26].

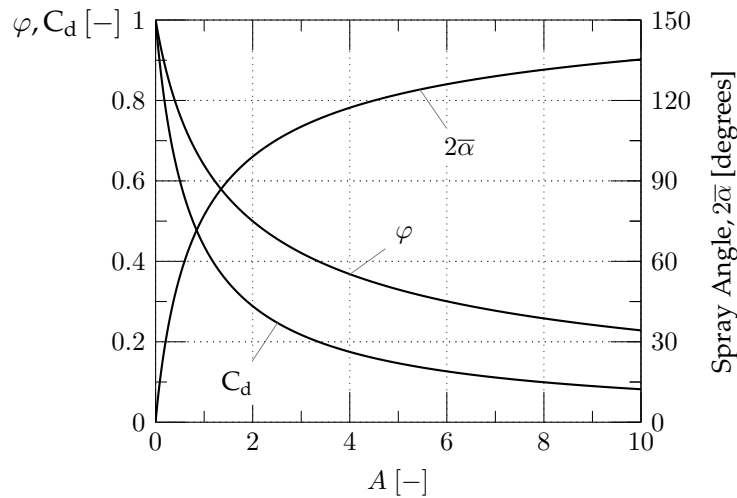


Figure 5.5.: Ideal swirl atomizer parameters as a function of the geometric constant A .

With an injector pressure drop Δp_{inj} of 0.8 to 1.2 [MPa] a throttling ratio δ between 1 to 3 (i.e. "shallow" throttling) can be achieved without much performance loss by use of a throttling valve. Higher throttle values will require correspondingly higher pressure drops. If a constant pressure drop is maintained, no propellant flow change is possible. However, in sectional and multi-element injection heads, on average, a constant pressure drop can be maintained and a 10:1 step change in thrust is achievable. By reducing the flow rate through the injector results in a decrease in Δp_{inj} and a deterioration in spray quality. The geometric characteristic of the nozzle A lies usually between 0.5 and 10 with a corresponding discharge coefficient $C_{d,inj}$ between 0.1 and 0.4 and a total cone angle 2α ranging from 60° to 120° . For a constant A , flow coefficient $C_{d,inj}$ and spray angle 2α remain constant for a relatively wide range of pressure drops Δp_{inj} .

Dual-manifold swirl atomizers

Dual-manifold swirl atomizers belong to the so-called duplex swirlers with dual-stage feeding. They have been primarily used in gas turbine engines because they can enlarge the range of flow variation by up to 25 times [34]. Their use in liquid propellant rockets

5. Potential Throttling Concepts

was investigated by Bazarov [19]. In the low thrust end (small flow rate) the propellant is fed through the tangential orifices with small radius r_{in1} and the atomizer geometric constant A_1 assumes the form:

$$A_1 = \frac{R_{in} r_n}{n_1 r_{in1}^2}. \quad (5.5)$$

The value of A_1 is high and denotes a small value of the discharge coefficient with pressure drop being sufficient to ensure good atomization. When propellant flow rate is increased via a throttle valve connected to the secondary manifold, the atomizer is fed via both the small and large orifices which leads to a decrease in the geometric constant:

$$A_2 = \frac{R_{in} r_n}{n_1 r_{in1}^2 + n_2 r_{in2}^2}. \quad (5.6)$$

The lower value of A_2 corresponds to a high value of the discharge coefficient and spray angle. The large variation in spray angle is a clear disadvantage of the dual-manifold atomizer. The angle may decrease drastically when the second supply comes into play. Another disadvantage is the loss occurring due to mixing of swirling flows with different velocities inside the atomizer chamber [92] which leads to deterioration of the spray quality. This non-uniformity of flows inside the chamber can be minimized by using two-chamber atomizers which are fed almost independently from each other. Reducing the wetted surface and volume of the atomizer chamber (i.e. fluid residence time) may also help improve performance as described by Bazarov [19].

Dual-orifice swirl atomizers

Another type of duplex swirler is the dual-orifice atomizer. This constitutes basically two simplex atomizers connected in parallel [30]. Propellant is fed via two coaxial swirl chambers and is exhausted by two coaxial outlet nozzles. For low propellant flows, only the inner swirler is fed. Throttling the flow to the second group of orifices regulates the thrust level. The flow rate is controlled through the variation of the discharge nozzle section. The throttling range equals:

$$\frac{\dot{m}_{\max}}{\dot{m}_{\min}} = \left[1 + \left(\frac{C_{d2}}{C_{d1}} \right) \left(\frac{r_{n2}}{r_{n1}} \right)^2 \right] \sqrt{\frac{\Delta p_{\max}}{\Delta p_{\min}}}. \quad (5.7)$$

Advantages of the dual-orifice atomizer are:

1. The range of thrust variation is potentially larger than for dual-manifold and variable geometry atomizers;
2. The flow rate is relatively uniform;
3. The spray angle remains practically constant when transitioning from low to high thrust mode.

One disadvantage lies on the fact that during opening of the throttle valve, spray quality might momentarily deteriorate, e.g. a decrease in combustion efficiency can occur.

Variable geometry swirl atomizers

The operation of variable geometry swirl atomizers is based on the fact that the inlet orifices are blocked or opened for throttling. By inspecting Equation (5.4) it follows that a change in atomizer geometric constant A is imparted when the total area of inlet orifices is modified. The change in A results in a change in discharge coefficient and propellant flow. This approach was investigated by Tomazic [100]. Khavkin [30] applied the idea for a screw type atomizer where a four-stage screw is depicted. Modification of the geometric constant is achieved by shaping the thread, the screw body or both. Changing the geometry of the screw causes a change in the degree of twist of the liquid, the thickness of the film at nozzle outlet and, consequently, to changes in the average diameter of droplets in the spray. The injector consists of two main parts: the housing and the four-stage screw. Inside the housing, four cylindrical steps are bored defining diameters D_{in1} , D_{in2} , D_{in3} and D_{in4} . Usually, a multiple-start thread is adopted and the thread itself assumes a rectangular-triangular cross-section. Operation is as follows: departing from the lower position, corresponding to the first stage, the axial movement of the screw brings consistently the second, third, and fourth stages into operation. Disadvantages of this type of injector reside in the complex design of the screw, the special tooling and high machining precision required for a satisfactory alignment between the housing and the threaded body. Besides, the behavior of propellant flow is not strictly linear with stroke, as experimental data revealed [92]. Despite these disadvantages, a throttling ratio of up to 100:1 is possible and if upstream and injector valving are used for flow control, an almost constant spray pattern is ensured.

5.3. Design Concept Comparison and Selection

The design concepts discussed in the preceding sections were combined into a number of potential system designs for the Mars Lander descent propulsion. The criteria used in screening the design concepts for this comparison were drawn based on four definite questions:

- (1) Concept Feasibility: What is the intrinsic feasibility of the design concept?
- (2) Mission Performance: What is the estimated ranking of conceptual systems in terms of total propulsion system weight for a typical Mars Lander Mission?
- (3) Propulsion System Performance: Is there enough technical evidence that the concept can provide high performance, stable and reliable operation?
- (4) Development required: How much development is needed to make the concept an operational reality?

For each system concept considered and listed in Table 5.1 questions (1) to (4) were asked.

Table 5.1.: Throttling Concept Comparison Chart.

Injector concept	Flow Control Concept							
	Upstream valving	Score	Injector valving	Score	Upstream valving + Injector valving	Score	Throat throttling + Injector valving	Score
Pintle type	SA	10	MD	5	ED	1	ED	1
	HF	20	HF	20	HF	20	QF	2
	6	18	6	18	8	24	9	27
Impinging (Slot-jet type)	SA	10	MD	5	MD	5	ED	1
	HF	20	HF	20	HF	20	QF	2
	5	15	5	15	6	18	8	24
Swirl Simplex	SA	10	-	-	-	-	-	-
	HF	20	-	-	-	-	-	-
	5	15	-	-	-	-	-	-
Dual-Manifold	-	-	SA	10	MD	5	ED	1
	-	-	HF	20	HF	20	QF	2
	-	-	5	15	6	18	7	21
Dual-Orifice	-	-	SA	10	MD	5	ED	1
	-	-	HF	20	HF	20	QF	2
	-	-	6	18	7	21	8	24
Variable-geometry	-	-	MD	5	ED	1	ED	1
	-	-	RF	10	RF	10	QF	2
	-	-	6	18	7	21	9	27
Development required (weight 1): SA = state-of-the-art (10 points) MD = moderate development (5 points) ED = extensive development (1 point)			Concept feasibility (weight 2): HF = highly feasible (10 points) RF = relatively feasible (5 points) QF = questionable feasibility (1 point)			Estimated performance (weight 3): 10 = high performance 1 = low performance		

5.3.1. Discussion and Recommendation

Over-all engine performance would be greatly improved for a variable-thrust engine if the gas flow at the throat were also throttled to maintain constant chamber pressure. This, coupled with liquid throttling at the injector would potentially result in a highly efficient variable thrust system. However, the throat throttling method was discarded altogether since structural and cooling problems of a variable throat would probably require considerable research and development. At the required thrust of 1100 [N] and consequent low mass flow rates involved, chamber cooling would be even more difficult to accomplish. This system is also heavier than the other concepts.

The somewhat conventional upstream flow control and fixed-area injector system has been selected for further investigation due to the separate flow control component (valve) capability and the near-term development limitation. Future missions, however, might be more effectively fulfilled by using the variable-area-injector control approach which will reduce both the number of components and the required tank pressure. This approach is, therefore, recommended for future applied research investigations.

With respect to the injection system, simplex swirlers cannot fulfill the 6:1 throttling requirement without spray deterioration or high pressure drop unless a multi-element injection head is employed; variable geometry swirlers are hard to manufacture and complex to develop. For these reasons they did not survive the screening. However, dual-manifold or dual-orifice swirlers remain as attractive options for a variable-area injection system.

Slot-jet (or swirl-jet) impinging type atomizers are similar to pintle injectors in concept but their stability characteristics are questionable.

For these reasons, and due to its ease of fabrication, heritage and relatively good stability and performance characteristics, the pintle injector design has been selected for the purposes of this research. Once the fixed area version of this injector is characterized for LO₂/LCH₄ operation, demanding requirements dictating injector area change can be more directly addressed.

5.4. Conclusions

To round out the discussion of throttling concepts, the conclusions are:

- A conventional upstream flow control and fixed-area injection system is the initial choice for the Mars Lander descent propulsion system and shall fulfill the minimum 6:1 throttling requirement. The decision is based on simplicity and relatively short development time;
- The injector will be based on a fixed-area pintle type. The design shall have provisions to represent changes in case future mission requirements indicate that injector area variation is additionally desirable.

Part IV.

Hardware Design and Description

6. Hardware Design and Description

Following selection of propulsion system and throttling concepts, this chapter summarizes hardware design for subsequent cold-flow and hot-fire characterization.

The nominal engine conditions for the test hardware were 500 [N] thrust with a specified nozzle expansion ratio of 4 and a chamber pressure of 2.5 [MPa]. The thrust level differs from the nominal value of 1100 [N] established by the mission model to give more allowance for spacecraft/lander layout changes and because it may be desirable to adopt this engine size for, e.g. attitude control. The reduced thrust also seemed more appropriate to the existing propellant supply capabilities at the Institute's test facility.

6.1. Injector Design

Selection of the injector concept for this research was qualitatively based on the decision matrix of Section 5.3, and was strongly influenced by pintle injector resistance to damaging modes of combustion instability. Heritage is often an abused factor and therefore every design aspect must be carefully evaluated. As an example of this, the work of Kazuki et al. [104] revealed the pintle concept to be not completely immune to unstable behavior.

The pintle injector design is based on obtaining a proper mechanical interaction of the propellants which forces mixing to occur [107]. Selection of an oxidizer-centered or fuel-centered pintle design can be established in terms of propellant combination and thrust level. For the present research, all configurations were designed and tested as LO₂-centered. The injection parameters for this type of injector which show a dominating influence on injector performance were identified as follows [105]:

1. Ratio of oxidizer to fuel injection momentum;
2. Ratio of secondary oxidizer flow to primary orifice flow, if any;
3. Number, size and shape of oxidizer orifices;
4. Elemental spacing of oxidizer orifices;
5. Location of secondary oxidizer orifices;
6. Injection pressure level and mixture ratio.

Variation of these parameters are used to control both performance and chamber wall environment. As part of the analysis of the injector design, the effects of geometry, momentum ratios, velocities and pressure drops were studied. The results of these analyses were used to establish the basic dimensions of the injector. All injector configurations were designed for liquid-liquid injection, i.e. for sub-critical injection temperatures and pressures.

The specific injector configuration selected for this research was arranged so as to provide high flexibility and permit variations of injection parameters to change mixing and distribution characteristics, see Figure 6.1.

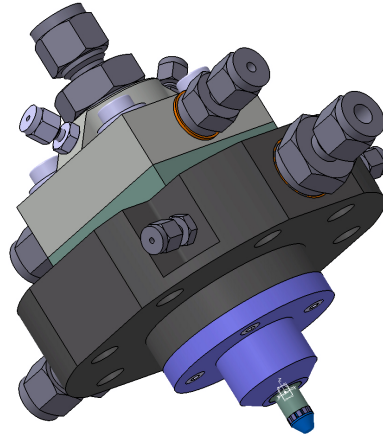


Figure 6.1.: 3-D view of pintle injector.

This “building block” approach also provided a means of using separate parts that could undergo inexpensive modifications. The oxidizer injector orifices, for instance, form a replaceable ring structurally held between the pintle tip and the pintle sleeve (LO₂ flow passage). Oxidizer injection area variation was effected by replacing these rings. Initially, rectangular (slotted) and circular orifice shapes were selected. Rectangular geometries are preferred, because they lend themselves to ease of machining and throttling. Despite the potentially higher surface area for propellant reaction, no continuous sheet configurations were considered. In all configurations tested, the fuel injection point was an annular gap whose metering area could be adjusted by changing spacers located between the injector body and the pintle sleeve.

6.1.1. Injection and Combustion Design Considerations

Once proper attention has been given to the design factors which affect propellant distribution, the additional combustion processes (i.e., atomization, vaporization and chemical reactions) with the pintle injector are similar to the other multiorifice, impinging type injectors. Factors such as stream momentum ratios and basic jet characteristics (injector hydraulics) must be then optimized.

The injector design factor involves stream momentum ratio (TMR) as a measure of the inherent propellant energy available for mixing and atomization. This ratio is simply [14]

$$TMR = \frac{F_o}{F_f} = \frac{\dot{m}_o V_o}{\dot{m}_f V_f}. \quad (6.1)$$

Following reference [106], the proper areas for the fuel and oxidizer are obtained through a more elaborate examination of the initial interaction mechanics. For a slotted orifice configuration, the following interaction model can be used, with the fuel force on the oxidizer taken as:

$$F_f = \rho_f V_f^2 t_f [W + 2LC]. \quad (6.2)$$

where t_f is the thickness of the annular propellant film sheet, L is the slot height and W the slot width. The parameter C is a cross influence term to account for the side interaction of the fuel acting on the oxidizer [107]. On the basis of a single reflective interaction between elements for a fuel particle a first approximation to C is given as [106]:

$$C = \left(\frac{L}{V_f} \right) \left(\frac{a}{S} \right) \left[1 - \left(\frac{NS}{\pi d_p} \right) \right]. \quad (6.3)$$

where N is the number of slotted orifices, S is the spacing between two adjacent primary orifices and d_p the diameter of the pintle tip.

The factor C can be seen to be an estimate of the ratio of time of flight of the fuel to the dispersion of the reactants [97],[107]. The value of parameter a is a measure of the velocity of a disturbance, which does not considerably change with mixture ratio and ranges according to reference [107] between 183 [m/s] and 244 [m/s] for combustible mixtures. For design purposes, a general value of 200 [m/s] for LO_2/LCH_4 was selected. The oxidizer force on the fuel is given by:

$$F_o = \rho_o V_o^2 WL. \quad (6.4)$$

Therefore, the final momentum ratio of the rectangular orifice configuration is:

$$\frac{F_o}{F_f} = \frac{\rho_o V_o^2 WL}{\rho_f V_f^2 t_f [W + 2LC]}. \quad (6.5)$$

Similarly, for a single row of circular orifices, the fuel force on the oxidizer is:

$$F_f = \rho_f V_f^2 t_f d. \quad (6.6)$$

and the force of the oxidizer acting on the fuel is:

$$F_o = \rho_o V_o^2 \frac{\pi d^2}{4}. \quad (6.7)$$

Leading to a momentum ratio given by

$$\frac{F_o}{F_f} = \frac{\rho_o V_o^2 \pi d}{\rho_f V_f^2 4 t_f}. \quad (6.8)$$

6.1.2. Design Criteria

Despite recent efforts [109], [110], [49], there are very little design criteria applicable directly to pintle injectors. In this respect, references [97] and [105] provide useful guidelines and references [106] and [111] give fundamental information applicable to impinging types. Stability considerations are covered essentially by Harrje and Reardon [91], pages 366 through 368.

Geometric parameters

The geometric layout of pintle injectors include some relevant parameters, such as:

1. Blockage factor \rightarrow ratio of total hole or slot circumferential length divided by the circumference of the pintle. In equation form, for circular orifices

$$BF = 100 \left(\frac{Nd_o}{\pi d_p} \right). \quad (6.9)$$

where N is the number of holes in the pintle tip, d_o is the hole diameter and d_p is the pintle diameter. In some pintle designs, a group of secondary orifices may be arranged adjacent to the primary holes/slots. These are usually smaller in size and are placed between the gaps formed by the primary orifices.

Similarly, for rectangular orifices:

$$BF = 100 \left[\frac{(N_{po}W_{po} + N_{so}W_{so})}{\pi d_p} \right]. \quad (6.10)$$

where N_{po} and N_{so} are the number of primary and secondary orifices, respectively; W_{po} is the width of primary slots and W_{so} the number of secondary ones.

2. Pintle diameter \rightarrow the selection of a pintle injector diameter includes consideration of:
 - The ratio of pintle-to-chamber diameter that provides sufficient radial reaction time and stability [91],[105].
 - The resultant fuel sheet thickness at the design fuel pressure drop;
 - The resulting pintle circumference length available for locating the oxidizer injection orifices.

Typical values range between 3 and 5 [52]. The Lunar Module Descent Engine employed an estimated value of 3.3 whereas for the MIRA 150A an apparently large value of 7.6 was adopted [92].

3. Skip distance \rightarrow defined as the length required for the annular sheet to travel in order to impinge the radial streams of propellant. According to Yang et al.[105], a typical value for the *skip ratio* (=skip distance/pintle diameter) should be around 1, since large distances are prone to cause film deceleration and too short a distance might cause the spray to impinge directly on the faceplate. This parameter would prove crucial in subsequent hot-fire experiments.

Momentum Ratio

The guidelines presented by Elverum and Staudhammer [111] and Rupe [106] can be used to initiate the mixing and combustion analysis. These studies indicated a maximum in performance when the individual droplets being of mixed constituents meet at the peak

or design mixture ratio. For this to occur to the maximum extent possible requires optimum use of the propellant stream momenta. Reference [97] extends this to pintle types and states that the ratio of dynamic interaction between fuel and oxidizer streams at impingement must equal one. Expressions (6.5) and (6.8) suggest that performance can be controlled through oxidizer element sizing and unit spacing as well as fuel sheet thickness. The unit spacing is selected on the basis of achieving adequate fuel penetration. Additional performance tuning can be accomplished by the addition of secondary oxidizer elements between the major primary elements or introduction of swirl to one of the propellant flows. The assumption of unit TMR was considered at the present design due to lack of better supporting data for LO_2/LCH_4 . Thus,

$$\frac{F_o}{F_f} = \left(\frac{\rho_o V_o^2}{\rho_f V_f^2} \right) \left(\frac{A_o}{A_f} \right) = 1. \quad (6.11)$$

Therefore, on the basis of this design approach, it was established that the optimum velocity ratio for LO_2 and LCH_4 at the nominal mixture ratio $K_m=2.8$ is:

$$\frac{V_o}{V_f} = \frac{1}{\dot{m}_o/\dot{m}_f} \approx 0.35. \quad (6.12)$$

Figure 6.2a shows this result graphically. Contrasted with the earth storable type propellants which have velocity ratios of 0.6 to 0.7, it is seen that the gross fuel momentum interchange (with the oxidizer) is considerably less with the LO_2/LCH_4 propellant combination. This means that with the relatively low oxidizer velocities, it might be important to control the LO_2 dispersion early in the atomization/mixing process to achieve high performance [111].

So far, the discussion has applied only to a generalized injector. The following design guidelines were integrated to form the basis for element sizing:

- ▶ Minimum annular gap greater or equal to 0.10 [mm] at full thrust;
- ▶ Minimum injection pressure drop equal to 0.10 [MPa];
- ▶ Maximum injection pressure drop equal to 0.80 [MPa];

The first criterion was established as a practical limitation, since ultra-thin sheets of fluid flow require excessive amounts of machining and alignment care. The latter two criteria were the result of system application considerations. The pressure drop cannot be reduced much below the lower limit without feed system coupled "chugging" occurring [112]. The upper boundary pressure drop was considered a practical limit for pressure-fed systems. By initially considering the continuity equation and propellant injection at their normal boiling point temperatures and the flow area-pressure relationship we obtain:

$$C_d A = \left[\frac{\dot{m}}{2\rho\Delta p} \right]^{1/2}. \quad (6.13)$$

where C_d is the average injector discharge coefficient, A is the flow area, \dot{m} is the propellant mass flow rate and Δp is the pressure drop across the element. It is found from Equation (6.13) that the propellant injection area requirements are small for a 500-[N] thrust class

engine. However, the area is a function of oxidizer and fuel pressure drops selected, and these parameters must be matched for mixing performance. Figure 6.2b represents the effect of pressure drop ratio at the nominal mixture ratio on TMR. Methane injection pressure drop turns out to be more than twice that of oxygen to fulfill optimum criteria. Therefore, pintle injector designs based upon this underlying principle should provide peak performance at the optimum momentum ratio as defined by Equations (6.5) and (6.8).

The injector orifice diameters, metering angles and gaps were then designed and adjusted to provide a nominal pressure drop for oxidizer and fuel as shown in Figure 6.2c. The oxidizer to fuel momentum ratio, should ideally be kept approximately equal for the entire thrust range. As chamber pressure (e.g. thrust) is decreased an accompanying increase in injector stiffness is observed as shown in Figure 6.2d. As mentioned elsewhere, this is to keep the necessary margin from low-frequency instabilities at low chamber pressures and to maintain a minimum pressure drop required for satisfactory atomization.

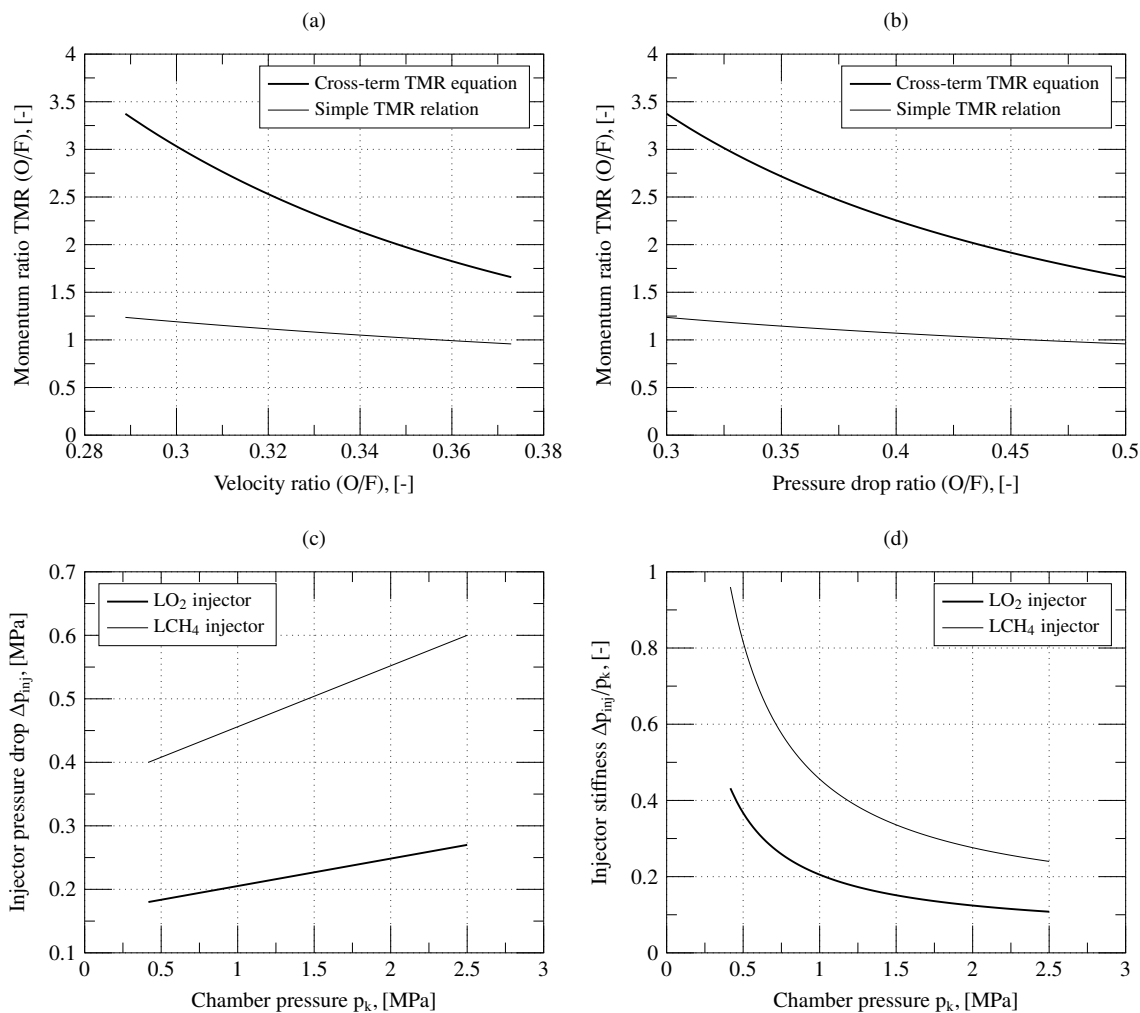


Figure 6.2.: Parameters for the baseline pintle injector design.

6.1.3. Design Summary

Using Equations (6.11), (6.5) and (6.8) and input data of Table 6.1, design calculations were performed for the subject 500-[N] injection assuming two different oxidizer and fuel flow settings. Tables 6.2 and 6.3 present a summary of these calculations.

Table 6.1.: Injector Input Design Data ($p_k=2.5$ [MPa] / $K_m=2.8$)

Parameter	Units	Value	
		LO ₂	LCH ₄
Design injection temperatures, T_{inj}	[K]	90	112
Mass flow rates (full-thrust), \dot{m}_{max}	[kg/s]·10 ³	151.0	54.0
Mass flow rates (idle), \dot{m}_{min}	[kg/s]·10 ³	25.2	9.0
Maximum pressure drop, Δp_{max}	[MPa]	0.27	0.60
Minimum pressure drop, Δp_{min}	[MPa]	0.18	0.40
Assumed discharge coefficient, C_d	[-]	0.65	0.75

Values of discharge coefficient change with mass flow and thrust setting. However, it was preferable to accept a slight non-linearity rather than attempt to design the injector for variable flow coefficients. It was assumed that both discharge coefficients change in a similar manner, thus not affecting mixture ratio considerably.

Table 6.2.: Summary of LCH₄ Injector Design Calculations

Maximum flow area, A_{fmax} [mm ²]	3.19
Minimum flow area, A_{fmin} [mm ²]	0.78
Design injection velocity, V_f [m/s]	39.8

These calculations indicate very small fuel injection areas for reasonable fuel stream energy levels and low oxidizer injection pressures. Injector hydraulic and spray characteristics are presented in the Cold-Flow Characterization Section.

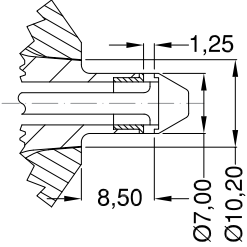
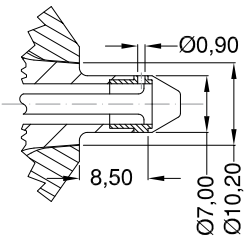
Injectors Configurations

Modifications to the basic injector design were made in the course of experimental tests to study the effects over pintle tip overheat and throat erosion. Table 6.4 shows both baseline versions with slotted and circular LO₂ orifices and the four most relevant alterations in design. These alterations incorporated individual or combined measures, such as: (1) reduction of the skip ratio from the baseline design value, (2) addition of a 25° ramp to deflect the outer propellant flow and (3) an actively cooled pintle tip. Numerous additional changes were attempted with less success and are not included in the present discussion.

Table 6.3.: Summary of LO₂ Injector Design Calculations

General	
Maximum flow area, $A_{o\max}$ [mm ²]	9.34
Minimum flow area, $A_{o\min}$ [mm ²]	2.28
Design injection velocity, V_o [m/s]	14.0
Pintle-to-chamber diameter ratio, [-]	7.15
Skip ratio (baseline), [-]	1.0
Number of primary orifices, [-]	12
Number of secondary orifices, [-]	0
Slotted Orifice	
Slot aspect ratio, [-]	2
Slot width, W [mm]	0.62
Slot height (full thrust), L_{\max} [mm]	1.24
Slot height (idle), L_{\min} [mm]	0.21
Blockage factor, BF [%]	34
Circular Orifice (full thrust setting only)	
Orifice diameter, d_o [mm]	0.90
Blockage factor, BF [%]	45

Table 6.4.: Pintle Injector Configurations Evaluated.

Injector Description	Schematic	Comment
1 Baseline design with rectangular LO ₂ orifices.		Employed rectangular orifices in the high-thrust mode.
2 Evaluation of circular LO ₂ orifices with the baseline skip distance.		Re-design and substitution of pintle tip material for a copper alloy.

6. Hardware Design and Description

Table 6.4.: Pintle Injector Configurations Evaluated. (continued)

Injector Description	Schematic	Comment
<p>3</p> <p>Reduction of the skip ratio to 0.55; employed rectangular LO₂ orifices.</p>		<p>Pintle body (needle) diameter reduced from 3.5 to 2.5 [mm]. New fabricated LO₂ sleeve made of brass.</p>
<p>4</p> <p>Same as Injector 3; incorporated active cooling of the pintle tip.</p>		<p>—</p>
<p>5</p> <p>Addition of a 25° ramp to the sleeve for displacement of the impingement point.</p>		<p>—</p>
<p>6</p> <p>Same as Injector 5 with inclusion of pintle tip cooling.</p>		<p>—</p>

6.1.4. Sensitivity Analysis

Having calculated nominal injector dimensions, the next task was to briefly evaluate the impact of geometric and hydraulic variability on TMR and engine mixture ratio and decide upon which manufacturing tolerances to adopt. This was made by partial differentiating Equation (6.13) with respect to the parameters of interest. If these deviations are small ($\pm 10\%$) Equations (6.14) and (6.15) can describe the corresponding sensitivity of individual parameter variation over the values of TMR and mixture ratio. The most critical dimension in the entire injector assembly is the register (alignment) between the oxidizer and fuel injector sleeves. The inside diameter D_{in} of the oxidizer sleeve must be held concentric to the bore of diameter D_{fm} of the fuel sleeve to ensure circumferential uniformity of the fuel sheet thickness. For the purposes of determining dimension tolerances, it was assumed that both propellant injection temperatures remain unchanged, and therefore the effect over propellant injection density can be neglected. With all other operating factors (pressure drops and discharge coefficients) at the design point, it is noted that the values of TMR and K_m are very sensitive to deviations in fuel film thickness. This led to the conclusion that, in order to prevent oxidizer streams of impacting the chamber walls, a larger tolerance over the fuel sleeve bore diameter is preferred.

$$\begin{aligned}
 \delta TMR &= 2(\delta C_{d_f} - \delta C_{d_o}) + \dots \\
 &= -(\delta W + \delta L) + \dots \\
 &= \frac{\pi}{2A_f} (\overline{D_{fm}^2} \delta D_{fm} - \overline{D_{in}^2} \delta D_{in}) + \dots \\
 &= -\delta \Delta p_o + \delta \Delta p_f.
 \end{aligned} \tag{6.14}$$

$$\begin{aligned}
 \delta K_m &= (\delta C_{d_f} - \delta C_{d_o}) + \dots \\
 &= (\delta W + \delta L) + \dots \\
 &= -\frac{\pi}{2A_f} (\overline{D_{fm}^2} \delta D_{fm} + \overline{D_{in}^2} \delta D_{in}) + \dots \\
 &= 0.5(\delta \rho_o - \delta \rho_f) + \dots \\
 &= 0.5(\delta \Delta p_o - \delta \Delta p_f).
 \end{aligned} \tag{6.15}$$

6.1.5. Injector Manufacturing and Assembly

The basic injector components are the main body, LCH_4 sleeve, LO_2 dome/sleeve, pintle tip and orifice ring. Injector components exposed to the combustion gas environment (i.e. the pintle tip and sleeve) were initially fabricated from AISI 321 (1.4541) stainless steel. Problems of excessive heating arose and led to erosion of these components and materials of higher thermal conductivity were incorporated, such as brass and copper.

Assembly of the injector is accomplished by inserting the pintle body and orifice ring into the LO_2 sleeve. The pintle is held into position by a mechanical interface between the LO_2 flow trimming orifices upstream of the injection point and the sleeve inside diameter.

6. Hardware Design and Description

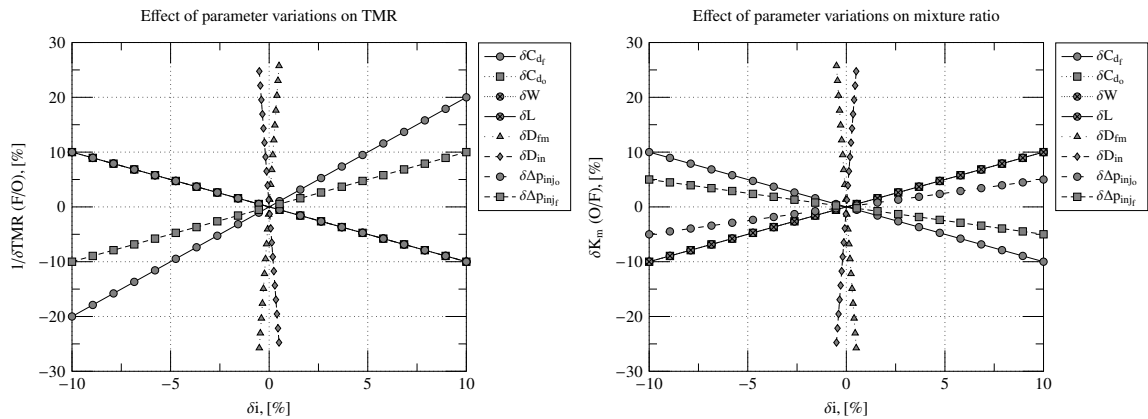


Figure 6.3.: Sensitivity of design parameters on mixture ratio and TMR.

The LO₂ sleeve and pintle tip sub-assembly is then inserted into the injector main body, observing the proper set of spacers and alignment to obtain the intended fuel gap setting. The LCH₄ sleeve is bolted up to the main body and may, in addition to spacer setting, be adjusted to suit the desired fuel sheet thickness. The injector as a unit is finally bolted to the engine faceplate. This type of installation provided a very convenient way of performing rapid changes to the injector during development tests.

6.1.6. Instrumentation

Measurement taps were provided on both oxidizer and fuel ports for measuring injection pressures and temperatures. Early versions of the pintle had a thermocouple in contact with the pintle tip, close to the point of LO₂ injection. As mentioned before, damage to these instrumented tips due to erosion, unfortunately prevented further evaluation of soak distances and temperatures in that particular region.

6.2. Experimental Thrust Chamber Design

6.2.1. General

The experimental thrust chamber was a copper heat sink design, sized to give nominal run durations of 4 to 6 seconds. The chamber was designed as a flexible piece of hardware being made of 50-[mm] inner diameter segments and throat sections. With this design, the chamber characteristic length L^* or contraction ratio could be changed by changing the segment or throat section accordingly. A nominal contraction ratio of about 9 was selected for the basic injector development tests. The L^* for this test series was 1.50 [m] and consisted of one throat section and three segments. The nozzle expansion was also truncated for test site ambient pressure. Figure 6.4 is the three-dimensional representation of this particular chamber configuration.

The chamber was attached to the injector faceplate by a bolt-on or flange design that allowed rapid exchange of nozzle type and/or segment lengths without necessity of dismantling the complete chamber assembly.

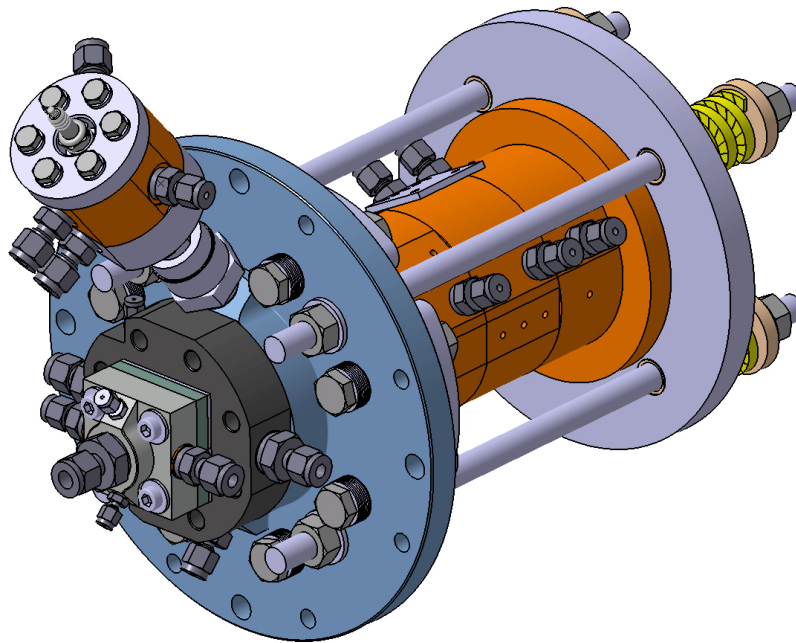


Figure 6.4.: Chamber assembly.

Subsequent tests made use of a shorter chamber length resulting in the same L^* of 1.50 [m], with use of the design chamber contraction ratio of 13. A nozzle expansion ratio of 4 blended to the convergent section was selected for these tests to improve outlet flow conditions.

Ignition system

In the present investigation a torch and a resonance igniter were initially considered. However, for reasons of simplicity and reliability, a conventional torch igniter was conceived, designed and built. Nominal igniter parameters were a chamber pressure of 0.35 [MPa] and a mixture ratio of 2.5. Igniter operating times varied slightly throughout the tests. An average 0.600 [ms] operating time proved sufficient for the majority of main engine mixture ratios investigated.

Chamber Wall Sizing

The minimum chamber wall thickness was sized for stress limits, accounting for a given maximum run time. Although copper is a common material for these applications, it has drastically different heat conductivity when compared to thermocouple probe materials. For this reason, a comparison of the transient heat flux capabilities of copper, nickel and steel was briefly made. The basis for comparison assumed that all materials reached their maximum temperatures in about 6 [s], a time which should be large compared to any buildup time of the gas-side temperature and heat transfer coefficient. It was additionally

6. Hardware Design and Description

assumed that the 6-[s] interval corresponds to a Fourier number of 1.60 for a flat plate with an initial temperature of 288 [K]. The definition of the Fourier Number can be rearranged to give the plate thickness as:

$$L = \left[\frac{\alpha t}{F_o} \right]^{\frac{1}{2}}. \quad (6.16)$$

where:

- L = thickness of flat plate, [m];
- α = thermal diffusivity of plate material, [m²/s];
- t = time, [s];
- F_o = Fourier Number, [-].

The temperature ratio at the heated surface of the plate at $F_o = 1.60$ is assessed as

$$\left(\frac{T_{wg(max)} - T_0}{T_g - T_0} \right). \quad (6.17)$$

using the allowable maximum temperature for the material and the assumed gas temperature, the Biot Number corresponding to this temperature ratio at $F_o = 1.60$ is determined by interpolation on Figure 6.5. From the Biot Number and from the thickness and thermal conductivity of the plate, the gas heat transfer coefficient is determined, and then the surface heat transfer rate is calculated. The comparison summarized in Table 6.5 shows that copper can absorb as much as twice the heat flux of nickel without overheating the inner chamber wall and is quite superior to stainless steel. Copper has much less variation of thermal properties and for this reason it became the preferred material of construction; nevertheless, a short nickel segment was manufactured for the effect of comparing thermocouple response in the first test firing series.

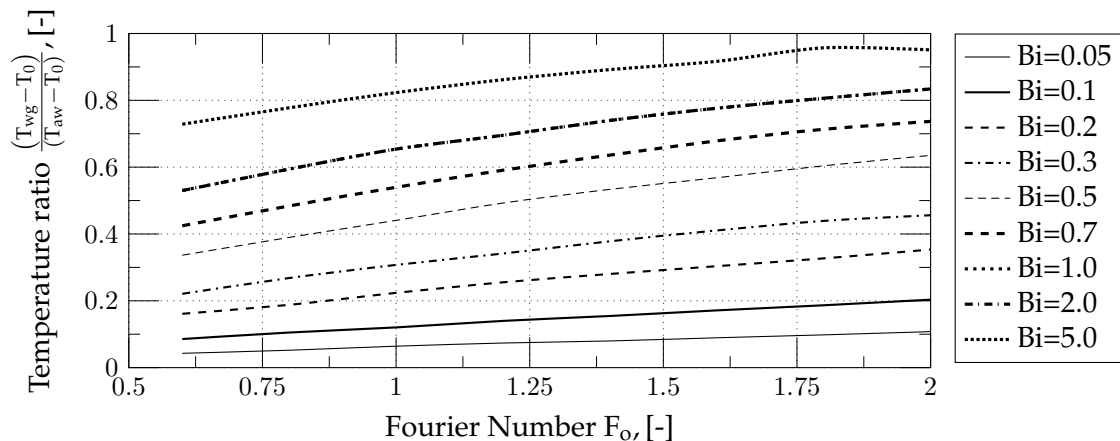


Figure 6.5.: Temperature ratio as a function of Fourier and Biot Numbers.

Table 6.5.: Comparative of transient heat flux capability for steel, copper and nickel chamber wall materials.

Material		Plate thickness	Adiabatic wall temperature	Temperature ratio	Biot Number	Heat transfer coefficient	$(T_{aw} - T_{wg})$	Maximum allowable heat flux
		L	T_{aw}	$\frac{(T_{wg}-T_0)}{(T_{aw}-T_0)}$	Bi	h_G		\dot{q}_g
		[mm]	[K]	[-]	[-]	$[\frac{W}{m^2 \cdot K}]$	[K]	$[\frac{MW}{m^2 \cdot K}]$
Steel (1.4541)		5.8	1368	0.587	0.531	1501.6	446	0.670
T_{wg} (max) [K]	922		3035	0.231	0.144	407.1	2113	0.860
k [W/m·K]	16.5							
α [cm ² /s]	0.0838							
Copper (CuCr1Zr)		20.2	1300	0.517	0.397	7293.7	489	3.567
T_{wg} (max) [K]	811		1900	0.324	0.217	3977.8	1089	4.332
k [W/m·K]	370		2500	0.236	0.148	2719.2	1689	4.593
α [cm ² /s]	1.00		3035	0.190	0.114	2093.3	2224	4.655
Nickel (2.4068)		8.9	1300	0.704	0.782	6956.1	300	2.087
T_{wg} (max) [K]	1000		3035	0.259	0.165	1466.8	2035	2.985
k [W/m·K]	79.3							
α [cm ² /s]	0.196							

For the nominal firings, a thermal penetration distance of approximately 20 [mm] was expected, which means that the outside copper surface temperature would barely change from ambient temperature conditions for firing durations much lower than 6 [s]. Taking a safety factor of 2, the stress level was more than adequate for CuCr1Zr and Nickel alloys. Furthermore, this wall thickness was also adequate for all instrumentation requirements.

6.2.2. Instrumentation

The chamber was instrumented for static pressure measurements as well as thermal measurements. Two pressure tap ports were provided at the start of the convergence and at the injector end. One pressure tap was mounted into the faceplate, upstream of the injection point. This signal was usually not regarded for performance calculations because of the intense recirculation zones created by the spray fan. Thermocouples distributed axially and circumferentially to obtain the required wall heat flux data were embedded in the segment walls. Surface temperatures during firing, were monitored with iron/constantan thermocouples. These were of the bare wire type with stripped leads for faster response. Inner-wall, transient temperature data, used 0.5 [mm]-diameter probe chromel/alumel thermocouples. These thermocouples were pressed through springs against the bottom of the mounting holes with an average force of ca. 3.5 [N], ensuring proper contact of the thermocouple sensing tip with the chamber inner-wall at all times.

Part V.

Experimental Results

7. Experimental Results

Upon completion of the analytical studies, hardware design and manufacturing, the experimental investigation of the proposed injector design was initiated. This effort consisted of basic cold-flow studies and hot firing runs, which culminated with an injector configuration that provided nearly 85% of the theoretical equilibrium C^* at the design mixture ratio.

7.1. Injector Cold-Flow Studies

Cold flow studies had a dual purpose: firstly to obtain the basic injector hydraulic characteristics in terms of pressure drop, mass flow and secondly to evaluate the spray pattern through visual observations. An additional objective was to utilize a mechanical patternator to assess injector mixture ratio and mass distribution. A picture of this test stand and the mechanical patternator built are shown in Figure 7.1.

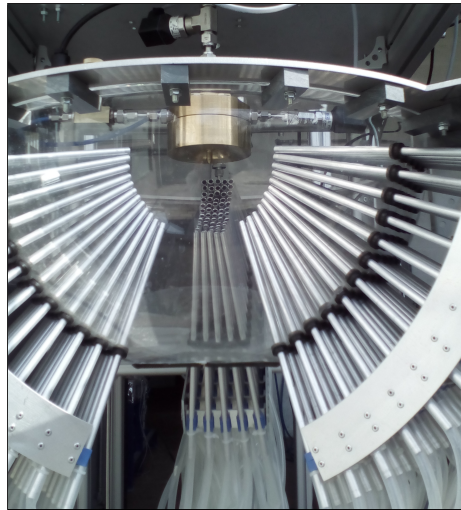
7.1.1. Hydraulic Characteristics

The flow rate-pressure drop characteristics were determined using water, with results appearing in Figures 7.3 for the fuel flow and Figures 7.2 for the oxidizer flow. Pressure losses in the propellant flow paths were accounted for in the computation of these curves. As is noted, the values of C_d obtained with water differed considerably with respect to the assumed designed values. The reason for that lies probably in the small injector dimensions and unique geometries which cannot be treated as in equivalent orifice flow conditions. Because of this discrepancy and the small injection pressure drops at the low flow regime, only the high thrust setting of the injector was considered for subsequent hot-firings.

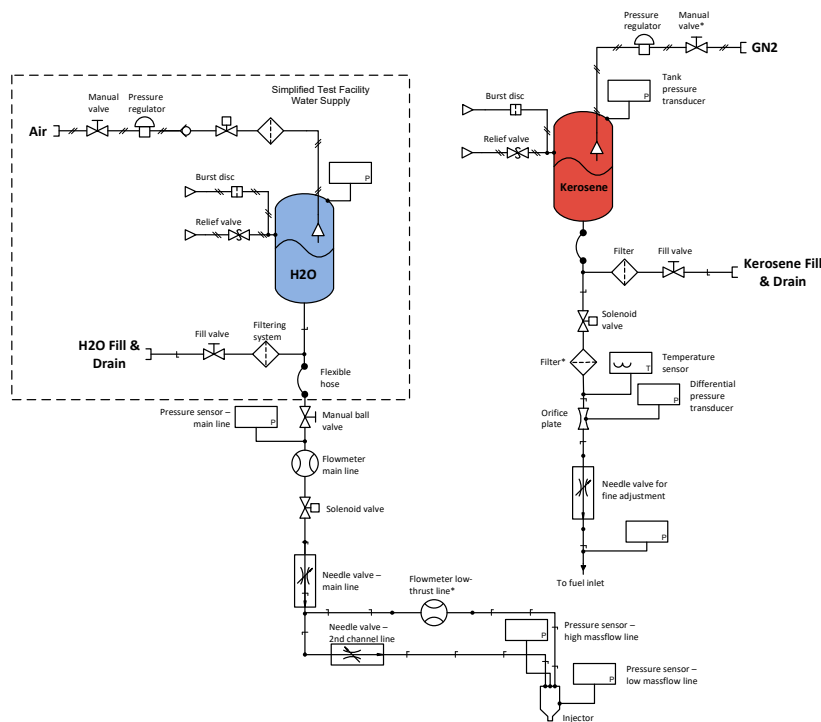
Figure 7.4 presents the aspect of the spray for Injector 1, the baseline version. The characteristic convergent annular LCH_4 flow is depicted in Figure 7.6a. Uniform flow conditions through the fuel gap are achieved primarily by use of flow straighteners and by careful centering of the LO_2 sleeve. Figure 7.6b illustrates the combined LO_2 and LCH_4 sprays at optimum momenta. Adjusting the momentum ratio with water to reflect real propellant conditions require conversion of simulant water flows into propellant flow as described by Sutton and Biblarz [113]. Spray angles were measured from the pictures to within $\pm 1.5^\circ$ and after numerous tests, the data have being compiled in Tables 7.1 and 7.2.

Injector 2 differed from Injector 1 in that it possessed a slightly larger (wider) LO_2 spray angle and more reproducible flow characteristics. Figure 7.5 shows a cold-flow check of Injector 4, including the four 0.5-[mm] orifices in the pintle tip. These orifices should meter the LO_2 cooling flow to approximately 10% of the total oxidizer mass flow rate. For the same LO_2 slotted orifice flow area, the presence of the axial orifices imparted a slight loss

7. Experimental Results



(a) View of test stand.



(b) Hydraulic scheme of the cold-flow test stand.

Figure 7.1.: Cold-flow test stand.

in flow radial velocity and a corresponding decrease in spray angle. It was hoped that this arrangement would displace the combustion zone away from the pintle tip and lower temperatures in that region.

Injectors 5 and 6 included a ramp that deflected the LCH_4 stream, while approximately retaining the baseline skip ratio. Figure 7.6 shows the fundamental differences in fuel

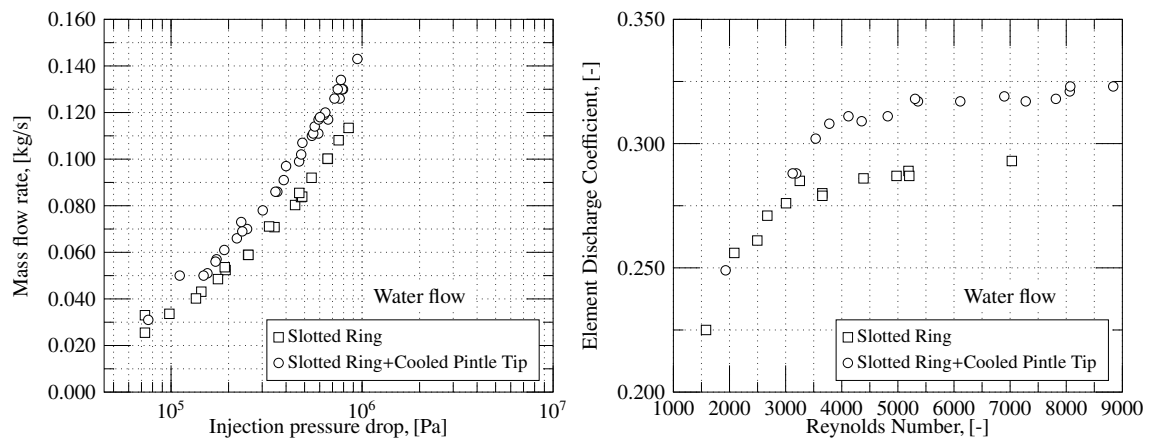


Figure 7.2.: Oxidizer Slotted-Orifice Hydraulic Characteristics.

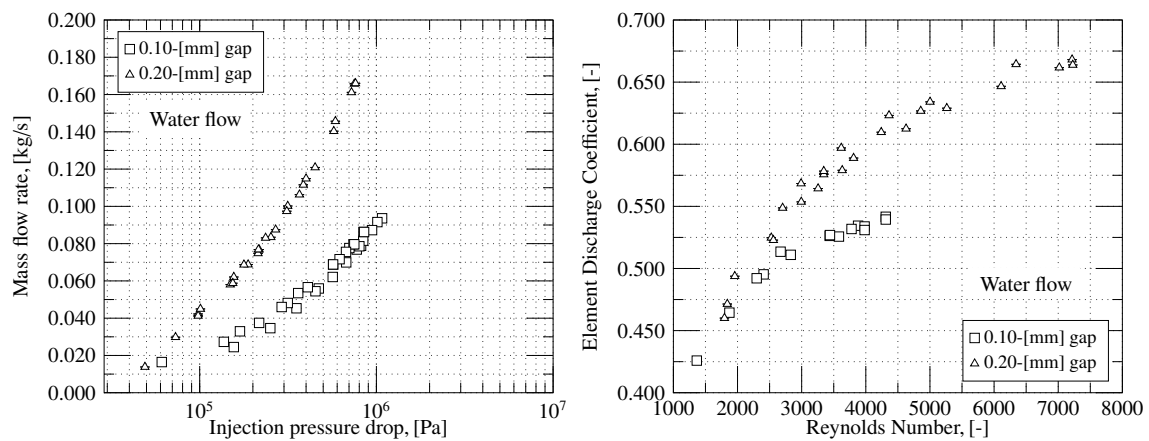


Figure 7.3.: Fuel Gap Hydraulic Characteristics.

Table 7.1.: Typical Values for the Discharge Coefficient (Nominal Regime).

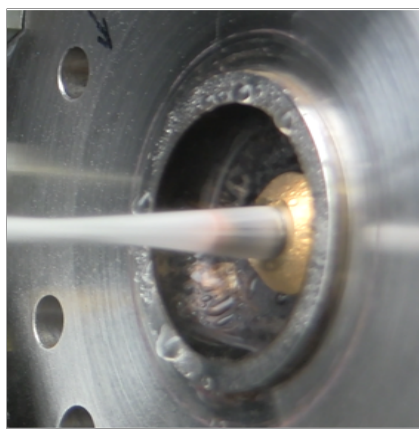
Injector #	Discharge Coefficient, $C_{d_{inj}}$		
	LO ₂	LO ₂ +Cooling	Uncertainty (%)
1,3-6	0.296	0.335	±13
2	0.383	-	±13
Injector #	LCH ₄ (1-[mm] Shim)	LCH ₄ (2-[mm] Shim)	Uncertainty (%)
1-6	0.533	0.632	±13

flow pattern. In the baseline design, the pintle tip is enveloped by the convergent fuel stream; with the deflector, the tip can be clearly seen. The ramp was intended to remove the combustion zone from the center of the chamber and constituted another strategy to overcome pintle tip overheating and throat erosion. The ramp had a 25° half-deflection angle

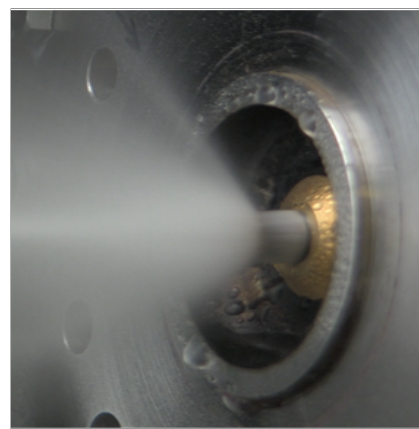
7. Experimental Results

Table 7.2.: Approximate Spray Angles $2\bar{\alpha}$.

Injector #	Spray Angle, $2\bar{\alpha}$, [degrees]		Uncertainty (%)
	LO ₂	LO ₂ +Cooling	
1,3-6	170°	149°	±1.5
2	174°	-	±1.5
Injector #	LCH ₄ (1-[mm] Shim)		Uncertainty (%)
1-4	-9°		±1.5
5,6	61°		±1.5



(a) LCH₄ flow.



(b) Both flows at optimum momenta.

Figure 7.4.: Spray patterns for Injector 1.

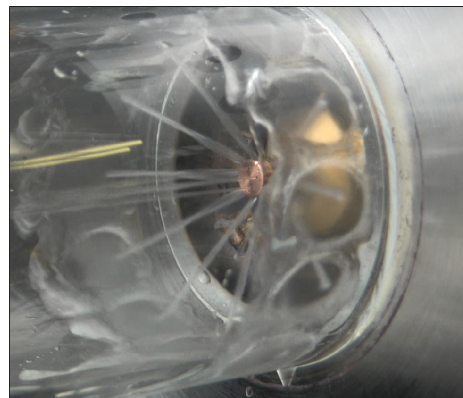


Figure 7.5.: Cold-flow evaluation of Injector 4, showing cooling and primary radial flows.

and introduced a decelerating effect over the annular fuel flow, resulting in a minor loss in momentum. However, this effect was considered negligible and no correction in the fuel flow gap or LO₂ orifice flow area was made. Injector 6 combined the ramp solution and the active cooling of the pintle tip. Figures 7.7 show the corresponding fuel, oxidizer and com-

bined flows. The introduction of tip cooling for Injector 6 was actually not necessary from the standpoint of material durability as would be proven by subsequent hot-firing tests. As seen in Figure 7.7b, the axial cooling flow offers very little opportunity for propellant interaction downstream of the tip. The decay in performance seems to be, in principle, not apparent, as discussed later in Section 7.2.3.

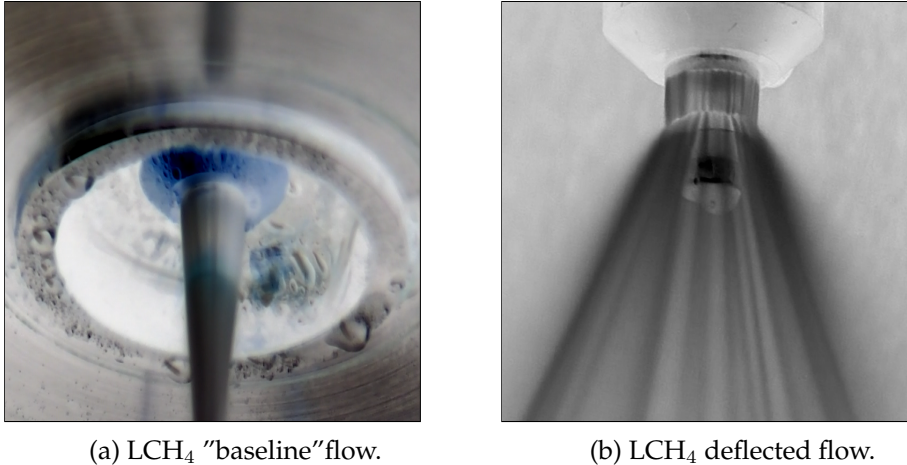


Figure 7.6.: Fundamental visual differences between both LCH₄ flows.

7.1.2. Use of the Mechanical Patternator Technique

The use of mechanical patternators to investigate injector mass and mixture ratio distribution is an old, but useful technique for preliminary screening of injector candidates [79]. The apparatus of Figure 7.6a collects flow from the conical fan of the injector within a range of 0 to 90 degrees and for three circumferential locations spaced 120°. In total, 180 collecting tubes were present, from which manual volume readings are made. Mixture ratio is measured by flowing water and kerosene through the oxidizer and fuel injection gaps, respectively. After collection, both fluids are allowed to separate, thus giving an indication of mass and mixture ratio circumferential, axial and radial distributions. These indications can be used to determine the effects of any non-uniformities on the expected combustion efficiency. The collected cold flow simulants with equal momentum ratios are converted to actual propellants through Equation (7.1):

$$K_m = K_m^* \left[\left(\frac{\rho_o}{\rho_f} \right)_{\text{Propellant}} \left(\frac{\rho_f}{\rho_o} \right)_{\text{Simulants}} \right]^{\frac{1}{2}}. \quad (7.1)$$

where:

- K_m = equivalent mixture ratio, [-];
- K_m^* = mixture ratio of simulants, [-];
- ρ = fluid density, [kg/m³].

The successful use of the apparatus was somewhat limited, due to the small tank volume

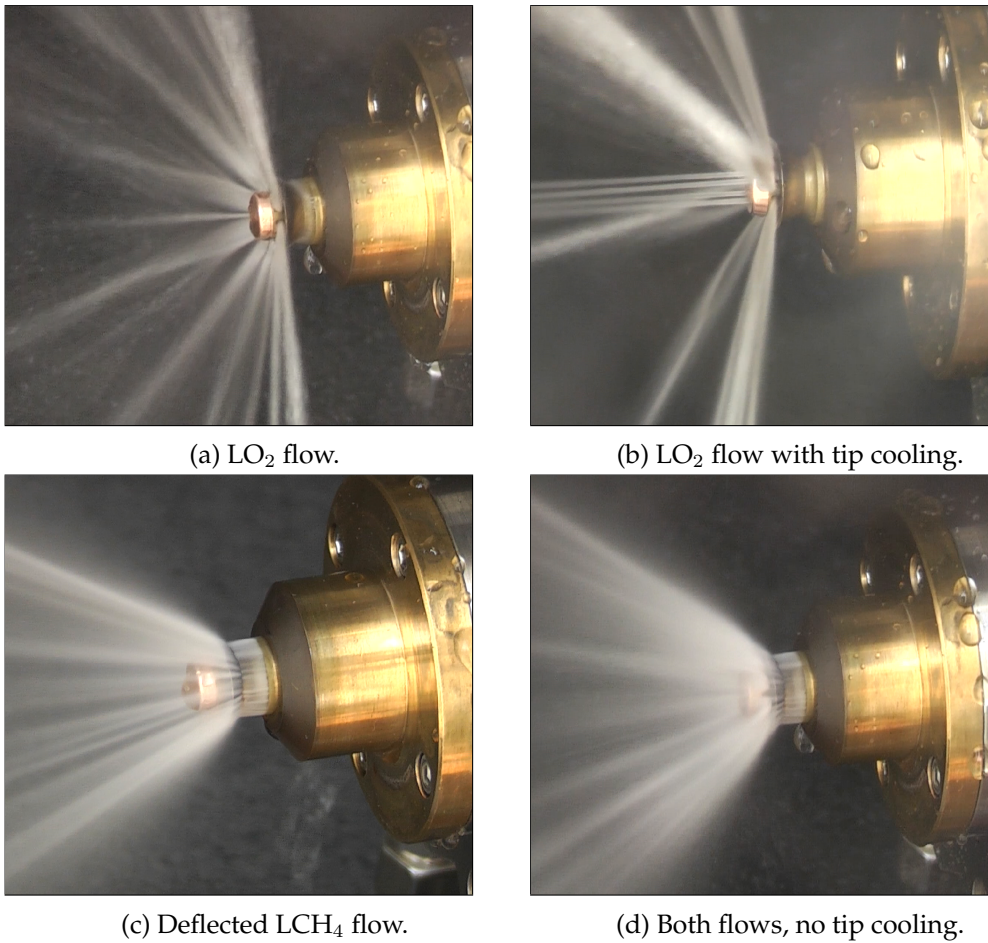


Figure 7.7.: Water flow-checks with Injectors 5 and 6, with deflected LCH₄ flow and two different LO₂ patterns.

available for kerosene. This led the data to reproduce very poorly. To remain within research schedule limitations, use of the patternator technique to investigate injector flow uniformity was therefore discontinued.

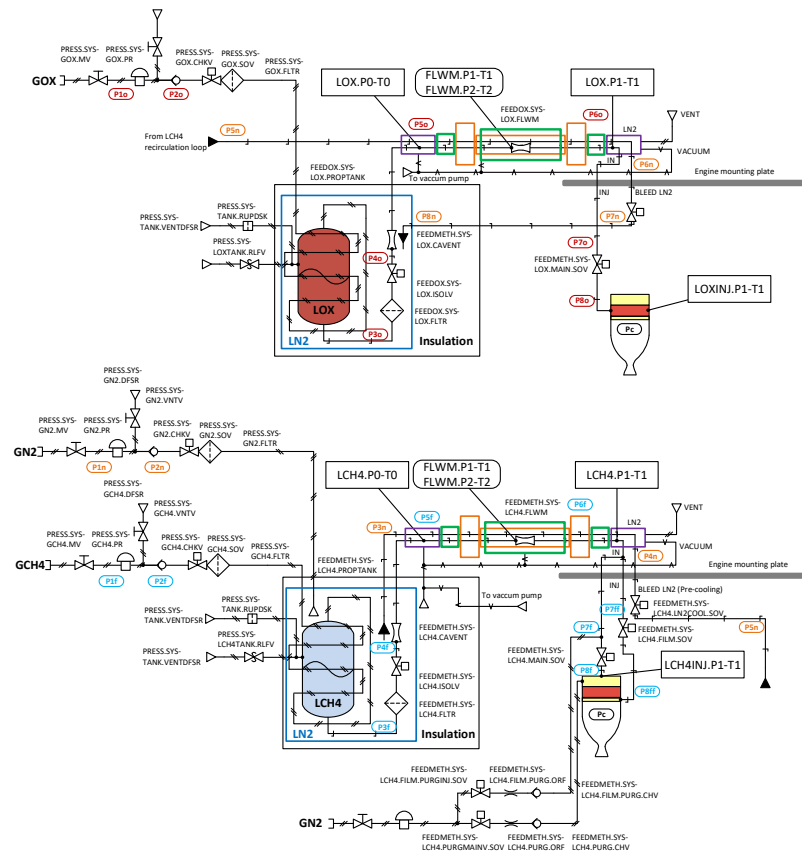
7.2. Injector Hot-Fire Characterization

7.2.1. Experimental Facility

All hot-firing test activities were conducted at the rocket test facility of the Institute of Space Propulsion in Garching. A schematic and an overall view of the cryogenic test stand designed and built for that purpose is shown in Figures 7.8 and 7.9, respectively.

Test Stand

A detailed description of test stand subsystems, instrumentation and test operational procedures is presented by Vasques and Haidn [114]. Due to laboratory space limitations,

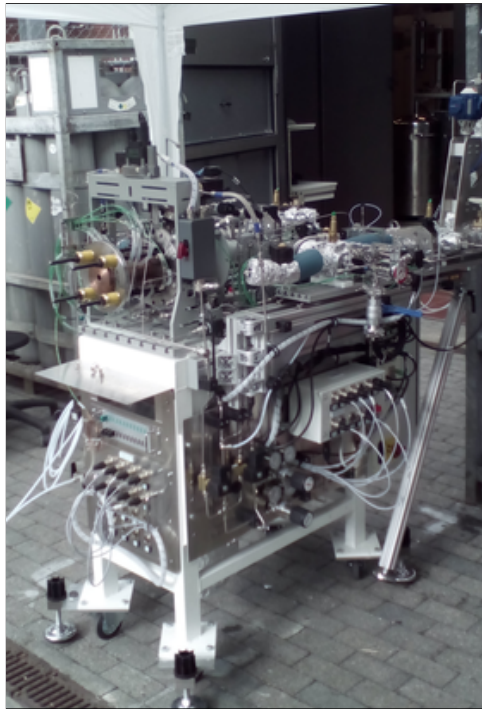
Figure 7.8.: Schematic of LO₂/LCH₄ facility.

the test stand was conceived as a movable and flexible unit. Each propellant feed-system is mounted on a fold-out table that can be directly aligned to the injection head connection points. The various test stand systems are briefly discussed in the following sections.

Liquid Methane Supply System

Production of liquid methane took place prior to testing and employed a pressurized liquid nitrogen bath at 0.65 [MPa] to keep methane temperatures within the liquid range. A regulated supply of gaseous methane flowed through a stainless steel tubing coil built around a 3-liter cylindrical storage tank immersed in the liquid nitrogen bath. This tank was pressurized to a level of 0.2 [MPa] for propellant transfer operations. The actual outlet temperature of liquid methane was around 120 [K]. A second, 3-liter "run tank", was used for supplying sufficient liquid methane for the firing. Modifications to the test setup to improve flow conditions included production and temperature conditioning of LCH₄ in the liquefier. This was then made to circulate through the lines and venturi meter in a series of isolation and bypass valves, before reaching the run tank prior to a test firing. A liquid nitrogen refrigerant flow supplied by a 100-liter dewar was maintained throughout the test for cool-down operations. Propellant lines upstream and downstream of the instrumen-

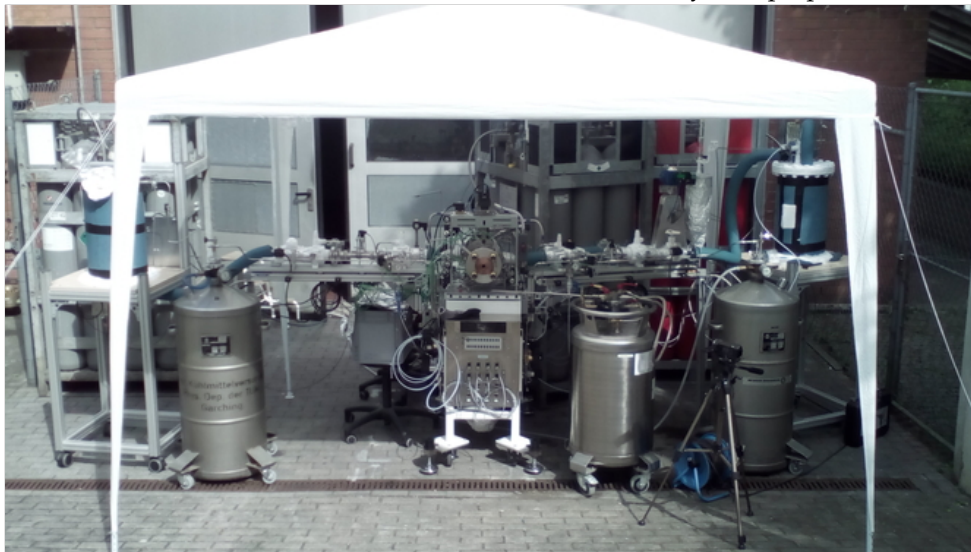
7. Experimental Results



(a) Test stand roll-out.



(b) Feed-system preparation.



(c) Typical test setup.

Figure 7.9.: Overall view of the miniature cryogenic test stand.

tation unit were simply foam insulated. This was especially important in order to reduce line stiffness and attenuate thrust cell side-loading effects. The line segment containing the venturi meter was vacuum insulated. Thermal control of the methane line proved difficult due to the low mass flows involved and the high heat input from ambient. The LN_2 refrigerant flow rate was then adjusted in subsequent tests to result in methane temper-

atures upstream of the venturi meter as low as 120 [K]. In general, the overall methane flow system was broken down into a number of parallel flow circuits, rather than flowing all sections in a single series arrangement. A bypass of flow (bleed) was provided that tapped-off the LCH_4 propellant supply system. The bypass control valve was automatically sequenced off just prior to the actuation of the main fuel valve. Pressurization of the run tank was made directly by gaseous methane by switching the corresponding pressurizing valve. An electro-pneumatically driven valve isolated all the flow system from the engine in the event of a sequence failure. Gas supply to this valve and to all fuel line purge operations was made with a dedicated gaseous nitrogen provision.

Liquid Oxygen Supply System

Liquid oxygen was produced on-site by direct liquefaction of gaseous oxygen flowing through a coil immersed in a liquid nitrogen bath. The coil was made out of stainless steel tubing spun around a 3-liter capacity tank. This tank was completely immersed in the liquid nitrogen bath and stored the liquefied oxygen produced for the firing. It was possible, by selective actuation of isolation valves, to flow LN_2 through both the LO_2 supply system and the line jackets for preliminary system cool-down or temperature control. The liquid oxygen supply system from the tank to the main valve was a vacuum-insulated, LN_2 -jacketed line. As in the case of the LCH_4 system, a liquid nitrogen refrigerant flow was maintained through the jacket passages in the instrumentation unit and a final run of approximately 30 [cm] line leading to the engine was unjacketed. This segment was simply foam-insulated during chill-down. This was adopted for simplicity and to increase thrust measurement accuracy. The LN_2 refrigerant flow rate was controlled by varying the dewar supply pressure, allowing delivery of liquid oxygen to the LO_2 venturi meter at temperatures as low as 85 [K]. A bypass flow system was provided which tapped off the LO_2 propellant supply system immediately downstream of the venturi meter. The bypass control valve maintained a continuous flow through that portion of the system until just prior to actuation of the engine main oxidizer valves. The bypass valve shut-off and opening of the oxidizer main valve were controlled by the PLC controller. A dedicated gaseous nitrogen system was used for all line purges. The oxidizer tank pressurization was provided by the gaseous oxygen entering the liquefier, through actuation of pressurizing valves.

Igniter Supply System

Regulated supplies of GO_2 and GCH_4 ran through stainless steel tubing mounted along each folding table and were connected via flexible hoses to the respective igniter valves. Correct igniter mixture ratio was achieved by metering both flows through sonic orifices mounted downstream of each valve. Spark energy was provided by a 10-kV electric spark coil generator. A regulated supply of GN_2 was used for igniter purge and cleaning procedures during checkout operations.

Chamber Installation Details

Details of the chamber installation may be seen in Fig. 7.10. The thrust absorbing structure was a frame made of 10-[mm] thick steel plates welded together. This structure pro-

7. Experimental Results

vided enough seismic mass and damping. Two steel flexures, located 90 degrees apart, were used to permit axial motion of the engine, while supporting the weight of the hardware and absorbing side loads. The engine was bolted to a thrust mount that threaded into the body of the load cell. This mount had a conical shape that was partially opened to provide access to the thrust calibration fixture. The fixture consisted of a ball-bearing mounted, right-angled lever system which allowed weights to be hung on the horizontal arm.

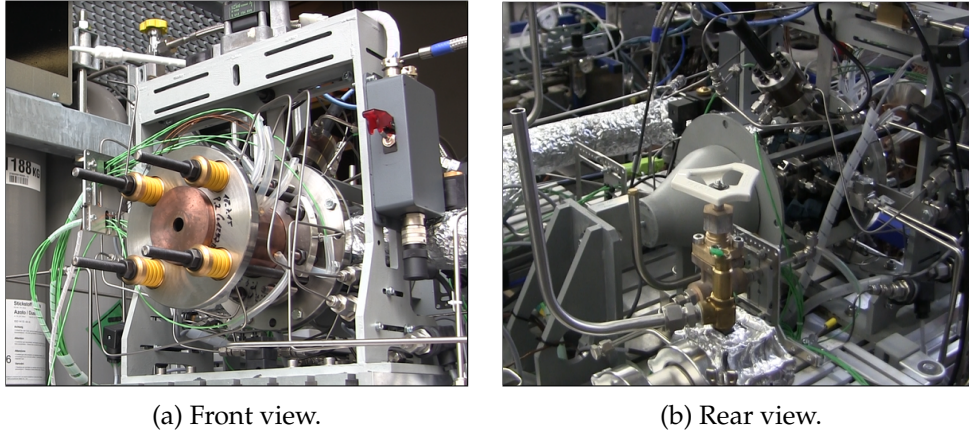


Figure 7.10.: Chamber installation with provisions for pressure, temperature and force measurements.

Instrumentation and Controls

The pressure transducers used were mainly thin-film strain gage instruments and where oxygen compatibility and superior corrosion resistance was required, ceramic strain gage transducers were adopted. The load-cell used for thrust measurements was a bonded strain-type transducer with a 1000 [N] rating. This load-cell was selected to provide a high-stiffness and, thus, to result in a short thrust measurement response. The cryogenic range temperature measurements were made with copper/constantan (propellant tanks) and chromel/alumel (feed-system) thermocouples by use of feed-throughs or standard connectors. The propellant flowrates were measured using subcritical venturi meters specially designed for this purpose. A three-wall stainless-steel construction was conceived to permit a continuous flow of LN_2 through the inner annular passage, while a vacuum was maintained in the outer annulus for superior thermal insulation. Upstream and downstream of the venturi meters, two mounting blocks were attached. These fully instrumented blocks served as a manifold for the LN_2 refrigerant flow and provided interface to all bypass, relief, isolation and main engine valves. Valve actuation as well as chamber start- and shut-down logics were implemented in conjunction with a Programmable Logic Controller (PLC). Manual and automatic actuation modes could be executed by selecting the appropriate switch position. A manual abort switch that could override any previous logic inputs was available to the operator. Any firing could also be automatically aborted by any of the redline input signals. The majority of the firings were additionally recorded

in video so that it was possible to visually assess ignition behaviour and the aspect of exhaust flame after the firing. Dedicated card modules were used for data acquisition at 160 [ksamples/s] and 14 bit resolution.

Test Procedures

Initial operations performed, prior to initiation of system chill-down, involved long purges with gaseous nitrogen. This eliminated the possibility of the presence of condensable gases in any part of the flow systems. Periodically, the line systems were leak checked with pressurized nitrogen and the main propellant valves and system bypass valves were checked for seat and/or stem leakage. In addition, periodic leak checks of the systems also were performed at cryogenic conditions; for these checks, liquid nitrogen was flowed through the systems. Combustion chamber, igniter and injection head leak tests were made with gaseous nitrogen using a special fixture attached to the threaded rods that closed the exhaust area of the chamber. After completion of the above operations, the vacuum environment for the propellant line insulation was created. Intermittent nitrogen purges of the chamber were made through trickle purges and main engine valves. This procedure aimed at eliminating any water that might have accumulated in the injection head, resulting from condensation and freezing of combustion-generated water during igniter checkout or previous shutdown sequence. Chill-down of the propellant supply was always done after all purge operations were terminated. The cryogenic propellant flows were then initiated in the various line jackets; liquid methane was allowed to flow through the bypass system and liquid nitrogen was flowed into the engine via the oxidizer supply lines. After all hardware was conditioned to the desired temperature range, some LCH_4 and LO_2 were permitted to separately flow through the main propellant valves and into the injection head. When the venturi upstream temperature sensors indicated that the propellant temperatures were in the desired range, the firings were initiated by arming the ignition circuit and engaging the automatic sequencer. Many firing sequence logics were attempted; here follows a description of a normal sequence adopted for the majority of the tests. The firing sequence maintained propellant flows through their respective venturi meters until approximately 2 [s] before the firing, by means of the propellant bypass systems. These flows were shutoff automatically, and the igniter system was activated. The spark was initiated about 100 [msec] before main engine propellant valve actuation and was maintained for 100 [msec] afterwards. The valve actuation logic circuits opened the main propellant valves with an average relative fuel lag of about 250 [msec]. The firings were performed with a continuous monitoring of five parameters, using the PLC logic to abort the test if the redline values were exceeded. One thermocouple installed upstream of the nozzle throat was set to avoid continuous operation if the temperature encountered could potentially lead to chamber damage. Operator monitoring of the chamber pressure recording and camera monitoring resulted in manual run aborts if ignition did not occur or if an abnormal heat pattern was noted. The shutdown of the firing was always programmed to result in at least 50 [msec] of fuel valve lead. After conclusion of the firing, a check of all transducer readings was made. These data were used to determine whether any bias existed between the venturi upstream and venturi throat pressure measurement under the pressurized, non-flow conditions. The venturi differential pressures computed during run conditions were corrected to eliminate any noted bias effects. Additionally,

7. Experimental Results

these venturi transducer pressure measurements could also be compared to both mounting block transducer readings to discern whether any pressure measurement anomalies existed.

Run Duration

To ensure good performance data with the cryogenic test stand, it is important to have firing durations sufficiently long so that operational parameters (flow rate, propellant injection temperatures, thrust, propellant pressures, chamber pressure, etc.) have stabilized for a period of time to show steady-state behavior. This period of time, based on experience was at least 2.5 seconds.

7.2.2. Basic Pintle Injector Development

The initial effort of the hot-firing experimental tests was concentrated around two objectives: 1) verify ignition characteristics and 2) assess baseline injector designs 1 and 2 for durability and performance. Initial tests were conducted with the slotted ring orifice geometry and a nominal 0.10-[mm] fuel propellant gap, based upon initial cold-flow tests. Follow-up tests maintained the fuel injection velocities of the previous runs but were conducted with the circular orifice geometry for the oxidizer injector. Both oxidizer geometries and fuel flow injection gap were set for high-thrust mode operation which permitted the venturi meters to operate within an adequate range of Reynolds numbers. As already mentioned, all of the basic injector development tests were conducted using a chamber length of about 180 [mm], resulting in a L^* of 1.50 [m] with a contraction ratio of 9 and a truncated nozzle. This chamber characteristic length should provide, together with the high contraction ratio, sufficient residence time for complete combustion of propellants. In these baseline tests, fifteen thermocouples were used to monitor the chamber temperature distributions as shown in Figure 7.11.

7. Experimental Results

Early in the test campaign, difficulties arose with respect to the operation of the test stand. These difficulties were all primarily associated with system chill-down procedures and insulation, as well as with limited propellant supply for assessing the correct pressure schedules.

Test Summary

In total, forty tests were conducted: 23 with the slotted ring and 17 with the LO₂ circular orifice configuration. The envelope of chamber pressure and mixture ratios for the first phase of experiments is depicted by Figure 7.12.

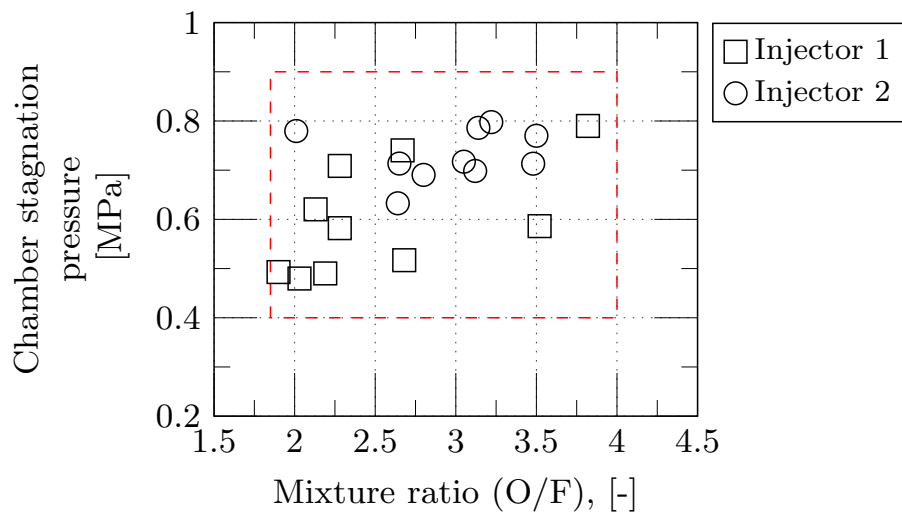


Figure 7.12.: Chamber pressure and mixture ratio operating envelope.

Temperature injection conditions observed for LO₂ fell mostly within a band between 105 to 115 [K] for both orifice shapes. Methane temperatures possessed a large spread in the initial tests, averaging nearly 195 [K]; this average would move up to 220 [K] with Injector 2, as injection pressures were slightly higher in these tests.

Even though propellant sub-cooled conditions upstream of both venturi meters existed, methane flow temperatures near the injection head could be only marginally controlled. This is due to the following reasons:

1. The low fuel mass flow rates associated with the low chamber pressures, which were unable to maintain injector body at the proper temperature;
2. The rather massive LCH₄ injector manifold could not be entirely cooled to permit design temperature conditions to be reached.

More importantly, and as mentioned in Section 7.2.1, the test stand was equipped with only a 3-liter fuel tank which limited the amount of fuel available for the test. Only one 3-liter pressure vessel of fuel could be installed in the methane liquefier since two bottles

would exceed its internal volume capacity. The use of this setup is not recommended because of the tendency of the methane gases to stratify while liquefying the gases and transferring them to the run tank. As a result, the capabilities of the test stand were limited in these early runs. In fact, methane injection pressures and temperatures reveal only near-saturated, or rather single-phase gaseous injection, as shown in Figure 7.13. On the other hand, according to Figure 7.14, liquid oxygen injection conditions are identified as saturated or sub-cooled. This is due to the fact that oxygen temperatures could be more easily controlled by permanently re-filling the LO₂ liquefier. Besides, in order to achieve proper conditioning of the run lines, it was necessary to bleed both oxidizer and fuel through the piping to prevent propellant boiling during the test. Because the system was limited in the fuel capacity, it was not possible to sufficiently cool down the feed lines prior to firing. However, this was not completely known until several tests had been conducted, and an analysis was made of the results.

Table 7.3 gives a summary of all valid data points considered during this initial evaluation phase. This table is a combination of the test results and does not include any performance corrections. The numbers are measured values taken as averages for the entire test run.

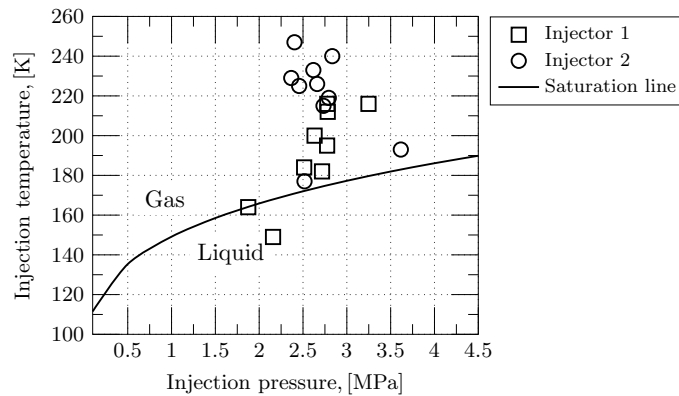


Figure 7.13.: LCH₄ propellant injection conditions.

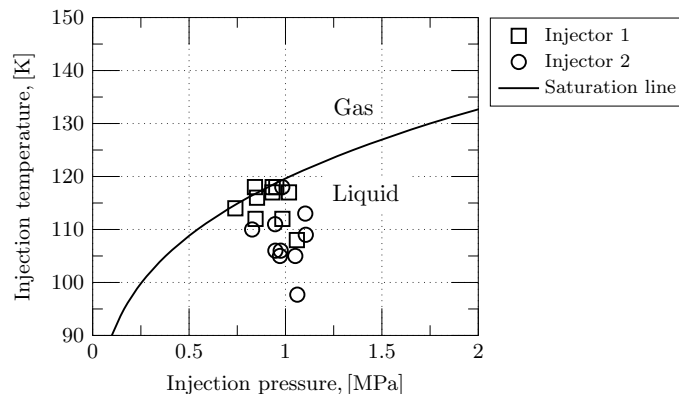


Figure 7.14.: LO₂ propellant injection conditions.

Table 7.3.: Phase I - Summary of Results.

Run #	Injection Element	Average measured values											Thrust, P [N]	$C_{exp_F}^*$ [m/s]	$\eta_{C_F}^*$ [-]	\dot{Q}_{Total} [MW]	\dot{Q}_{Nozzle} [MW]	Run Duration [s]	Comment
		O/F Overall [-]	O/F Core [-]	\dot{m}_T [kg/s]	\dot{m}_{LO_2} [kg/s]	\dot{m}_{LCH_4} [kg/s]	$(P_k)_o$ [MPa]	ΔP_{LO_2} [MPa]	ΔP_{LCH_4} [MPa]	C_{theo}^* [m/s]	$C_{exp_P}^*$ [m/s]	$\eta_{C_P}^*$ [-]							
001	Slotted ring	2.28		0.091	0.063	0.028	0.71	0.14	1.45	1849.10	1646.04	0.89	No thrust information				3.50	LO ₂ main valve shut-off lag	
002	Slotted ring	2.28		0.082	0.057	0.025	0.58	0.37	1.29	1847.90	1497.32	0.81					2.50	Steel pintle body	
003	Slotted ring	2.19		0.071	0.049	0.022	0.49	0.35	2.15	1840.80	1448.00	0.79					3.00		
004	Slotted ring	2.03		0.067	0.045	0.022	0.48	0.26	2.03	1802.80	1517.60	0.84					3.00	Some pintle tip erosion	
005	Slotted ring	2.68		0.071	0.052	0.019	0.52	0.42	4.07	1859.60	1528.50	0.82					3.00	Copper pintle body	
006	Slotted ring	3.52		0.072	0.056	0.016	0.59	0.27	2.13	1826.90	1715.00	0.94					3.00		
007	Slotted ring	1.90		0.079	0.052	0.027	0.49	0.53	2.75	1778.90	1319.83	0.74					3.20		
008	Slotted ring	2.13		0.082	0.056	0.026	0.62	0.31	2.16	1834.40	1595.95	0.87					3.20		
009	Slotted ring	2.67		0.094	0.068	0.026	0.74	0.24	2.42	1865.10	1664.83	0.89					3.20	No video recorded	
010	Slotted ring	3.82		0.095	0.076	0.019	0.79	0.27	1.98	1774.40	1733.50	0.97					3.50		
001	Circular orifices	3.22		0.100	0.076	0.024	0.79	0.30	1.99	1831.00	1682.00	0.92				4.00	Firing duration incremented		
002	Circular orifices	2.80		0.087	0.064	0.023	0.69	0.26	2.14	1859.60	1672.00	0.90				4.00	No pintle tip damage		
003	Circular orifices	2.65		0.089	0.065	0.024	0.71	0.27	1.95	1865.60	1669.00	0.89				4.00	No pintle tip damage		
004	Circular orifices	3.50		0.099	0.077	0.022	0.77	0.28	1.69	1804.60	1651.00	0.91				4.00	No pintle tip damage		
005	Circular orifices	3.15		0.100	0.076	0.024	0.79	0.27	1.83	1837.30	1647.00	0.89				4.50	100-[ms] increase in LCH ₄ valve lag		

Table 7.3.: Phase I - Summary of Results. (continued)

Run #	Injection Element	O/F Overall [-]	O/F Core [-]	\dot{m}_T [kg/s]	\dot{m}_{LO_2} [kg/s]	\dot{m}_{LCH_4} [kg/s]	$(p_k)_o$ [MPa]	Δp_{LO_2} [MPa]	Δp_{LCH_4} [MPa]	C_{theo}^* [m/s]	$C_{exp_p}^*$ [m/s]	$\eta_{C_F}^*$ [-]	Thrust, P [N]	$C_{exp_F}^*$ [m/s]	$\eta_{C_F}^*$ [-]	\dot{Q}_{Total} [MW]	\dot{Q}_{Nozzle} [MW]	Run Duration [s]	Comment
006	Circular orifices	3.10		0.088	0.067	0.021	0.69	0.25	1.82	1836.20	1650.40	0.89	No thrust information					4.50	400-[ms] LCH ₄ valve lag
007	Circular orifices	3.05		0.090	0.068	0.022	0.72	0.26	2.01	1842.60	1658.60	0.90						5.00	LCH ₄ valve lag decreased to 200 [ms]
008	Circular orifices	2.64		0.080	0.058	0.022	0.63	0.19	1.73	1864.10	1679.70	0.90						4.50	No pintle tip damage
009	Circular orifices	3.48		0.090	0.070	0.020	0.71	0.26	1.69	1763.50	1662.00	0.94						4.50	No pintle tip damage
010	Circular orifices	2.01		0.092	0.068	0.034	0.78	0.33	2.84	1813.40	1598.90	0.88						5.00	Trim orifices re-adjusted

Slotted Ring Configuration Tests

The slotted ring (rectangular orifice) was the first configuration tested. Following conclusion of the first three test runs, the injector was inspected for damage. Figure 7.15 shows a post-firing view of the original 1.4541 pintle body after these tests. Despite the erosion of the material, the investigation proceeded with the spare steel pintle body, until copper parts became available.



Figure 7.15.: Post-firing view of injector pintle body and replacement.

What follows is a description of Run 009 and the corresponding pressure and temperature data collected.

- ▶ Run 009: Following the previous tests, it appeared that chamber pressure oscillations might be occurring because of erratic propellant supply and insufficient chill-down of the injection head. To allow more adequate propellant flow and injection conditions, improved injector cool-down was implemented. However, pressure oscillations were still present. Figures 7.16 and 7.17 show pressure and temperature traces for this test, respectively. Figure 7.18 is a plot of axial temperatures obtained for the firing in steady-state conditions. Circumferentially, temperatures can be regarded as uniform. A characteristic peak in temperature values is observed at an axial distance of ca. 100 [mm] from the faceplate and corresponds to measurements obtained with the nickel chamber segment.

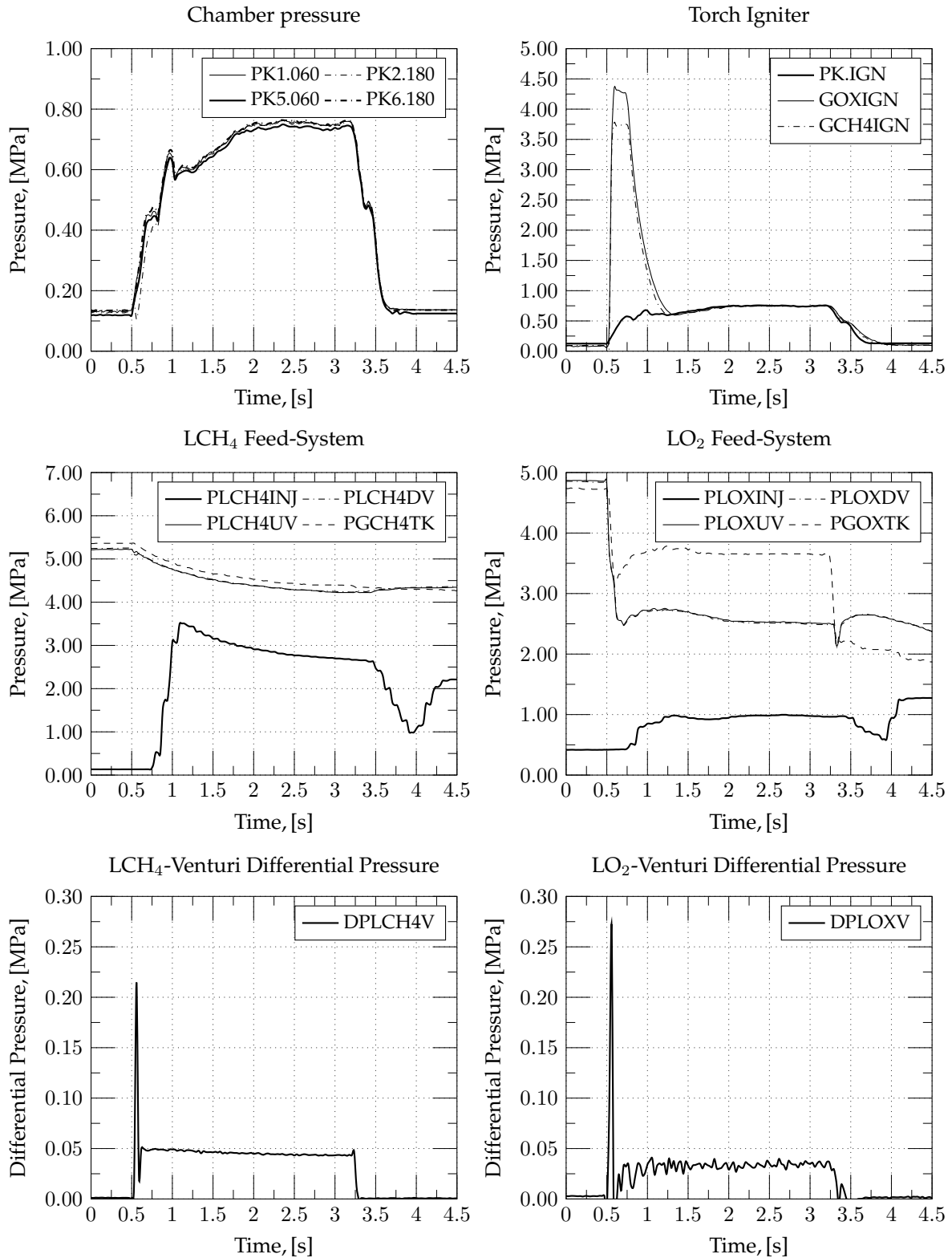


Figure 7.16.: Pressure traces for Run 009 (Injector 1).

7. Experimental Results

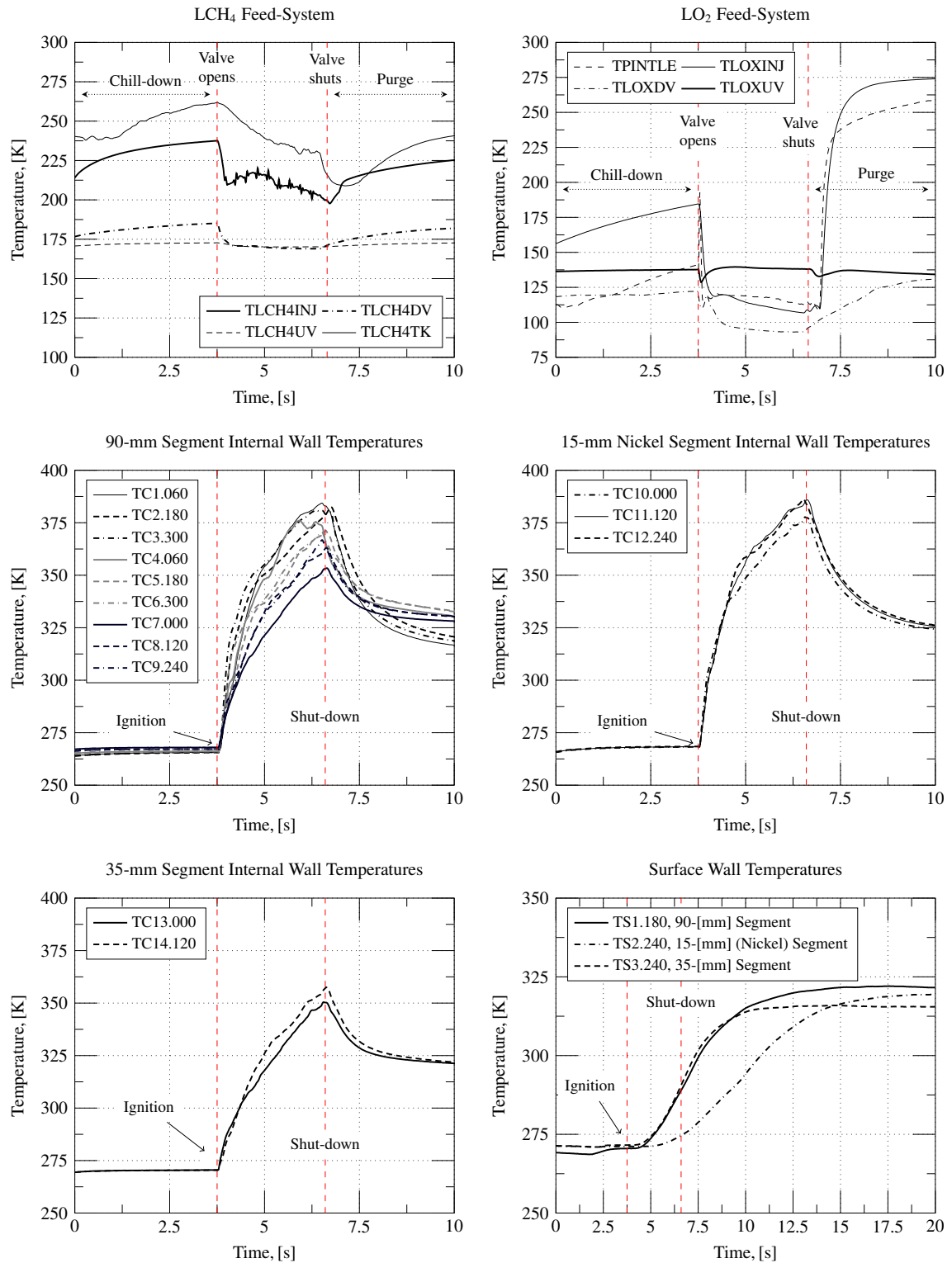


Figure 7.17.: Plots of temperature history for Run 009 (Injector 1).

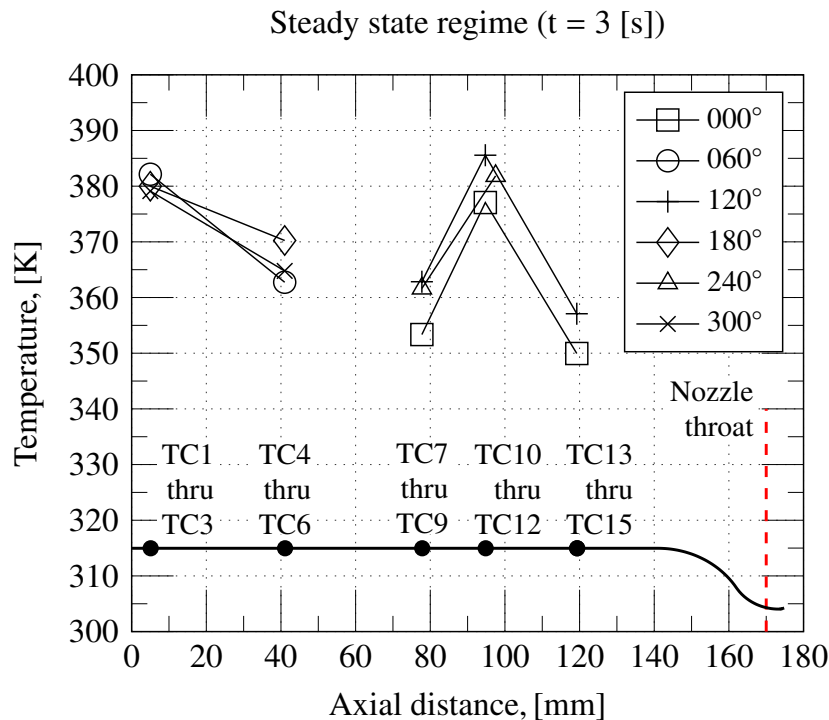


Figure 7.18.: Axial and circumferential temperature variation for Run 009 (Injector 1).

Circular Orifice Configuration Tests

The objective of this test series was to investigate the effect of orifice shape on performance and improve pintle tip heat rejection. Using the same design injection velocity ratio of Injector 1, 12 orifices were employed resulting in a slightly higher blockage factor with improved LO_2 flow path and hydraulic characteristics. Following erosion of the 1.4541 pintle tip, materials of higher heat conductivity were used for the pintle body and orifice ring. These measures allowed an increase in run duration to up to 5 seconds. After a series of runs, ten tests were regarded for subsequent analysis. The first two tests conducted were intentional duplicates of previous runs with the slotted ring configuration, except that chamber pressures were slightly higher, remaining within 0.6 and 0.8 [MPa]. Difficulties with the test stand still prevented a precise test point (e.g. mixture ratio and chamber pressure) to be reached. What follows is a description of Run 003.

- Run 003: Shown in Figure 7.27 is the aspect of the exhaust flame during this test run. Two-phase flow apparently occurred in the feed lines and might have caused transients in injector pressure drops and combustion. Figure 7.19 represents the pressure traces obtained for this run and confirms that transients occur during start-up and that steady-state conditions are barely reached. Post-firing analysis revealed no damage to pintle body or chamber. Figure 7.20 illustrates feed-system temperature traces and chamber transient temperature data, with transient conditions being evident on

7. Experimental Results

both propellant feed lines. By inspecting Figure 7.21 circumferential temperature deviations are pronounced closer to the injector faceplate; these deviations tended to smooth out along the chamber length.

After conclusion of this test series, the injector was removed from the test stand so that changes could be made in the oxidizer orifice and pintle body. At the same time, the engine hardware was examined thoroughly for any signs of erosion or damage. No damage was found either in the injector, chamber or nozzle. Some soot deposition was found on the injector faceplate; however, the carbon was very light and powdery indicating a probable low-temperature combustion.

Preliminary Injector Performance

Preliminary performance (C^* efficiency) for Injectors 1 and 2 were evaluated as a function of the oxidizer-to-fuel mixture ratio and momentum ratio. The calculation of characteristic velocity followed by the chamber pressure method and the C^* efficiency was calculated as indicated in Section C. In this case, no corrections were made for engine friction losses, throat area change or heat losses to the chamber wall. The final precision in η_{C^*} was $\pm 4.5\%$ for one standard deviation. Figure 7.22 present measured characteristic velocity and C^* efficiency for both configurations. It is noted that the performance obtained with Injector 2 is less sensitive to changes in mixture ratio. At low mixture ratios, Injector 1 presents a substantial drop in performance but matches Injector 2 as mixture ratio increases. Figure 7.23 shows C^* efficiency as a function of momentum ratio. Use of this information for Injector 1 is rather limited because of the large spread in the data; for Injector 2 a trend exists which indicate increase in performance as momentum ratio moves towards unit.

7.2.3. Injector Modifications

In reviewing the data from the previous test runs, it was clear that for some of these tests, the LCH_4 injection pressure drops were not close to the design value. The fuel injector which had been designed for a maximum pressure drop of 0.6 [MPa] neared 2.0 [MPa] in those hot-firings. Since the fuel injection gap had been set at 0.10 [mm], it was suspected that LCH_4 film boiling behind the injection point restricted the fuel flow leading to increased pressure drops. In order to complete the injector design and characterize the proper operating conditions, a series of cold-flow (no combustion) tests using the real propellants were conducted to determine the pre-conditioning necessary for unrestricted injector operation at the nominal operating conditions. These tests showed that the injector body should be ideally cooled between 120 [K] (methane side) to 90 [K] (oxygen side) before ignition and the LCH_4 should be at approximately 110 [K] upon reaching the main valve to ensure that no boiling occurs in the injector upon injection. Additionally, to avoid constricted fuel operation it was decided to modify the original LCH_4 flow path and increase the fuel gap to 0.2 [mm]. Modifications to the LO_2 injector included (1) increase the inside diameter of the injector sleeve to decrease flow approach velocity in conjunction with reduction in pintle body diameter and (2) re-design of the flow path to improve LO_2 discharge conditions. As previously mentioned, within the framework of these hot-fire

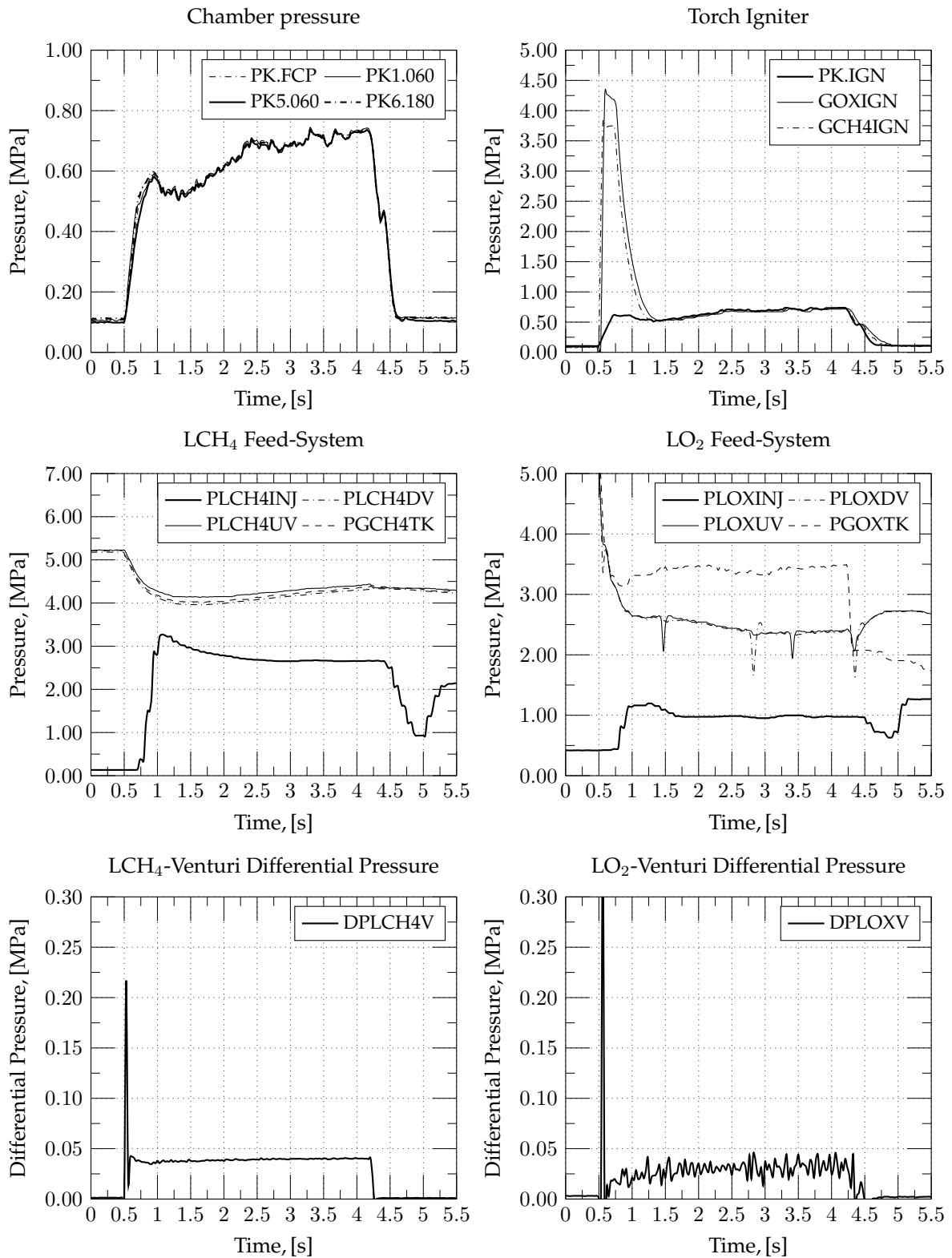


Figure 7.19.: Pressure traces for run 027a (circular).

7. Experimental Results

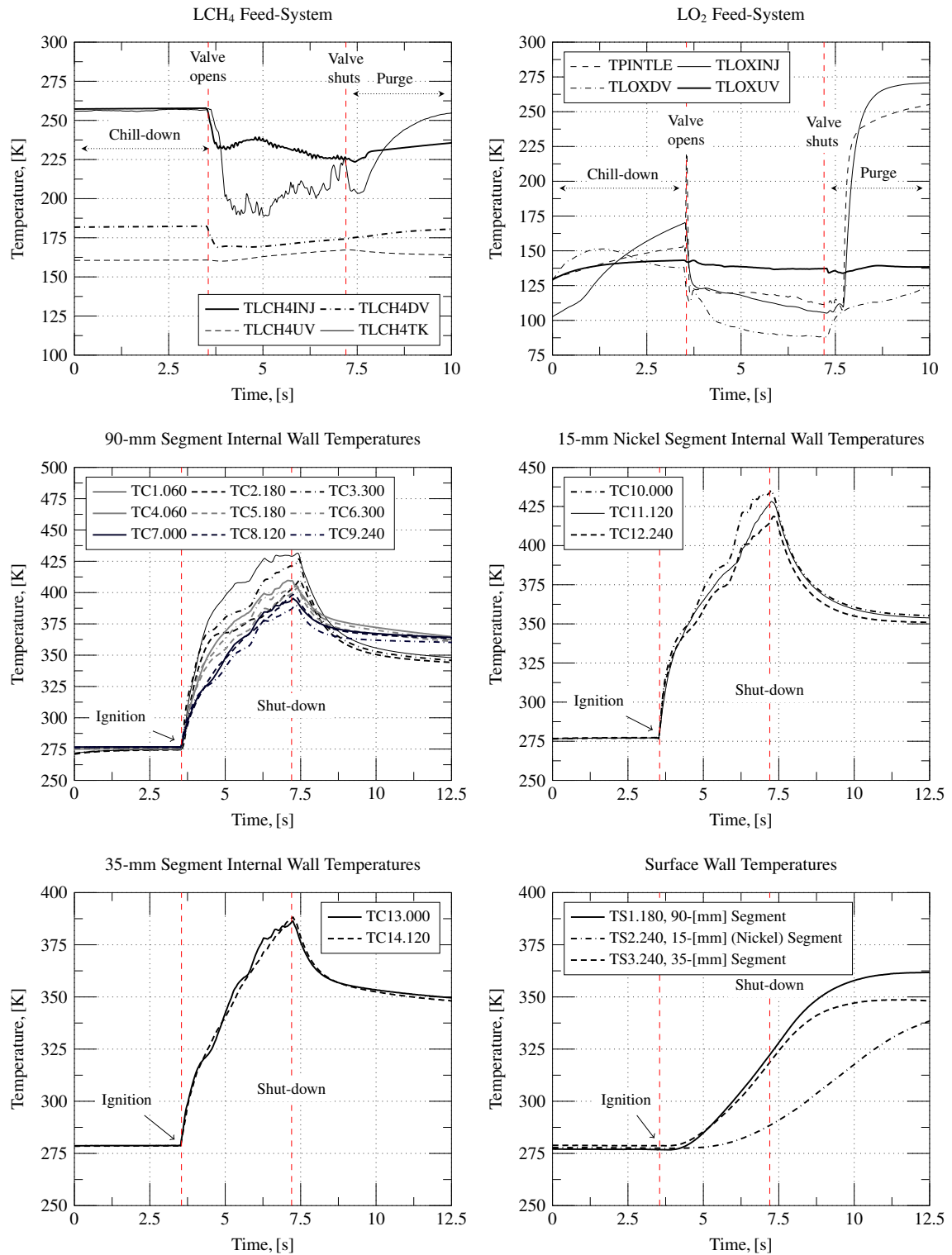


Figure 7.20.: Plots of temperature history for Run 003 (Injector 2).

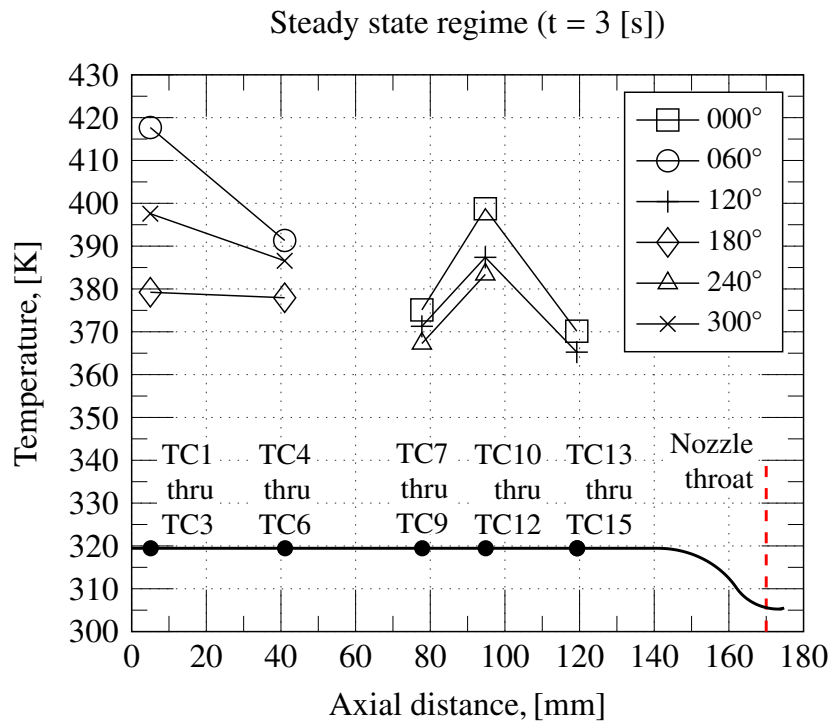


Figure 7.21.: Axial and circumferential temperature variation for Run 003 (Injector 2).

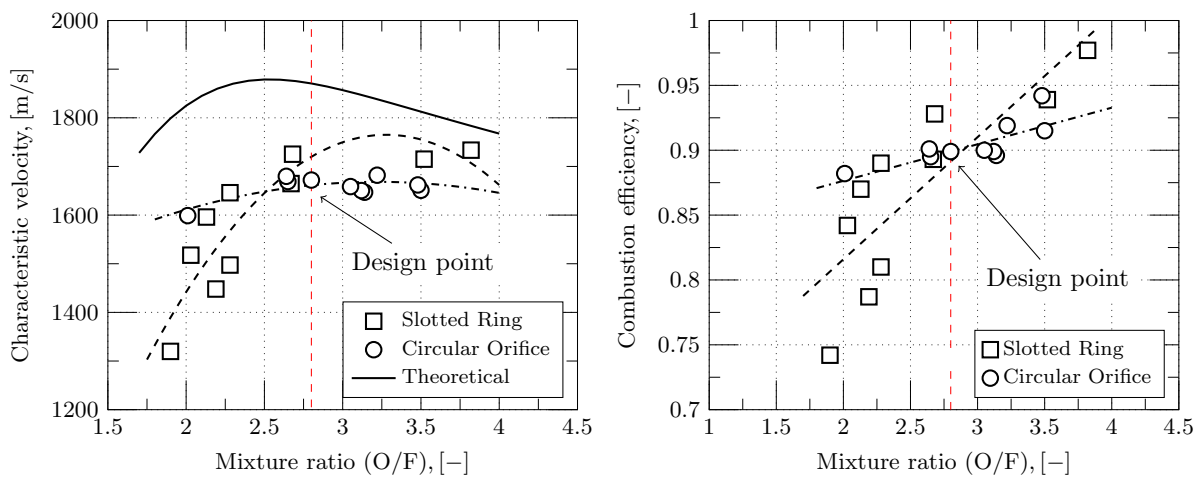


Figure 7.22.: Computed performance comparison for the slot and circular orifices.

experiments, additional changes were made to the basic configuration to primarily investigate the effect over pintle durability and performance. All the tests were performed with the rectangular LO_2 orifices, a shorter chamber length and the nominal contraction ratio of 13. Figure 7.25 shows the envelope of chamber pressures and mixture ratios investigated.

7. Experimental Results

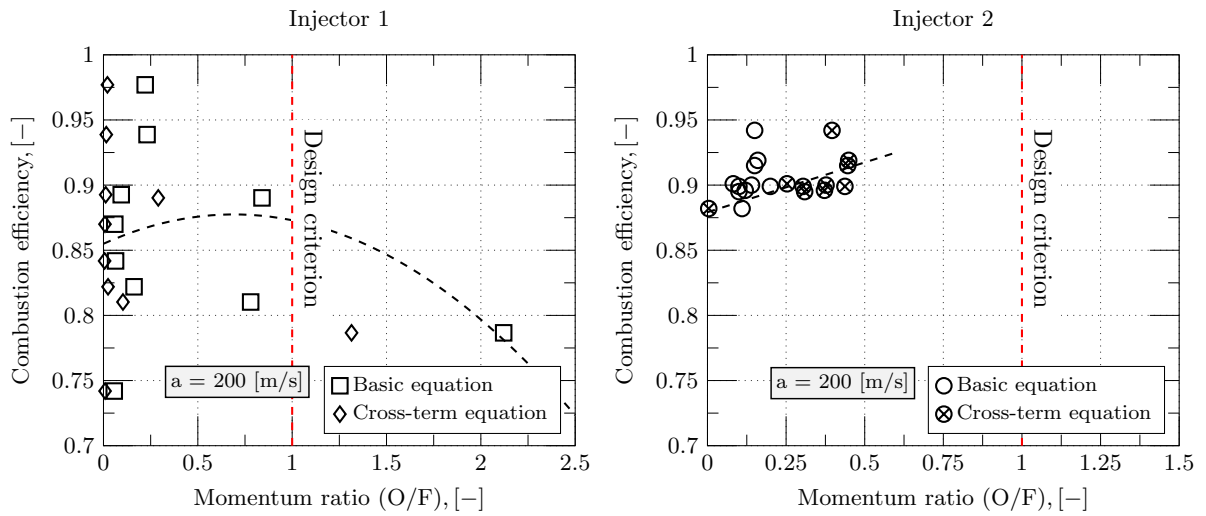


Figure 7.23.: Effect of propellant force ratio (TMR) on characteristic velocity efficiency.

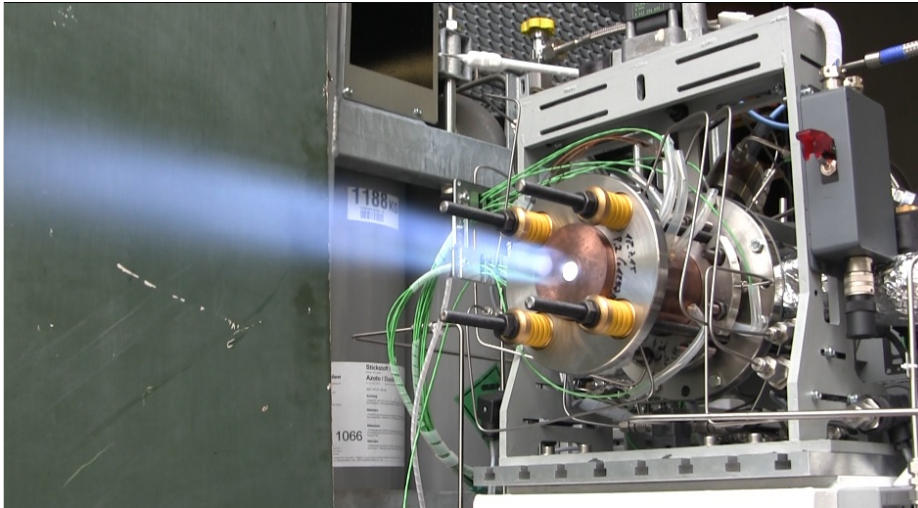


Figure 7.24.: View of hot-fire test for Run 003 (Injector 2).

It is noted that for Injectors 3 and 4 chamber pressures predominated in the range within 0.5 to 1.0 [MPa], with most of the runs for Injectors 5 and 6 reaching values between 1.0 and 1.5 [MPa].

Summary of Injector Performance

The resulting injection pressure drops were closer to the design values than in previous tests. Unfortunately, some of the issues with the propellant supply met during basic injector development would persist in subsequent tests and could not be entirely solved. Eventually, large transients and rough combustion were observed at the start-up and again were apparently caused by two-phase flow in the fuel feed system. These transients that were occurring throughout the run made it difficult to assign true performance steady-

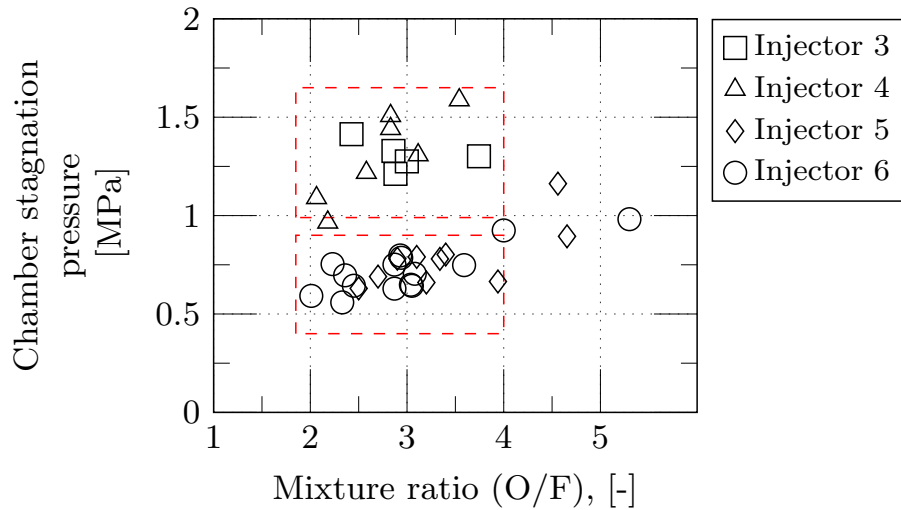


Figure 7.25.: Chamber pressure and mixture ratio map for the second phase of tests.

state values. Some of the runs, however, provided acceptable test data. Figures 7.27 and 7.26 are representative of these tests.

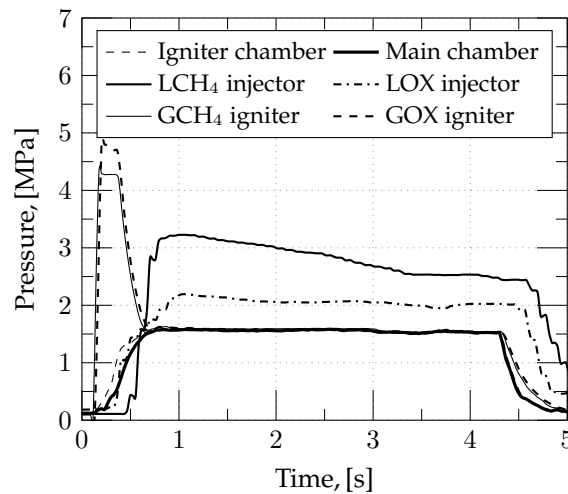


Figure 7.26.: Representative pressure traces.

Limited performance of Injectors 3 and 4 at 1.5 [MPa] chamber pressure is given in Figure 7.28. Injector 3 made use of a reduced skip ratio, in an attempt to remove the injector from the core of the combustion zone. This action solely could not prevent failure of the pintle material and tests with Injector 3 were terminated. As a result, the cooled pintle tip was introduced in the form of Injector 4. The latter provided improved injector durability, as well as enhanced ignition characteristics, possibly due to the axial pattern of LO₂ cooling streams interacting with the more fuel-rich torch igniter flame. Cooling the tip, however, provided only short-term solution to the overheat problem and degradation of the material resulted after several test runs, preventing any subsequent assessment of In-

7. Experimental Results

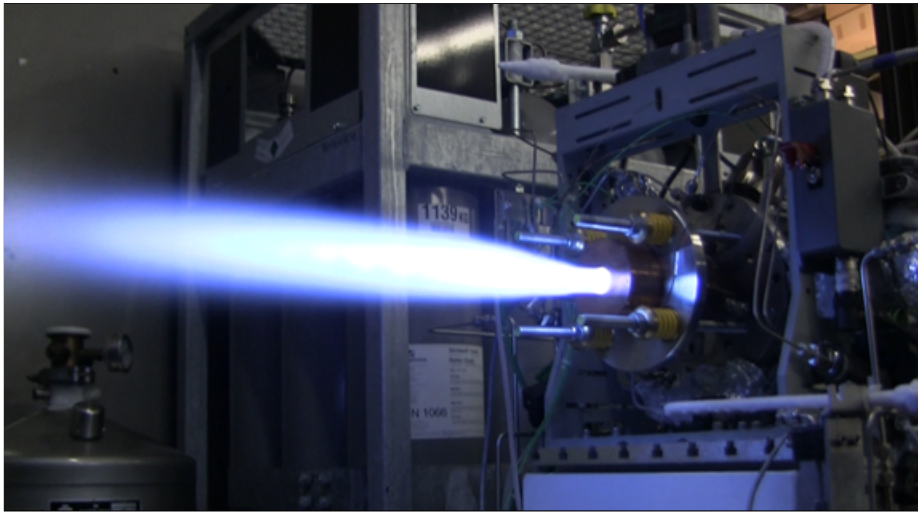


Figure 7.27.: Hot-fire test run (Injector 5).

jector 4. Performance at the nominal engine mixture ratio of 2.8, was around $\eta_{C^*} = 92.5$ percent for both injector configurations. The characteristic velocity efficiencies of Injectors 3 and 4 as a function of injection momentum and velocity ratios are given in Figure 7.29. For the propellant injection conditions encountered, oxidizer-fuel momentum ratios lie well below unit, with performance apparently increasing for Injector 4 as momentum and velocity ratios increase.

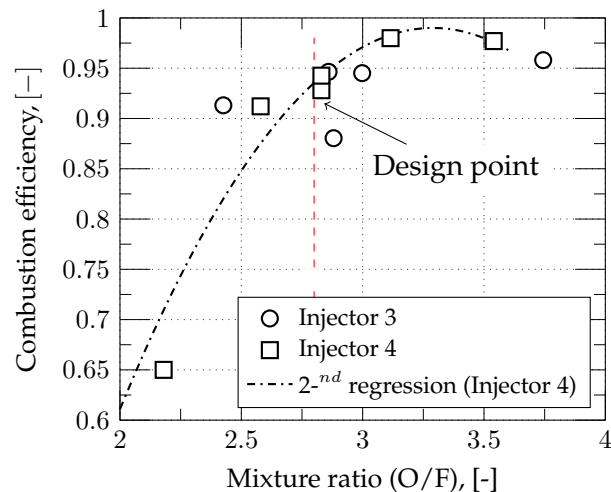


Figure 7.28.: Corrected efficiency η_{C^*} for Injectors 3 and 4.

Figure 7.30 gives the η_{C^*} of Injectors 5 and 6 at 1.0 [MPa] chamber pressure as a function of the chamber global mixture ratio (without correction for cooling flow). Included in Figure 7.30 are the computed values of η_{C^*} obtained via chamber pressure and thrust measurements, as described in Sections C.1.1 and C.1.2. The good agreement is thus a strong verification of overall data consistency. The heat rejection, friction, nozzle throat

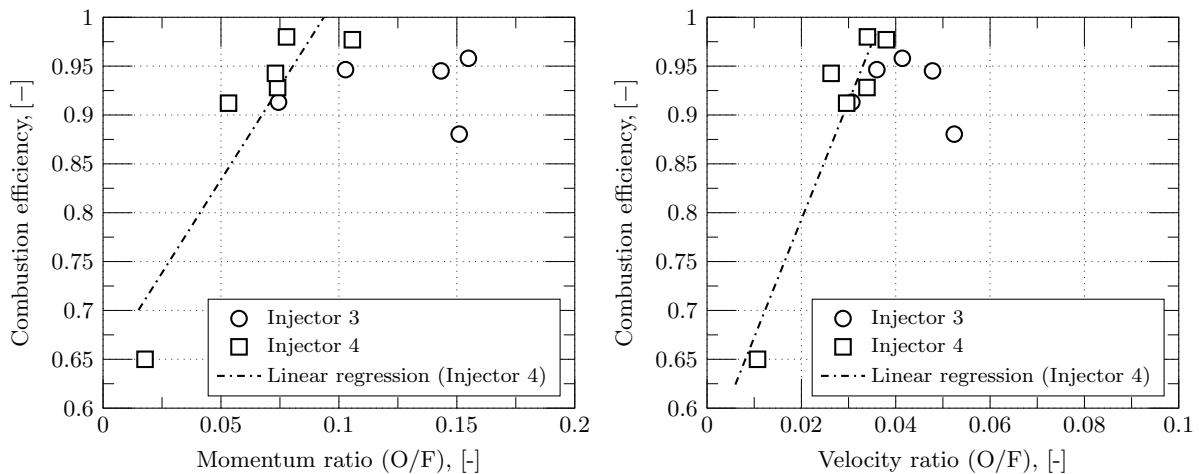


Figure 7.29.: Trend in characteristic velocity efficiency for Injectors 3 and 4 as a function of oxidizer-to-fuel momentum- and velocity-ratios.

diameter change and nozzle discharge coefficient corrections to measured characteristic velocity are defined in Appendix C together with the corresponding factors to derive characteristic velocity from thrust. Correction of the mixture ratio for Injector 6 to reflect the conditions of the interacting sprays only, is given in Figure 7.31. Although the cooling flow did not participate directly in the initial interaction process, it was felt that correction in η_{C^*} was not necessary. The intense central re-circulation fan, characteristic of pintle injectors, apparently leads the cooling flow to mix downstream of the injection point, ultimately contributing to chamber pressure build-up and thrust generation. According to Figure 7.31, both injectors were 83 percent efficient at the design point. Figure 7.32 shows that Injector 5 is less sensitive to variations in momentum ratio. As shown in Figure 7.33, similar to Injectors 3 and 4, performance increases as momentum and velocity ratios increase for Injector 6. These figures represent a trend, since not enough data is available to envelope the complete spectrum of injection velocities. Besides that, and in regard to all test runs, knowledge of the exact fluid temperatures that could better describe real injection conditions was very limited if not impossible to obtain with the present setup.

Tests with Injectors 5 and 6 were considered very successful in that reasonable performance ($C^* \approx 85$ percent) was achieved with no signs of injector or throat erosion. The fact that the orifice ring was made of 1.4541 stainless steel and did not show any signs of erosion during a 5-second firing indicated the injector element was running cool. It is believed, therefore, that the introduction of the ramp definitely solved the overheat issue by moving the combustion zone away from the tip. Injectors 3 and 4 had improved performance, however. The reason for this is probably the decelerating effect the ramp created in the flow of fuel. This resulted in non-uniform momentum exchange with zones where propellant did not ideally react. The fuel deflector occasionally created ignition difficulties and although a perfectly suitable explanation for this anomaly has not been devised, it is possible that for some injection conditions the flame could not be properly anchored.

7. Experimental Results

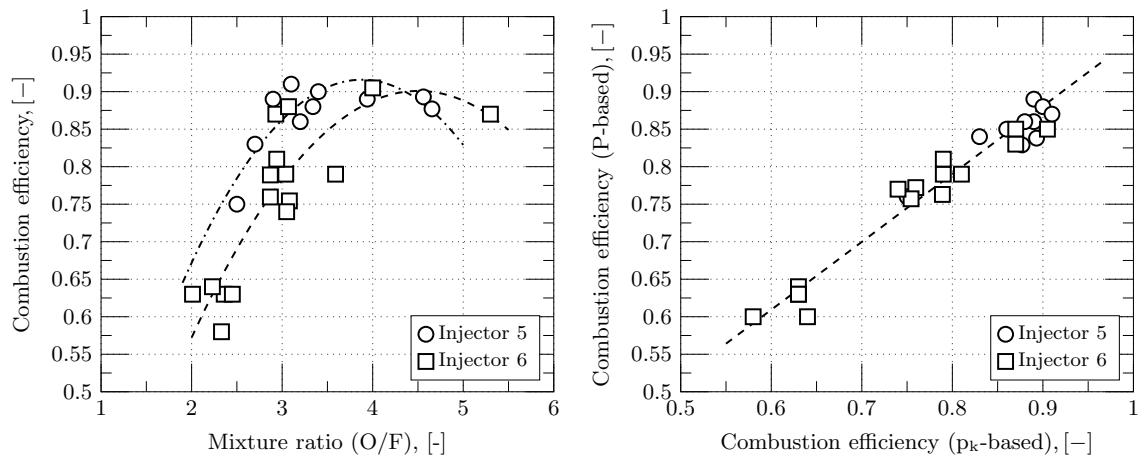


Figure 7.30.: Overall performance for Injectors 5 and 6 and comparison of thrust- and chamber pressure-based methods of η_{C^*} computation.

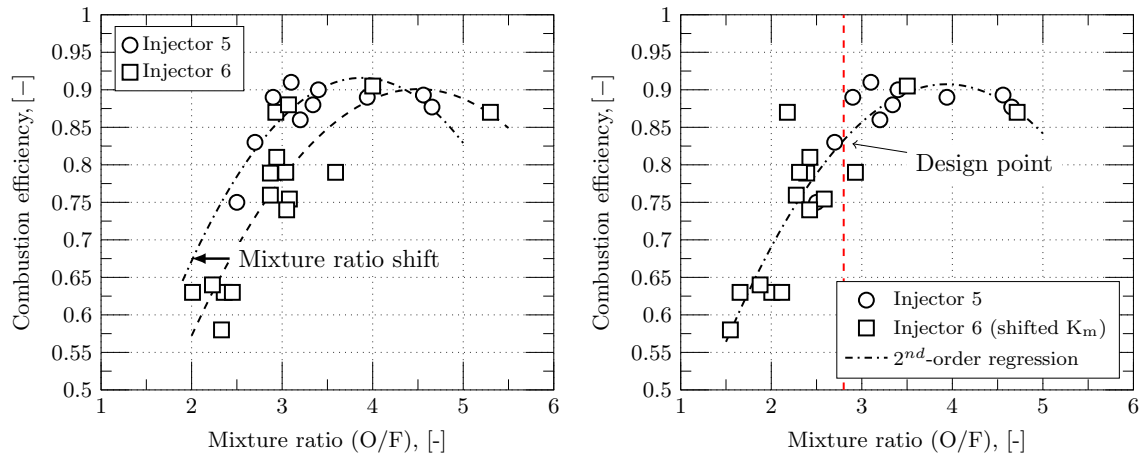


Figure 7.31.: Corrected performance of Injector 6 to account for LO₂ flow tip cooling.

7.3. Conclusions

The experimental effort was sufficient to establish the qualitative characteristics of the fixed-area pintle injector design for throttling applications. Two uncooled thrust chamber configurations were designed and test fired. The nominal design included a chamber pressure of 2.5 [MPa] and mixture ratio of 2.8. Test operating conditions were limited to the facility propellant supply capabilities and reached a maximum chamber pressure of only 1.5 [MPa] over a range of mixture ratios. Variations around the baseline injector design generated five additional configurations. The results of the test effort are summarized as follows:

1) Injector 1, the baseline design, and Injector 2, possessed a relatively large skip ratio based on the initial design criteria. These tests basically revealed that a value below unit is necessary to minimize pintle tip erosion. Performance was ca. 90% for both injectors

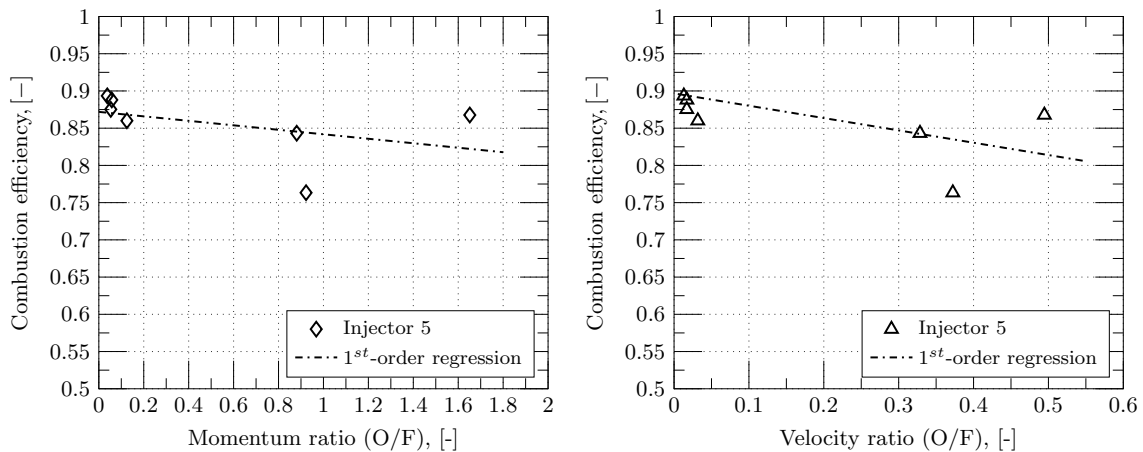


Figure 7.32.: Combustion efficiency for Injector 5 as a function of oxidizer-to-fuel momentum- and velocity-ratios.

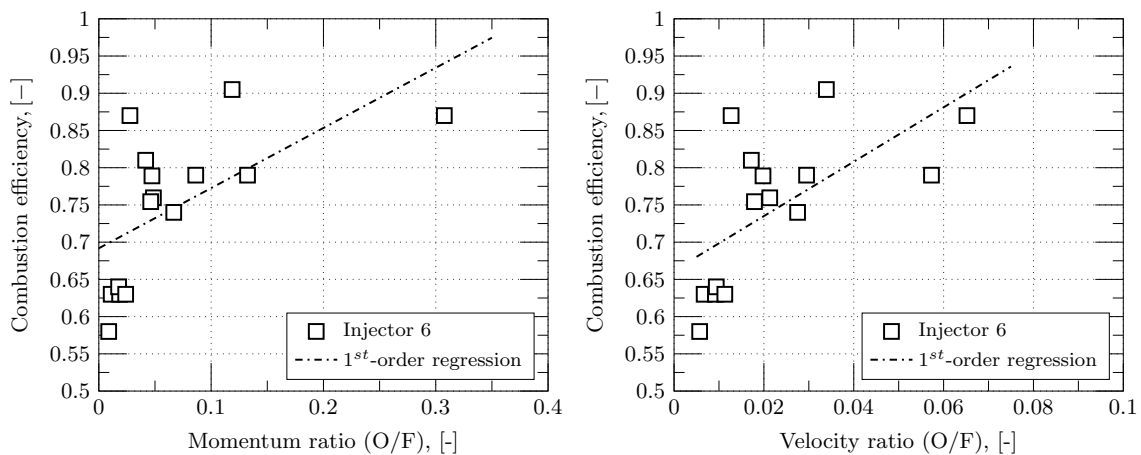


Figure 7.33.: Combustion efficiency for Injector 6 as a function of oxidizer-to-fuel momentum- and velocity-ratios.

at an L^* of 1.50 [m]. Injector 2 had a 10% larger blockage factor and was apparently less sensitive to changes in mixture ratio;

2) The third injector configuration saw a 45% reduction in skip ratio with respect to the baseline version. Performance data at the nominal mixture ratio indicated high performance, with values around 92.5 percent for C^* efficiency and the same L^* of previous tests. Tests were terminated resulting from failure of the pintle tip due to overheating;

3) Injector 4 was identical to the third configuration, except that it incorporated an actively-cooled pintle tip. Cooling was effected by flowing 10% of the LO_2 -flow through four, 0.5-[mm] holes in the pintle tip. Tests at 1.5 [MPa] resulted in similar combustion efficiency around the nominal mixture ratio as Injector 3 and improved ignition characteristics. After several firings, the pintle material failed structurally;

4) Deflection of the methane flow out of the pintle tip region, forcing impingement out-

7. Experimental Results

side of the central combustion chamber zone, considerably enhanced pintle tip life and reduced throat erosion at the cost of lower performance. At a chamber pressure of 1.0 [MPa] this modified injector had a combustion efficiency of 83 percent around the nominal mixture ratio and at a characteristic length L^* of 1.50 [m]. In order to assess the influence of tip cooling with the presence of the ramp, a last configuration was tested. These tests indicated no considerable influence of additional pintle tip cooling in the characteristic velocity efficiency;

5) Values of combustion efficiency in terms of momentum and velocity ratio were presented for all injectors, although in a rather limited form. It became apparent for almost all configurations that as momentum and velocity ratios increase there is an accompanying increase in performance. However, the assumption of unit momentum ratio as a condition for maximizing performance could not be entirely verified in the tests. Whereas the controlling parameter could be momentum rather than velocity, the information available does not supply any distinction;

6) Although not investigated, there is sufficient reason to believe that through adequate design of the deflector, an improvement in performance and dependable operation can be attained. With the addition of secondary radial orifices and a modified ramp angle, the possibility to organize chamber mixture ratio and related chamber-wall heat transfer characteristics may be created.

Part VI.

Conclusions and Future Work

8. Conclusions and Recommendations

8.1. Analytical Results

The initial task in the analytical investigation was to select a mission model for further study and establish basic propulsion system requirements. Based on a simplified payload optimization study, a maximum thrust of 1100 [N] was determined for a 500-[kg] class Lander using a set of four fixed-thrust engines. A resulting thrust-to-Mars-weight ratio of approximately 2.4:1 was shown to be rather independent of vehicle size. A more detailed evaluation is recommended to assess the effects of aerodynamic forces and required landing maneuvers on the final engine thrust level. Additionally, further investigation will be required to include flight control characteristics, such as attitude control and guidance component considerations. A minimum thrust modulation of 6:1 was selected based on experience with past flight programs, and should allow larger tolerances to starting, trajectory and terminal landing errors.

Propulsion system analytical studies were conducted to determine potential chamber cooling design approaches with LO_2/LCH_4 , with emphasis on the regenerative and film cooling concepts. Computer routines were developed in MATLAB to assist the parametric analyses of both single propellant- and dual propellant-cooled thrust chamber designs, and to determine the applicability of each as active thrust chamber cooling methods. The analytical performance evaluation showed dual-regen cooling to have expected delivered performance (corrected I_{sp}) of 3447 [m/s] against 3329 [m/s] for supercritical single-regen LO_2 cooling. These two cooling concepts appeared to be the most advantageous in terms of engine thermal design. However, the necessity to increase coolant pressures beyond what is common practice for pressure-fed systems ruled out regenerative cooling as a viable option for the proposed unmanned Mars Lander descent propulsion system. Therefore, the film-cooling concept has been finally selected for that purpose, with an estimated I_{sp} of 3113 [m/s], a value which is compatible with the previous payload optimization study.

Following study and survey of various potential throttling concepts, a conventional upstream flow control and fixed-area injection system was selected to fulfill mission requirements. The decision was based on simplicity, cost and short development time. This was, of course, only a comparative analysis and more detailed studies would be warranted to determine more precise rankings for each candidate throttling approach on the basis of delivered specific impulse and overall propulsion system weight.

8.2. Experimental Results

In reality, the experimental effort involved more than hot-fire testing the proposed injector designs. It required many hours of conception, design and construction of a new cryogenic test stand, with all the equipment required for propellant production, gauging,

8. Conclusions and Recommendations

thermal conditioning and the electronics for data acquisition and engine control.

The six pintle injector configurations evaluated showed the design criterion of unit skip ratio to create some injector durability issues. Initial tests with both the rectangular and circular LO_2 orifices showed similar performance, with Injector 2 being less affected by mixture ratio excursions. Subsequent reduction of the skip ratio in Injectors 3 and 4 had no negative effect in performance and resulted in slight improvement in injector durability. Pintle tip cooling with LO_2 alone seemed ineffective in removing the combustion zone from the face of the injector, but provided better ignition characteristics.

Injector durability was fully established with the introduction of the fuel ramp in Injector 5. A large number of firings with over 150 seconds of accumulated time have been accomplished with no problems. However, performance seemed to be greatly affected by the ramp. It became evident, that empirical adjustment of the geometries of the oxidizer and fuel elements are necessary to optimize combustion efficiency.

The contraction ratio change essentially resulted in the same performance for Injectors 3 and 4 as with the long chamber of the initial tests. This was not too surprising since the L^* was about the same as the extended chamber. Of interest was the fact that chamber pressure was higher for runs with Injectors 3 and 4 and no significant increase in performance has occurred. These results strongly suggest that the performance of the injector was not atomization controlled, but instead was primarily controlled by mixture ratio and mass distribution control. This conclusion was made since the burning rate should be proportional to the chamber pressure. The results indicated that some performance gain optimization was still possible with Injectors 5 and 6 through mixture ratio control brought about by variation in the angle of the ramp and re-sizing of the oxidizer elements.

Although the research scope did not permit optimization of the performance/resultant wall environment characteristics of the pintle injector, it did provide preliminary design criteria applicable to future gas- and liquid-liquid LO_2/LCH_4 propellant engine designs.

8.2.1. Operating Conditions

Difficulties with the test stand propellant supply (especially with the LCH_4 liquefier) precluded the nominal liquid-liquid injection pattern proposed to be thoroughly investigated. In some of the tests, two-phase flow effects may have affected injector and chamber operation, impeding the approach of a steady-state regime. However, fluctuations in propellant thermal conditioning might exist in the actual operational environment and two-phase flow start-ups may be of real significance. The off-nominal conditions observed during the experimental effort are representative of those fluctuations.

8.3. Future Research

The accomplishments of this research have provided useful data on the application of the LO_2/LCH_4 propellants to low thrust rocket engine designs. The injector concept developed for this study enabled a rapid empirical adjustment of the parts to be made, once the baseline design was established. The build-up of a new test stand for cryogenic LO_2/LCH_4 propellants has laid out the groundwork for future testing of similar injector elements. The experimental activities have demonstrated reasonably good combustion performance

characteristics ($\eta_{C*} \approx 85\%$) with the pintle injector design, culminating with excellent overall injector durability. Additional investigations are required, however, to further refine and optimize this design approach from both a cooling and engine performance standpoint.

The use of the mechanical patternator technique for cold-flow evaluation of the mass and mixture ratio distribution is encouraged for further research of this injector type. Although not conclusive, test results obtained with the patternator showed some promise as an aid in design for minimum wall heat transfer.

The pressure drop characteristics of the injector require additional investigation. The oxidizer pressure drops were acceptable, whereas the fuel pressure drops needed to be reduced. However, in the experimental approach no particular effort was made to improve injector discharge coefficients. As an example, the hydraulic path leading to the oxidizer orifices was not optimum and all orifices were sharp-edged. The fuel flow straightener ensured uniform fuel flow distribution, but presented sharp edges which probably degraded pressure drop characteristics.

Further work is also recommended with other chamber design approaches, e.g. regenerative cooling with supercritical LO_2 and with both propellants, in combination with a turbo-alternator/expander cycle. With these design concepts, additional attention must be given to the injector design employed to maintain defined liquid propellant injection and injector durability under the possibly higher imposed heat loads. The pintle concept allows control of the wall environment and resulting heat flux with minimal adjustments in injector geometry or pressure drop ratios. This will additionally require more detailed heat transfer measurements to show the magnitude and distribution of heat fluxes both axially and circumferentially.

Another area warranting investigation is the dynamic rating of the injector through induced pulse techniques, already accomplished with UDMH and NTO propellants. Additional effort is required with LO_2/LCH_4 propellants.

Finally, once the fixed-area injector element has been fully characterized, a central objective of future work should be the assessment of dynamic thrust modulation by injector and upstream valving to obtain measurements of steady-state performance parameters, such as characteristic exhaust velocity and thermal parameters such as heat fluxes near the injector face and the chamber wall, and combustion dynamic characteristics throughout the throttling range. To accomplish these goals, new and improved test facility infrastructure to allow adequate cryogenic propellant supply appears to be necessary.

Appendix

A. Propellant Physical and Transport Properties

A.1. Liquid Oxygen Physical and Transport Properties

Table A.1.: Physical Properties of Oxygen [115]

Molecular weight [$\frac{\text{kg}}{\text{kmol}}$]	32,0
Freezing (melting) point, [K]	54.3
Boiling point, [K]	90.17
Density at 90.17 [K], [$\frac{\text{kg}}{\text{m}^3}$]	1140.0
Critical temperature, [K]	154.4
Critical pressure, [MPa]	4.97
Critical density, [$\frac{\text{kg}}{\text{m}^3}$]	430.0
Vapor pressure at 90.17 [K], [MPa]	0.16
Surface tension at 90.17 [K], [$\frac{\text{mN}}{\text{m}}$]	13.2
Dynamic viscosity at 90.17 [K], [mPa·s]	0.190

A.2. Liquid Methane Physical and Transport Properties

Table A.2.: Physical Properties of CH₄ [115]

Molecular weight [$\frac{\text{kg}}{\text{kmol}}$]	16.03
Freezing (melting) point, [K]	89.2
Boiling point, [K]	111.66
Density at 111.66 [K], [$\frac{\text{kg}}{\text{m}^3}$]	415.0
Critical temperature, [K]	190.7
Critical pressure, [MPa]	4.58
Critical density, [$\frac{\text{kg}}{\text{m}^3}$]	162.0
Vapor pressure at 111.66 [K], [MPa]	0.1
Dynamic viscosity (91.6 [K]), [mPa·s]	0.0035
Dynamic viscosity (194.7 [K]), [mPa·s]	0.0076

B. Computer Routines

B.1. Computer Program for Thrust Chamber Cooling Analyses

The digital program uses the one-dimensional equations to calculate steady-state regenerative and radiation cooling parameters. A simplified model is used to estimate film-coolant requirements. The MAIN program calls subroutines which may be classified into three groups: the input-output subroutines, the system subroutines and the data handling subroutines.

B.1.1. Input-Output Subroutines

INPUT sets constants used in other subroutines

OUTPUT prints desired variables

PLOTWRITE plots and saves final results

B.1.2. System Subroutines

GEOMETRY calculates thrust chamber coordinates and dimensions

RADIA calculates the nozzle wall temperature distribution with radiation cooling

REGEN solves one-dimensional regenerative cooling equations for a given geometry, cooling direction (counter- or parallel-flow) and determines cooling channel dimensions, gas- and liquid-side temperature distributions

FILM calculates amount of film-coolant fraction and chamber mixture ratio distributions

B.1.3. Data-Handling Subroutines

TRANSPORTCOOLANTCH4 two-dimensional interpolation of fuel transport properties (uses the REFPROP [69] database as reference)

TRANSPORTCOOLANTLOX two-dimensional interpolation of oxidizer transport properties (uses the REFPROP [69] database as reference)

TRANSPORTGAS three-dimensional interpolation of combustion chamber gas transport properties

WALLCOND database for wall material/thermal coating heat conductivities

B.2. One-Dimensional REGEN Code Listing

```
1 function REGEN(varargin)
2
3 % -----
4 % Regenerative cycle computation
5 % -----
6
7 % Thermal information
8 % -----
9 T0k=Ttc (:, :, 1);
10 Taw=r*(effCstar^2)*T0k;
11
12 % Fluid and combustion mixture properties
13 % -----
14 % Gas mixture
15 % -----
16 transpG=TRANSPORTGAS;
17 CpG=@transpG.CpG;
18 MuG=@transpG.MuG;
19
20 % Coolant properties
21 % -----
22 % Coolant property tables & functions
23 % -----
24 load -mat cpch4
25 load -mat much4
26 load -mat kch4
27 load -mat dch4
28 transpLCH4=TRANSPORTCOOLANTCH4(cpch4, much4, kch4, dch4);
29 % -----
30 load -mat cplox
31 load -mat mulox
32 load -mat klox
33 load -mat dlox
34 transpLOX=TRANSPORTCOOLANTLOX(cpllox, mulox, klox, dlox);
35 % -----
36
37     if flagCoolant==1
38
39         TCoolant0=TcoolIn;
40         PcritCoolant=46.1;
41         TcritCoolant=190.6;
42         mcool=mkf;
43         CpL=@transpLCH4.CpLCH4;
```

```

44     MuL=@transpLCH4.MuLCH4;
45     kL=@transpLCH4.kLCH4;
46     dL=@transpLCH4.dLCH4;
47
48     else
49
50         TCoolant0=TcoolIn;
51         PcritCoolant=51.02;
52         TcritCoolant=154.0;
53         mcool=mkox;
54         CpL=@transpLOX.CpLOX;
55         MuL=@transpLOX.MuLOX;
56         kL=@transpLOX.kLOX;
57         dL=@transpLOX.dLOX;
58
59         if flagCoolant == 2
60
61             TCoolant0=298;
62             mcool=mkw;
63             CpL=@transpH2O.CpH2O;
64             MuL=@transpH2O.MuH2O;
65             kL=@transpH2O.kH2O;
66             dL=@transpH2O.dH2O;
67
68             end
69
70     end
71
72     a = zeros(size(xSegm));
73     b = zeros(size(xSegm));
74     t=2*pi.*(ySegm+tW)./vNChannel;
75     Dh=2.*a.*b./(a+b);
76     Rh=a.*b./(2.*(a+b));
77     ratioIto=curvITO./Rh;
78
79     % Wall-temperature distribution estimates
80     % -----
81     vectorTwgInit=TwgRadInit;
82     vectorTLInit=((560-TCoolant0)/(xSegm(end)-xSegm(1))).*xSegm+
83         TCoolant0; %
84
85     % Pressure distribution estimate
86     % -----
87     DeltaPTest=0;
88     vectorPLInit=PcoolIn-((DeltaPTest)/(xSegm(end)-xSegm(1))).*xSegm;

```

B. Computer Routines

```
89 % Pre-allocating memory
90 % -----
91 hG=zeros ( size (xSegm) );
92 qConvG=zeros ( size (xSegm) );
93 qTotalG=zeros ( size (xSegm) );
94 QTotalG=zeros ( size (xSegm) );
95 sigmaBartz=zeros ( size (xSegm) );
96 % -----
97 ReL=zeros ( size (xSegm) );
98 PrL=zeros ( size (xSegm) );
99 hL=zeros ( size (xSegm) );
100 NuRef=zeros ( size (xSegm) );
101 dLratio=zeros ( size (xSegm) );
102 AreaL=zeros ( size (xSegm) );
103 f=zeros ( size (xSegm) );
104 fatorITO=zeros ( size (xSegm) );
105 ff=zeros ( size (xSegm) );
106 % -----
107 VelL=zeros ( size (xSegm) );
108 DeltaPFriction=zeros ( size (xSegm) );
109 DeltaPManifold=zeros ( size (xSegm) );
110 DeltaPMomentum=zeros ( size (xSegm) );
111 PLCalc=zeros ( size (xSegm) );
112 PLCalcInSeg=zeros ( size (xSegm) );
113 PLCalcOutSeg=zeros ( size (xSegm) );
114 % -----
115 kWratio=zeros ( size (xSegm) );
116 kW=380*ones ( ( size (xSegm) ) );
117 m=zeros ( size (xSegm) );
118 etaFin=ones ( size (xSegm) );
119 B1=zeros ( size (xSegm) );
120 % -----
121 TwL=zeros ( size (xSegm) );
122 TwgCalc=zeros ( size (xSegm) );
123 Tfilm=zeros ( size ( (xSegm) ) );
124 qTotalCalcG=zeros ( size (xSegm) );
125 QTotalGCalc=zeros ( size (xSegm) );
126 % -----
127 iter=ones ( ( size (xSegm) ) );
128 tol=ones ( size (xSegm) );
129 tolPress=ones ( size (xSegm) );
130 % -----
131
132 if coolDirection==0
133     in=1;
134     out=length (xSegm) ;
```

```
135     step=1;
136 else
137
138     if coolDirection==1
139
140         in=RAD;
141         out=1;
142         step=-1;
143         vectorTLInit=vectorTLInit(end:-1:1);
144         vectorPLInit=vectorPLInit(end:-1:1);
145
146     end
147
148 end
149
150 TLCalc=vectorTLInit;
151
152 for seg=in:step:out
153
154     while ( tolPress(seg) ) > 0.0005
155
156         tol(seg)=1;
157
158         while ( tol(seg) > 0.00001 )
159
160             TwgInit=vectorTwgInit(seg);
161             TLInit=vectorTLInit(seg);
162             valDm=Dm(seg);
163             valdeltaSG=deltaS(seg);
164             valdeltaX=deltaX(seg);
165             valNChannel=vNChannel(seg);
166             caracol=vcaracol(seg);
167             valDh=Dh(seg);
168             vala=a(seg);
169             valb=b(seg);
170             valtFin=tFin(seg);
171             valtW=tW(seg);
172             valt=t(seg);
173             pkPropG=pkaxis(seg);
174             Machaxis=Maxis(seg);
175             gammatc=gammaaxis(seg);
176             rbarraITO=ratioIto(seg);
177             cg=Cg(seg);
178
179             % Gas-side
180             % _____
```

B. Computer Routines

```
181     Tfilm(seg) = 0.5*(Taw+TwgInit);
182     hG(seg) = 0.895*cg*CpG(pkPropG, Tfilm(seg), Km) * (MuG(
        pkPropG, Tfilm(seg), Km))^0.18*(mk^0.82/valDm^1.82)
        *(Taw/TwgInit)^0.35;
183     qConvG(seg) = 1.000*hG(seg)*(Taw-TwgInit);
184     qTotalG(seg) = qConvG(seg) + qradG(seg);
185     QTotalG(seg) = (qConvG(seg) + qradG(seg)) * valdeltaSG;
186
187     % Liquid side
188     % -----
189     ReL(seg) = 2*mcool / ((vala+valb)*MuL(TLInit, vectorPLInit
        (seg))*valNChannel);
190     PrL(seg) = CpL(TLInit, vectorPLInit(seg))*MuL(TLInit,
        vectorPLInit(seg))/kL(TLInit, vectorPLInit(seg));
191
192     if rbarraITO == 0
193
194         fatorITO(seg) = 1;
195
196     else
197
198         fatorITO(seg) = (ReL(seg) * (rbarraITO)^2) ^ (sign(
            rbarraITO)*0.05);
199
200     end
201
202     if (vectorPLInit(seg) > PcritCoolant)
203
204         if (iter(seg) == 1)
205
206             hL(seg) = etaFin(seg) * 0.022 * (kL(TLInit,
                vectorPLInit(seg))/valDh) * ReL(seg)
                ^ 0.8 * PrL(seg) ^ 0.4 * (fatorITO(seg));
207
208             else
209
210                 if coolCorrelation == 1
211
212                     % LOX & Methane correlation used for
                        supercritical regimes:
213                     dLratio(seg) = dL(TLInit, vectorPLInit(
                            seg))/dL(TLInit, vectorPLInit(seg))
                            ;
214                     kWratio(seg) = WALLCOND(TLCalc(seg))/
                            WALLCOND(TwL(seg));
215                     NuRef(seg) = 0.0025 * ReL(seg) * (PrL(seg))
```

```

216         ^0.4;
        hL(seg)=etaFin(seg)*((kL(TLInit,
            vectorPLInit(seg))/valDh))*NuRef(
            seg)*(dLratio(seg))^(−0.5)*(
            kWratio(seg))^(0.5)*((CpL(0.5*(TwL
            (seg)+TLCalc(seg)),vectorPLInit(
            seg)))/(CpL(TLCalc(seg),
            vectorPLInit(seg))))^(2/3)*(
            vectorPLInit(seg)/PcritCoolant)
            ^(-1/5)*(1+2/(ds(seg)/valDh))*(
            fatorITO(seg));

217
218     else
219
220     % Correlation for Methane
221     hL(seg)=etaFin(seg)*0.022*(kL(TLInit,
            vectorPLInit(seg))/valDh)*ReL(seg)
            ^0.8*PrL(seg)^0.4*(TLCalc(seg)/TwL
            (seg))^0.45*(fatorITO(seg));

222
223     end
224
225     end
226
227     else
228
229     % Haines Correlation (superheat/
            subcritical pressures)
230     hL(seg)=etaFin(seg)*0.005*(kL(TLInit,
            vectorPLInit(seg))/valDh)*ReL(seg)
            ^0.95*PrL(seg)^0.4*(fatorITO(seg));

231
232     end
233
234     % Conduction – fin computation
235     % _____
236     kW(seg)=WALLCOND(0.5*(TwgCalc(seg)+TwL(seg)));
237
238     % Modelo Vasiliev para computo da aleta
239     m(seg)=sqrt(((2*hL(seg)*(ds(seg)/cos(deg2rad(caracol))
            +valtFin))/(kW(seg)*valtFin*ds(seg)/cos(deg2rad(
            caracol))));
240     B1(seg)=2*(ds(seg)*(1/cos(deg2rad(caracol))))*(valb+
            vala/2)*tanh(m(seg)*(valb+vala/2))/(m(seg)*(valb+
            vala/2));
241     etaFin(seg)=1-(valtFin/valt)*(1/cos(deg2rad(caracol))

```

```

) + B1(seg) / (valt * ds(seg));
242
243 % Wall temperature internal calculation
244 TwL(seg) = (hL(seg) * (1 + kW(seg) / (hG(seg) * valtW)) * TLCalc(
    seg) + (kW(seg) / valtW) * Taw + gradG(seg) * kW(seg) / (valtW
    * hG(seg))) / (kW(seg) / valtW + hL(seg) * (1 + kW(seg) / (
    valtW * hG(seg))));
245 TwgCalc(seg) = (hG(seg) * Taw + (kW(seg) / valtW) * TwL(seg) +
    gradG(seg)) / (hG(seg) + (kW(seg) / valtW));
246
247 % Total heat flux internal calculation
248 qTotalCalcG(seg) = hG(seg) * (Taw - TwgCalc(seg)) + gradG(seg)
    );
249
250 % Coolant temperature & pressure distribution
251 % -----
252 f(seg) = 0.0055 * (1 + (2e4 * rugW / valDh + 1e6 / ReL(seg))^(1/3));
253 AreaL(seg) = a(seg) * b(seg);
254
255 if coolDirection == 0
256
257 % Same direction coolant flow
258     if seg == 1
259         TLCalc(seg) = TCoolant0 + 1 * (0.5 * qTotalCalcG(seg) *
            deltaS(seg)) / (mcool * CpL(0.5 * (vectorTLInit(seg)
            + TCoolant0), PcoolIn));
260         VelL(seg) = (mcool / valNChannel) / (dL(TLCalc(seg),
            PcoolIn) * AreaL(seg));
261         DeltaPFriction(seg) = (1e-5 * f(seg) * (valdeltaX / valDh
            ) * dL(TLCalc(seg), PcoolIn) * VelL(seg)^2) / 2;
262         DeltaPManifold(seg) = 1e-5 * Kmanifold * dL(TLCalc(seg)
            , PcoolIn) * VelL(seg)^2 / 2;
263         DeltaPMomentum(seg) = 0;
264         PLCalc(seg) = PcoolIn - (valNChannel * (DeltaPFriction(
            seg) / 2 + DeltaPMomentum(seg)) + DeltaPManifold(seg)
            ));
265     else
266         TLCalc(seg) = (vectorTLInit(seg) + TLCalc(seg - 1))
            / 2 + 1 * (0.5 * qTotalCalcG(seg) * deltaS(seg)) / (mcool
            * CpL(0.5 * (vectorTLInit(seg) + TLCalc(seg - 1)),
            vectorPLInit(seg)));
267         VelL(seg) = (mcool / valNChannel) / (dL(TLCalc(seg),
            vectorPLInit(seg)) * AreaL(seg));
268         DeltaPFriction(seg) = (1e-5 * f(seg) * (valdeltaX / valDh
            ) * dL(TLCalc(seg), vectorPLInit(seg)) * ((VelL(seg)
            ) + VelL(seg - 1)) / 2)^2) / 2;

```

```

269      DeltaPMomentum(seg)=1e-5*(mcool^1/(valNChannel*(
          AreaL(seg)+AreaL(seg-1))))*abs((VelL(seg)-VelL
          (seg-1)));
270      PLCalcInSeg(seg)=(PLCalc(seg-1)-vNChannel(seg-1)
          *(DeltaPFriction(seg-1)/2));
271      PLCalc(seg)=PLCalcInSeg(seg)-vNChannel(seg)*(
          DeltaPFriction(seg)/2+DeltaPMomentum(seg));
272      PLCalcOutSeg(seg)=PLCalc(seg)-vNChannel(seg)*(
          DeltaPFriction(seg)/2+DeltaPMomentum(seg));
273      end
274
275      else
276
277      % Counter direction coolant flow
278      if seg==in
279          TlCalc(seg)=TCoolant0+1*(0.5*qTotalCalcG(seg)*
          deltaS(seg))/(mcool*CpL(0.5*(vectorTLInit(seg)
          +TCoolant0),vectorPLInit(seg)));
280          VelL(seg)=mcool/(dL(TlCalc(seg),PcoolIn)*AreaL(
          seg)*valNChannel);
281          DeltaPFriction(seg)=1e-5*f(seg)*(valdeltaX/valDh)
          *dL(TlCalc(seg),PcoolIn)*VelL(seg)^2/2;
282          DeltaPManifold(seg)=1e-5*Kmanifold*dL(TlCalc(seg)
          ,PcoolIn)*VelL(seg)^2/2;
283          DeltaPMomentum(seg)=0;
284          PLCalc(seg)=PcoolIn-(DeltaPFriction(seg)/2+
          DeltaPMomentum(seg))-DeltaPManifold(seg);
285      else
286          TlCalc(seg)=(vectorTLInit(seg)+TlCalc(seg+1))
          /2+1*(0.5*qTotalCalcG(seg)*deltaS(seg))/(mcool
          *CpL(0.5*(vectorTLInit(seg)+TlCalc(seg+1)),
          vectorPLInit(seg)));
287          VelL(seg)=mcool/(dL(TlCalc(seg),vectorPLInit(seg)
          )*AreaL(seg)*valNChannel);
288          DeltaPFriction(seg)=1e-5*f(seg)*(valdeltaX/valDh)
          *dL(TlCalc(seg),vectorPLInit(seg))*((VelL(seg)
          +VelL(seg+1))/2)^2/2;
289          DeltaPMomentum(seg)=1e-5*(mcool^1/(valNChannel*(
          AreaL(seg)+AreaL(seg+1))))*abs((VelL(seg)-VelL
          (seg+1)));
290          PLCalcInSeg(seg)=(PLCalc(seg+1)-vNChannel(seg+1)
          *(DeltaPFriction(seg+1)/2));
291          PLCalc(seg)=PLCalcInSeg(seg)-vNChannel(seg)*(
          DeltaPFriction(seg)/2+DeltaPMomentum(seg));
292          PLCalcOutSeg(seg)=PLCalc(seg)-vNChannel(seg)*(
          DeltaPFriction(seg)/2+DeltaPMomentum(seg));

```

B. Computer Routines

```
293         PLCalcInSeg(seg)=(PLCalc(seg+1)-(DeltaPFriction(
294             seg+1))/2);
295         PLCalc(seg)=PLCalcInSeg(seg)-(DeltaPFriction(seg)
296             /2+DeltaPMomentum(seg));
297         PLCalcOutSeg(seg)=PLCalc(seg)-(DeltaPFriction(seg)
298             /2+DeltaPMomentum(seg));
299     end
300
301     QTotalGCalc(seg)=qTotalCalcG(seg)*valdeltaSG;
302
303     tol(seg)=abs((QTotalG(seg)-QTotalGCalc(seg))/((QTotalGCalc(
304         seg))));
305
306     vectorTwgInit(seg)=0.5*(TwgCalc(seg)+vectorTwgInit(seg));
307
308     vectorTLInit(seg)=0.5*(TLCalc(seg)+vectorTLInit(seg));
309
310     end
311
312     tolPress(seg)=abs((vectorPLInit(seg)-PLCalc(seg))/((PLCalc(
313         seg))));
314     vectorPLInit(seg)=0.5*((PLCalc(seg)+vectorPLInit(seg)));
315     iter(seg)=iter(seg)+1;
316     end
317
318     end
319
320     qL=hL.*(TwL-TLCalc);
321
322     end
323
324 % End of REGEN
```

C. Calculation of Characteristic Velocity Efficiency

C.1. Methods of Computation

The index of injector performance used in this study was the corrected combustion efficiency. The correction is necessary inasmuch as it isolates the effects of mixing and vaporization, the two factors of more relevance in injector performance evaluation. By assuming initially a perfect injector, the efficiency attributed to a particular injector design will be:

$$\eta_{C^*} = \frac{C_{exp}^*}{C_{idealinj}^*}. \quad (C.1)$$

where $C_{idealinj}^*$ is the characteristic velocity that would be obtained with a perfect injector. This value equals the theoretical equilibrium characteristic velocity corrected for effects of throat geometry, chemical kinetics, boundary layer and chamber heat losses. Two independent methods were used for calculating C_{exp}^* , one based on measurement of chamber pressure and the other on measurement of thrust.

C.1.1. Chamber Pressure Method

Characteristic velocity efficiency based on chamber pressure is defined as follows:

$$\eta_{C^*} = \frac{(p_k)_o (A_t)_{eff}}{\dot{m}_T C_{theo}^*}. \quad (C.2)$$

As mentioned previously, values obtained via Equation (C.2) are referred to as corrected characteristic velocity efficiencies, because the factors involved are obtained by application of suitable influence factor corrections to measured quantities. Stagnation pressure at the throat is obtained from measured static pressure at start of nozzle convergence by assumption of isentropic expansion and effective throat area is estimated from measured geometric area and from geometrical radius changes during firing and for non-unity nozzle discharge coefficient. Chamber pressure can be corrected to allow for energy losses from combustion gases to the chamber wall by heat transfer and friction. Equation (C.2) may therefore be written as follows:

$$\eta_{C^*} = \frac{p_k A_t f_p f_{TR} f_{DIV} f_{FR} f_{HL} f_{KE}}{(\dot{m}_o + \dot{m}_f) C_{theo}^*}. \quad (C.3)$$

The overall combustion efficiency of the chamber, i.e. without consideration of individual injector mixing and vaporization losses was simply computed as:

$$\eta_{C^*} = \frac{C^*_{Exp}}{C^*_{Theo}}. \quad (C.4)$$

where C^*_{CEA} is the theoretical value obtained through chemical equilibrium computations.

C.1.2. Calculations Based on Thrust

The alternate determination of characteristic velocity efficiency is based on thrust:

$$\eta_{C^*} = \frac{P_{vac}}{\dot{m}_T (K_p)_{vac} C^*_{theo}}. \quad (C.5)$$

Values of vacuum thrust are obtained by correcting the sea-level measurements. These corrected values can then be used in conjunction with theoretical thrust coefficients for calculation of C^* . Nozzle efficiency is taken as 100% if there is no combustion in the nozzle, if chemical equilibrium is maintained in the expansion process and if energy losses from the combustion gases are taken into account [70].

$$\eta_{C^*} = \frac{(P + p_a A_e) \phi_{FR} \phi_{DIV} \phi_{HL} \phi_{KE}}{(\dot{m}_o + \dot{m}_f) (K_p)_{theo} C^*_{theo}}. \quad (C.6)$$

In Equation (C.6), the correction factors are directly applied to vacuum thrust rather than the measured thrust, because, for convenience, the factors are readily calculated as changes in efficiency based on theoretical vacuum parameters. Implicit in the use of theoretical K_p values are corrections to geometric throat area and to measured static chamber pressure at the start of nozzle convergence. Therefore, calculation of corrected C^* efficiency from thrust measurement includes all factors of Equation (C.6) plus an additional one to account for divergence on the nozzle exit flow. Because $(K_p)_{theo}$ is essentially independent of small changes to chamber pressure and contraction ratio which are involved in corrections to p_k and A_t , these corrections are really of no practical significance in calculation of C^* from thrust measurements. Methods of estimation of the various correction factors are described in the JANNAF 245 Handbook [70]. Not all of the factors considered by Equations (C.5) and (C.6) were computed because of lack of experimental data. Typical values for the correction factors used are summarized as follows:

► Applicable to η_{C^*} based on Chamber Pressure:

- $f_p = 1.023$ (throat stagnation pressure)
- $f_{TR} = 0.995$ to 0.998 (transient throat effects)
- $f_{DIS} = 0.995$ to 1.000 (discharge coefficient)
- $f_{FR} = 1.000$ (friction)
- $f_{HL} = 1.000$ (heat loss)
- $f_{KE} = 1.000$ (kinetic)

► Applicable to η_{C^*} based on Thrust:

- $\phi_{FR} = 1.000$ (friction)
- $\phi_{DIV} = 1.020$ (divergence)
- $\phi_{HL} = 1.000$ (heat loss)
- $\phi_{KE} = 1.000$ (kinetic)

D. Mass Flow Computation from Venturi Meter Measurements

D.1. Data Reduction Procedure

Experimentally, both methods of combustion efficiency computation require knowledge of the mass flow rate of propellants. Calculation of total propellant mass flow takes a few steps and is obtained by considering venturi meter upstream pressure and temperature conditions and by calculating the corresponding flow velocity at the venturi throat:

$$V_{th} = \sqrt{\frac{(h_{line} - h_{th})}{\left[1 - \left(\frac{\rho_{th}}{\rho_{line}}\right)^2 \beta^4\right]}}. \quad (D.1)$$

where ρ_{th} is the propellant density and h_{th} the enthalpy at the venturi throat. The propellant thermodynamic state points at the venturi throat are obtained by assuming isentropic flow to the throat, i.e.,

$$s_{th} = s_{line}. \quad (D.2)$$

where s_{th} is the entropy at the venturi throat and s_{line} the entropy computed from upstream flow conditions.

In this case, pressure at the venturi throat p_{th} must be known:

$$p_{th} = p_{line} - \Delta p. \quad (D.3)$$

where Δp is the measured venturi pressure drop and p_{line} is the value of pressure read in the upstream mounting block.

In Equation (D.1), the parameter β is the line contraction ratio, defined as:

$$\beta = \frac{d_{th}}{d_{line}}. \quad (D.4)$$

where d_{line} and d_{th} are the line and venturi throat diameters, respectively.

The mass flow across any of the venturi meters can be calculated as follows:

$$\dot{m} = C_d A_{th} \rho_{th} V_{th}. \quad (D.5)$$

where C_d is the venturi discharge coefficient obtained from cold-flow calibrations. Figure D.1 presents typical signal traces obtained during testing for both venturi meters.

Finally, the total propellant flow is the sum of both propellant mass flow rates computed, namely:

$$\dot{m}_T = \dot{m}_{LO_2} + \dot{m}_{LCH_4}. \quad (D.6)$$

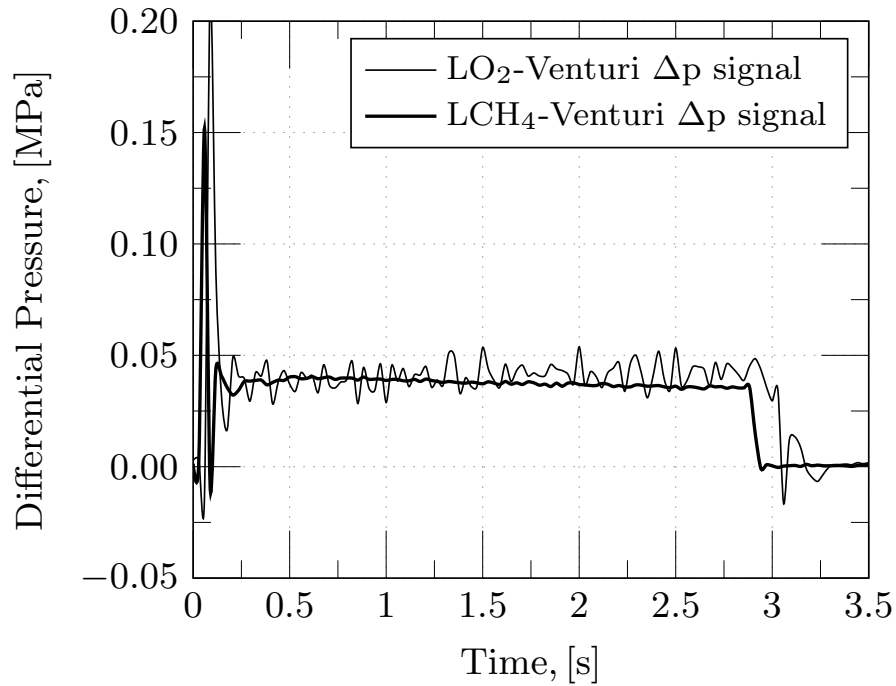


Figure D.1.: Representative pressure traces for the venturi meters.

From the raw test data, a timeframe of 0.01 [s], selected approximately 2.0 [s] after igniter operation had terminated, was used to compute the average values of static chamber pressure and differential pressure across the venturi meters. Temperatures and pressures in the mounting blocks upstream of the venturi meters changed very little during the firing; their average values were used to calculate propellant mass flow rates as described previously.

E. Uncertainty Analysis

The discussion presented here is meant to be a summary of the methods used. A full discussion of the approach used for uncertainty analysis is described in reference [70]. The parameter used in this study for characterization of the error in a given measurement is the uncertainty U , made up of bias B and precision S . Precision is the variation between repeated measurements and the standard deviation of this group of data points characterizes the random error. For samples containing more than 30 data points the error range can be generally regarded as twice the computed standard deviation and includes 95% of the total spread of measurements [70]. Depending on the characteristics of the measurement or group of data, different approaches may be used to calculate S [116]. In a very general way, the precision index S is given by:

$$S_X = \sqrt{\frac{\sum_{i=1}^N (X_i - \bar{X})^2}{N - 1}}. \quad (\text{E.1})$$

Bias represents the constant or systematic error. In repeated measurements, it is assumed that each data point has the same bias. Whereas precision can be estimated based on calibration and test history, unknown bias factors need to be estimated. Alternatively, the known components of bias can be eliminated by comparison with the true value. Sources of bias and precision error are assumed in this research to result from calibration, data acquisition and data reduction procedures. The root sum square method is used to combine these numerous sources of error. As a result, for the bias,

$$B = \sqrt{B_1^2 + B_2^2 + B_3^2 \dots + B_N^2}. \quad (\text{E.2})$$

where B_i is the systematic error of the i^{th} elemental source.

In a similar way, for the precision index:

$$S = \sqrt{S_1^2 + S_2^2 + S_3^2 \dots + S_N^2}. \quad (\text{E.3})$$

where S_i represents the precision index of the i^{th} error source involved. A single parameter describing both bias and precision and having a simple interpretation is highly desirable. The uncertainty interval is the most widely used approach:

$$U^\pm = B^\pm \pm tS. \quad (\text{E.4})$$

In other words, U represents the interval within which the true value is expected to lie, given a certain confidence level or coverage. In this study, a confidence level of 95% was considered:

$$U_{95}^\pm = B^\pm \pm t_{95}S. \quad (\text{E.5})$$

The value of t_{95} is a function of the number of degrees of freedom used in obtaining S . As mentioned previously, when the degrees of freedom of a certain measurement is higher than 30, t_{95} can be generally taken as $t_{95}=2$ [70]. Values for t_{95} can be found in tables for t-Student's distribution as a function of the degrees of freedom of the sample, calculated as follows [116]:

$$\nu = \frac{\left(\sum_{i=1}^N S_i^2\right)^2}{\sum_{i=1}^N \frac{S_i^4}{\nu_i}} \quad (\text{E.6})$$

where S_i is the spread or precision index resulting from the combination of the various error sources, and ν_i represents the degrees of freedom connected to each error source.

E.1. Total Uncertainty of a Measurement

The error in the measurement of a given parameter involved in the calculation of a final quantity can be propagated by use of influence coefficients describing the effect of a unit error in the parameter on the final result. If P_i represents the i^{th} parameter to be measured in order to obtain a quantity q , then the influence coefficients are given by:

$$\theta_i = \frac{\partial q}{\partial P_i}. \quad (\text{E.7})$$

Therefore, the precision of a given quantity S_q becomes

$$S_q = \sqrt{\sum_{i=1}^N (\theta_i S_{P_i})^2}. \quad (\text{E.8})$$

and for the bias sources:

$$B_q = \sqrt{\sum_{i=1}^N (\theta_i B_{P_i})^2}. \quad (\text{E.9})$$

To apply Equations (E.8) and (E.9) the uncertainties in the parameters P_i must be independent and random [70], using Equation (E.5) in the last step to obtain the total uncertainty of a result.

E.1.1. Characteristic Velocity

As described in Section C.1, the effects of mixing and vaporization need to be isolated, in order to discern the level of excellence of a given injector design. In order to accomplish this isolation, all other effects must be accurately estimated. However, the test data and the correction factors have uncertainties associated with them, resulting in an uncertainty in the isolated effect. The model used in calculating this corresponding uncertainty is:

$$U_{\eta_{C^*}}^{\pm} = \pm t_{95} \sqrt{S_{C_{exp}^*}^2 + S_{C_{FR}^*}^2 + S_{C_{DIV}^*}^2 + S_{C_{HL}^*}^2 + S_{C_{theo}^*}^2}. \quad (\text{E.10})$$

Each S factor in Equation (E.10) represents the change in injector efficiency caused by a change of magnitude S in the specific factor, as described by Equation (E.8).

Determination of Influence Coefficients

The computation of influence coefficients are required to propagate the errors of measured parameters associated with a final quantity. For analytical expressions, such as those given by Equation (D.1), the influence coefficients are obtained by partial differentiation with respect to the parameter of interest. Whenever thermodynamic properties are involved, a small perturbation around the nominal value was used. All propellant thermodynamic state points were calculated using the REFPROP program [69] supplied by the National Institute of Standards and Technology (NIST). Expressions for the influence coefficients and their typical values are summarized in Table E.1.

Particularly for the velocity at the venturi throat, it is interesting to describe the influence coefficients in terms of measured parameters, i.e. pressure and temperature in the line and pressure drop across the venturi. If κ is a calculated thermodynamic property (either enthalpy, temperature or density at the venturi throat), then the chain rule applies:

$$\frac{\partial \kappa}{\partial p_{line}} = \frac{\partial \kappa}{\partial p_{th}} \frac{\partial p_{th}}{\partial p_{line}} + \frac{\partial \kappa}{\partial s_{line}} \frac{\partial s_{line}}{\partial p_{line}}. \quad (E.11)$$

$$\frac{\partial \kappa}{\partial \Delta_p} = \frac{\partial \kappa}{\partial p_{th}} \frac{\partial p_{th}}{\partial \Delta_p}. \quad (E.12)$$

$$\frac{\partial \kappa}{\partial T_{line}} = \frac{\partial \kappa}{\partial s_{line}} \frac{\partial s_{line}}{\partial T_{line}}. \quad (E.13)$$

Equations (E.5) and (E.8) through Equation (E.13) plus expressions in Table E.1 formed the basis for the calculation of all C^* uncertainties.

Error Sources

Possible error sources associated with each instrument was carefully traced for calibration and data acquisition errors. In the case of pressure transducers, hysteresis and non-linearity were calibrated out using a precision electronic calibrator as reference. Sources of data acquisition errors originated from pressure sensor temperature variations during data collection and zero shift were mitigated by effecting the calibration at test conditions.

The venturi meters were periodically calibrated using water against high precision turbine or magnetic inductive type flowmeters. Discrepancies in the values of discharge coefficients obtained with water and the real, low viscosity propellants, were acknowledged.

Thermocouples used in the feed-system lines and combustion chamber were not calibrated; these were employed as per supplier stated precision standards. In the case of the combustion chamber, several sources of error influence the values of transient temperature. Some of these errors include disturbances in thermocouple reading due to roughness in combustion and chamber operation, uncertainty of the exact location of an inner-wall thermocouple and of the thermal properties of the combustion chamber wall material.

Thrust measurement errors due to a shift in load cell output signal caused by rigid propellant lines, valve connections and flexures were verified and compensated for prior to engine testing. Offset reading error was eliminated since the load cell was zeroed prior to each test fire. Errors due to misalignment between thrust chamber force vector and the resultant component measured by the load cell, as well as those resulting from misalignment of forces acting on an axis different from the engine centerline could not be entirely

E. Uncertainty Analysis

Table E.1.: Typical Values for the Influence Coefficients.

Parameter	Expression	Value	Units
p_{th}	$\frac{\partial p_{th}}{\partial p_{line}} = 1$	1	[Pa/Pa]
	$\frac{\partial p_{th}}{\partial p} = -1$	-1	[Pa/Pa]
β	$\frac{\partial \beta}{\partial d_{th}} = \frac{1}{d_{line}}$	0.170×10^0	[1/m]
	$\frac{\partial \beta}{\partial d_{line}} = -\frac{d_{th}}{d_{line}^2}$	0.690×10^{-1}	[1/m]
V_{th}	$\frac{\partial V_{th}}{\partial h_{line}} = \frac{1}{\sqrt{2} \sqrt{\frac{h_{line} - h_{th}}{[1 - (\frac{\rho_{th}}{\rho_{line}})^2 \beta^4]}}}$	0.590×10^{-1}	[s/m]
	$\frac{\partial V_{th}}{\partial h_{th}} = -\frac{\partial V_{th}}{\partial h_{line}}$	0.590×10^{-1}	[s/m]
	$\frac{\partial \beta}{\partial d_{line}} = -\frac{d_{th}}{d_{line}^2}$	0.258×10^{-1}	[m/s]
	$\frac{\partial V_{th}}{\partial \rho_{line}} = -\frac{\rho_{th}^2}{\rho_{line}^3} \frac{V_{th} \beta^4}{[1 - (\frac{\rho_{th}}{\rho_{line}})^2 \beta^4]}$	-0.190×10^{-2}	[m ⁴ /kg · s]
	$\frac{\partial V_{th}}{\partial \rho_{th}} = \frac{\rho_{th}}{\rho_{line}^2} \frac{V_{th} \beta^4}{[1 - (\frac{\rho_{th}}{\rho_{line}})^2 \beta^4]}$	0.190×10^{-2}	[m ⁴ /kg · s]
\dot{m}_o, \dot{m}_f	$\frac{\partial \dot{m}}{\partial p_{line}} = \frac{\partial \dot{m}}{\partial V_{th}} \frac{\partial V_{th}}{\partial p_{line}} + \frac{\partial \dot{m}}{\partial \rho_{th}} \frac{\partial \rho_{th}}{\partial p_{line}}$	0.410×10^{-9}	[m ³ · s/kg ²]
	$\frac{\partial \dot{m}}{\partial T_{line}} = \frac{\partial \dot{m}}{\partial V_{th}} \frac{\partial V_{th}}{\partial T_{line}} + \frac{\partial \dot{m}}{\partial \rho_{th}} \frac{\partial \rho_{th}}{\partial T_{line}}$	-0.170×10^{-3}	[kg · s/K]
	$\frac{\partial \dot{m}}{\partial p} = \frac{\partial \dot{m}}{\partial V_{th}} \frac{\partial V_{th}}{\partial p} + \frac{\partial \dot{m}}{\partial \rho_{th}} \frac{\partial \rho_{th}}{\partial p}$	0.280×10^{-6}	[s/m]
	$\frac{\partial \dot{m}}{\partial d_{line}} = \frac{\partial \dot{m}}{\partial V_{th}} \frac{\partial V_{th}}{\partial d_{line}}$	-0.230×10^0	[kg/s · m]
\dot{m}_t	$\frac{\partial \dot{m}_t}{\partial \dot{m}_o} = 1$	1	[kg · s ⁻¹ /kg · s ⁻¹]
	$\frac{\partial \dot{m}_t}{\partial \dot{m}_f} = 1$	1	[kg · s ⁻¹ /kg · s ⁻¹]
C_{exp}^*	$\frac{\partial C_{exp}^*}{\partial p_k} = \frac{f_p A_t f_{TR}}{\dot{m}_t}$	0.240×10^{-3}	[m ² · s/kg]
	$\frac{\partial C_{exp}^*}{\partial A_t} = \frac{p_k f_p f_{TR}}{\dot{m}_t}$	0.205×10^6	[1/s]
	$\frac{\partial C_{exp}^*}{\partial \dot{m}_t} = -\frac{p_k f_p A_t f_{TR}}{\dot{m}_t^2}$	-0.190×10^5	[m/kg]

quantified and eliminated.

Errors due to data reduction techniques included, for example, the effect of smoothing and linear interpolation of recorded propellant and chamber temperatures or calculated thermal properties. In the case of propellant flow rate computation, errors are inevitably present if two-phase flow develops in the line. Whenever two-phase flow upstream of the venturi exists, only such thermodynamic properties as pressure and temperature are not sufficient to characterize the flow and knowledge of the vapour quality is needed. Figure D.1 presents typical signal traces obtained during an early test for both venturi meters. Pressure oscillations in the LO₂ venturi meter indicate two-phase flow was present. Appropriate venting of the lines and permanent liquid nitrogen cooling flow through the venturi meter jackets was conducted prior to and during data taking in order to maintain propellants in subcooled conditions. Additionally, values of mass flow converted from orifices mounted downstream of the main valves served as backup to the venturi meters. Values from venturi and orifice flow meters agreed to within $\pm 4\%$ of one another.

E.1.2. Discharge Coefficient from Cold-Flow Tests

The general procedure for computing the discharge coefficient from cold-flow tests is presented. The procedure applies, with minor modifications, to injectors components, orifices and venturi meters. Generally, the discharge coefficient is determined by rearranging Equation (E.14):

$$C_d = \frac{\dot{m}}{A\sqrt{2\rho\Delta p}}. \quad (\text{E.14})$$

hence, the error of this measurement is:

$$\delta C_d = \sqrt{\delta C_{d\dot{m}}^2 + \delta C_{dA}^2 + \delta C_{d\rho}^2 + \delta C_{d\Delta p}^2}. \quad (\text{E.15})$$

The mass flow uncertainty is essentially a function of the meter discharge coefficient, error in density and pressure drop. So the mass flow error in the discharge coefficient is:

$$\delta C_{d\dot{m}} = \left[\frac{1}{2A} \frac{\sqrt{2}}{[\rho\Delta p]^{(\frac{1}{2})}} \right] \delta \dot{m}. \quad (\text{E.16})$$

The error in the flow area is:

$$\delta C_{dA} = \left[\frac{-\dot{m}}{2A^2} \frac{\sqrt{2}}{[\rho\Delta p]^{(\frac{1}{2})}} \right] \delta A. \quad (\text{E.17})$$

The error in the density:

$$\delta C_{d\rho} = \left[\frac{-\dot{m}}{4A} \frac{\sqrt{2}}{[\rho\Delta p]^{(\frac{3}{2})}} \Delta p \right] \delta \rho. \quad (\text{E.18})$$

Finally, the error in the pressure drop measurement:

$$\delta C_{d\Delta p} = \left[\frac{-\dot{m}}{4A} \frac{\sqrt{2}}{[\rho\Delta p]^{(\frac{3}{2})}} \rho \right] \delta\Delta p. \quad (\text{E.19})$$

For the particular case of injector calibration, the pressure drop was assumed to be approximately equal to the injection pressure, i.e. $\Delta p \cong p_{\text{in}}$.

Table E.2 shows typical quantities and error involved in the computation of venturi meter discharge coefficient.

Table E.2.: Typical Quantities and Error of Venturi Meter C_d Measurement.

Quantity	Typical Value	Error (%)
Water mass flow rate, [kg/s]	0.106	± 3
Venturi throat diameter d_{th} , [mm]	2.50	± 1
Water density ρ , [kg/m ³]	997.95	± 0.5
Pressure drop Δp , [MPa]	0.240	± 2
Discharge coefficient C_d , [-]	0.988	± 11

F. Test Instrumentation

F.1. Hot-Fire Test Instrumentation

Table F.1.: Instrumentation list.

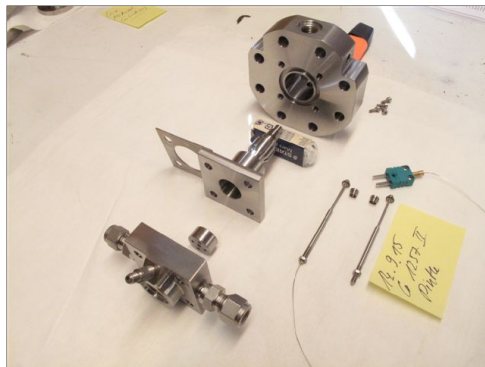
System	Parameter	I.D.	Range	Location	Comment
LO ₂	Tank pressure	PGOXTK	0-350 [barg]	LOX liquefier	First Sensor SQ286, 4-20 [mA]
	Venturi upstream pressure	PLOXUV	0-70 [barg]	Mounting block	First Sensor SQ286, 4-20 [mA]
	Venturi differential pressure	DPLOXV	0-5 [bar]	Venturi meter	Omega PD-23-C, 4-20 [mA]
	Venturi downstream pressure	PLOXDV	0-50 [barg]	Mounting block	First Sensor SQ286, 4-20 [mA]
	Injection pressure	PLOXINJ	0-1000 [psia]	LOX Dome	Omega PX1005L1, 0-10 [V]
	Igniter feed-pressure	GOXIGN	0-70 [barg]	GOX feed-line	First Sensor SQ286, 4-20 [mA]
	Tank outlet temperature	TLOXTK	73.15-313.15 [K]	Mounting block	Thermocouple, type T
	Venturi upstream temperature	TLOXUV	73.15-313.15 [K]	Mounting block	Thermocouple, type K
	Venturi downstream temperature	TLOXDV	73.15-313.15 [K]	Mounting block	Thermocouple, type K
	Injection temperature	TLOXINJ	73.15-313.15 [K]	LOX Dome	Thermocouple, type K
LCH ₄	Tank pressure	PGCH4TK	0-250 [barg]	Run-tank	Wika A-10, 0-10 [V]
	Liquefier LN ₂ bath pressure	PLN2LCH4TK	0-25 [barg]	LCH ₄ liquefier	Wika A-10, 0-10 [V]
	Venturi upstream pressure	PLCH4UV	0-100 [barg]	Mounting block	Wika A-10, 4-20 [mA]
	Venturi differential pressure	DPLCH4V	0-5 [bar]	Venturi meter	Omega PD-23-C, 4-20 [mA]
	Venturi downstream pressure	PLCH4DV	0-60 [barg]	Mounting block	Wika A-10, 4-20 [mA]
	Injection pressure	PLCH4INJ	0-1000 [psia]	LCH ₄ manifold	Omega PX1005L1, 0-10 [V]
	Igniter feed-pressure	GCH4IGN	0-100 [barg]	GCH ₄ feed-line	Wika A-10, 4-20 [mA]
	Tank outlet temperature	TLCH4TK	73.15-313.15 [K]	Mounting block	Thermocouple, type T
	Venturi upstream temperature	TLCH4UV	73.15-313.15 [K]	Mounting block	Thermocouple, type K
	Venturi downstream temperature	TLCH4DV	73.15-313.15 [K]	Mounting block	Thermocouple, type K
	Injection temperature	TLCH4INJ	73.15-313.15 [K]	LCH ₄ manifold	Thermocouple, type K
LN ₂ bath temperature	TLN2LCH4	73.15-313.15 [K]	LCH ₄ liquefier	Thermocouple, type K	
Chamber	Static pressure	PK1.060	0-100 [barg]	169.5 [mm], 60°	Wika A-10, 0-10 [V]
	Static pressure	PK2.180	0-100 [barg]	169.5 [mm], 180°	Wika A-10, 0-10 [V]
	Static pressure	PK3.060	0-100 [barg]	96.75 [mm], 60°	Wika A-10, 0-10 [V]
	Static pressure	PK4.180	0-60 [barg]	96.75 [mm], 180°	Wika A-10, 0-10 [V]
	Static pressure	PK5.060	0-100 [barg]	55.25 [mm], 60°	Wika A-10, 0-10 [V]

Table F.1.: Instrumentation list.(continued)

System	Parameter	I.D.	Range	Location	Comment
Chamber	Static pressure	PK6.180	0-60 [barg]	55.25 [mm], 180°	PLC/DAQ Wika A-10, 0-10 [V]
	Surface temperature	TS1.180	233.15-1023.15 [K]	96.75 [mm], 180°	Thermocouple, type J
	Surface temperature	TS2.180	233.15-1023.15 [K]	79.75 [mm], 180°	Thermocouple, type J
	Surface temperature	TS3.180	233.15-1023.15 [K]	55.25 [mm], 180°	Thermocouple, type J
	Inner-wall temperature	TC1.060	233.15-1273.15 [K]	169.50 [mm], 60°	Thermocouple, type K
	Inner-wall temperature	TC2.180	233.15-1273.15 [K]	169,50 [mm], 180°	Thermocouple, type K
	Inner-wall temperature	TC3.300	233.15-1273.15 [K]	169.50 [mm], 300°	Thermocouple, type K
	Inner-wall temperature	TC4.060	233.15-1273.15 [K]	133,50 [mm], 60°	Thermocouple, type K
	Inner-wall temperature	TC5.120	233.15-1273.15 [K]	133.50 [mm], 120°	Thermocouple, type K
	Inner-wall temperature	TC6.300	233.15-1273.15 [K]	133.50 [mm], 300°	Thermocouple, type K
	Inner-wall temperature	TC7.000	233.15-1273.15 [K]	79.75 [mm], 0°	Thermocouple, type K
	Inner-wall temperature	TC8.120	233.15-1273.15 [K]	79.75 [mm], 120°	Thermocouple, type K
	Inner-wall temperature	TC9.240	233.15-1273.15 [K]	79.75 [mm], 240°	Thermocouple, type K
	Inner-wall temperature	TC10.000	233.15-1273.15 [K]	55.25 [mm], 0°	Thermocouple, type K
Inner-wall temperature	TC11.120	233.15-1273.15 [K]	55.25 [mm], 120°	Thermocouple, type K	
Inner-wall temperature	TC12.240	233.15-1273.15 [K]	55.25 [mm], 240°	Thermocouple, type K	
General	Igniter chamber pressure	PK.IGN	0-100 [barg]	Igniter	Wika A-10, 0-10 [V]
	Faceplate chamber pressure	PK.FCP	0-100 [barg]	Fire bottom	Wika A-10, 0-10 [V]
	Pintle tip temperature	TPINTLE	233.15-1273.15 [K]	Pintle tip	Thermocouple, type K

G. Injector Hardware

G.1. Injector hardware



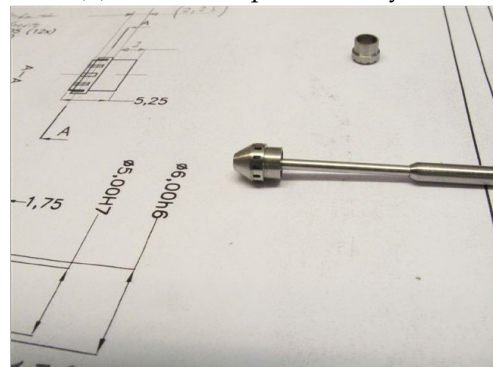
(a) Injector assembly.



(b) Thermocouple assembly.



(c) Detail of pintle tip.



(d) Pintle tip and orifices.

Figure G.1.: Pintle injector hardware.

Bibliography

- [1] I. A. Klepikov, B. I. Katorgin, and V. K. Chvanov, "The New Generation of Rocket Engines, Operating by Ecologically Safe Propellant Liquid Propellant and Liquefied Natural Gas Methane," *Acta Astronautica*, vol. 41, no. 4, pp. 209–217, 1997.
- [2] C. O'Brien and R. L. Ewen, "Advanced Oxygen-Hydrocarbon Rocket Engine Study," Aerojet Liquid Rocket Company, NASA CR-161748, 1981.
- [3] G. F. Orton, T. D. Mark, and D. D. Weber, "LOX/Hydrocarbon Auxiliary Propulsion System Study," McDonnell Douglas Astronautics Company, NASA CR-171656, 1982.
- [4] L. Schoenman, "Low-thrust ISP Sensitivity Study," Aerojet Liquid Rocket Company, NASA CR-165621, 1982.
- [5] S. R. Hirshorn, Linda, V. D. and Linda, K. B., *NASA Systems Engineering Handbook*, NASA SP-2016-6105 Rev 2., Washington, D.C., 2017.
- [6] D. Todd, "SpaceX's Mars Rocket to be Methane-Fuelled," *Flight Global*, November 2012.
- [7] J. Wesley, T. Tomsik, T. Smudde, A. Schnell, and M. Femminineo, "A Densified Liquid Methane Delivery System for the Altair Ascent Stage," in *Spaceops Conference*, AIAA 2010-1904, 2010.
- [8] A. A. Kozlov, I. A. Bazanova, G. E. M., Chugaev, and C. M. Krishna, "Development of Liquid Rocket Engines of Small Thrust on Ecological Clean Propellants," Moscow Aviation Institute, 2002.
- [9] G. F. Orton and T. D. Mark, "LOX/Hydrocarbon Auxiliary Propulsion for the Space Shuttle Orbiter," *Spacecraft and Rockets*, vol. 21, no. 6, pp. 580–586, 1984.
- [10] J. A. Martin, "Hydrocarbon Rocket Engines for Earth-to-Orbit Vehicles," *Spacecraft and Rockets*, vol. 20, no. 3, pp. 249–256, 1983.
- [11] S. Zurbach, J. Thomas, Vuillermoz, L. Vingert, and M. Habiballah, "Recent Advances on LOX/Methane Combustion for Liquid Rocket Engine Injector," in *38th AIAA/ASME/SAE/ASEE Joint Propulsion Conference & Exhibit*, Indianapolis, Indiana, July 2002.
- [12] T. D. Smith, M. D. Klem, and K. L. Fisher, "Propulsion Risk Reduction Activities for Nontoxic Cryogenic Propulsion," Glenn Research Center, Cleveland, Ohio, NASA TM-2010-216820, October 2010.
- [13] J. C. Melcher and J. K. Allfred, "Liquid Oxygen / Liquid Methane Test Results of the RS-18 Lunar Ascent Engine at Simulated Altitude Conditions at NASA White Sands

- Test Facility," in *45th AIAA/ASME/SAE/ASEE Joint Propulsion Conference and Exhibit*, AIAA 2009-4949, Denver, Colorado, August 2009.
- [14] G. P. Sutton, *History of Liquid Propellant Rocket Engines*, AIAA, Reston, Virginia, 2006.
- [15] M. J. Casiano, J. R. Hulka, and V. Yang, "Liquid-Propellant Rocket Engine Throttling: A Comprehensive Review," in *45th AIAA/ASME/SAE/ASEE Joint Propulsion Conference & Exhibit*, AIAA 2009-5135, 2009.
- [16] G. Dressler, "Summary of Deep Throttling Rocket Engines with Emphasis on Apollo LMDE," in *42nd AIAA/ASME/SAE/ASEE Joint Propulsion Conference & Exhibit*, AIAA 2006-5220, 2006.
- [17] D. E. Sokolowski, N. P. Hannum, and E. J. Seigwarth, "Some Aspects of FLOX-Methane Rocket Engine Throttling," Cleveland, Ohio, NASA TM X-3094, 1974.
- [18] E. M. Betts, "Determination of a New Throttling Liquid Rocket Engine for a Mars Lander," Master's thesis, The University of Alabama in Huntsville, 2011.
- [19] V. G. Bazarov, "Throttleable Liquid Propellant Engines Swirl Injectors for Deep Smooth Thrust Variations," in *30th AIAA/ASME/SAE/ASEE Joint Propulsion Conference*, AIAA 94-2978, June 1994.
- [20] D. W. Harvey, "Throttling Venturi Valves for Liquid Rocket Engines," in *AIAA 6th Propulsion Joint Specialist Conference*, AIAA 70-703, June 15-19 1970.
- [21] D. R. Baker, "Inert Calibration of Deep-Throttling Bipropellant Rocket Engines," *Journal of Spacecraft and Rockets*, vol. 5, no. 5, p. 6, 1968.
- [22] D. E. Welton, M. S. Bensky, and J. Hiland, "Variable-Thrust Liquid Propellant Rocket Engines," in *AIAA Summer Meeting*, AIAA 63-268, Los Angeles, California, June 17-20 1963.
- [23] M. W. Cardullo and F. R. Rickerson, "Variable Thrust Rocket Engines," in *Liquid Rockets and Propellants*, U.S. Naval Air Rocket Test Station, Liquid Rocket Propulsion Laboratory, 1960.
- [24] L. Carey, "Dual-Mode, 100:1 Thrust Modulation Rocket Engine," *Journal of Spacecraft and Rockets*, vol. 5, no. 2, p. 5, 1967.
- [25] S. A. Whitmore, Z. W. Peterson, and S. D. Eilers, "Closed-Loop Precision Throttling of a Hybrid Rocket Motor," *Journal of Propulsion and Power*, vol. 30, no. 2, pp. 325-336, March-April 2014.
- [26] G. N. Abramovich, *The Theory of Swirl Atomizers*, Industrial Aerodynamics, BNT ZAGI, Moscow, 1944.
- [27] G. Taylor, "The Mechanism of Swirl Atomizers," in *Proceedings of the 7th International Congress for Applied Mechanics*, vol. 2, London, 1948.

-
- [28] J. J. Chinn, "An Appraisal of Swirl Atomizer Inviscid Flow Analysis, Part 1: The Principle of Maximum Flow for a Swirl Atomizer and its Use in the Exposition and Comparison of Early Flow Analyses," *Journal of Atomization and Sprays*, vol. 19, issue 3, pp. 263–282, 2009.
- [29] J. J. Chinn, "An Appraisal of Swirl Atomizer Inviscid Flow Analysis, Part 2: Inviscid Spray Cone Angle Analysis and Comparison of Inviscid Methods with Experimental Results for Discharge Coefficient, Air Cone Radius, and Spray Cone Angle," *Atomization and Sprays*, vol. 19, issue 3, pp. 283–308, 2009.
- [30] Y. I. Khavkin, *Swirl Injectors*. Mashinostroyeniye Press, Moscow, 1976.
- [31] V. D. Kurpatenkov and J. V. Kessaev, *Design of Engine Injectors (in Russian)*, Moscow Aviation Institute, Moscow, 1987.
- [32] M. V. Dobrovolski, *Liquid Propellant Rocket Engines, Preliminary Design (in Russian)*, 2nd ed., MGTY, Moscow, 2005.
- [33] V. G. Bazarov, V. Yang, and P. Puri, *Design and Dynamics of Jet and Swirl Injectors, Chapter 2 of Liquid Rocket Thrust Chambers: Aspects of Modeling, Analysis and Design*, AIAA Progress in Astronautics and Aeronautics, vol. 200, Virginia, 2004.
- [34] L. Bayvel and Z. Orzechowski, *Liquid Atomization*. Taylor & Francis, Washington, DC, 1993.
- [35] M. R. Long, W. E. Anderson, and R. W. Humble, "Bi-Centrifugal Swirl Injector Development for Hydrogen Peroxide and Non-Toxic Hypergolic Miscible Fuels," in *38th AIAA/ASME/SAE/ASEE Joint Propulsion Conference and Exhibit*, AIAA 2002-4026, Indianapolis, Indiana, 2002.
- [36] M. R. Long, "Swirl Injectors for Oxidizer-Rich Staged Combustion Cycle Engines and Hypergolic Propellants," Ph.D. dissertation, Purdue University, West Lafayette, Indiana, August 2004.
- [37] R. J. Kenny, J. R. Hulka, M. D. Moser, and N. O. Rhys, "Effect of Chamber Backpressure on Swirl Injector Fluid Mechanics," in *Joint Propulsion Conference*. AIAA, Huntsville, Alabama, 2008.
- [38] M. Sasaki, H. Sakamoto, M. Takahashi, and T. Tomita, "Comparative Study of Recessed and Non-recessed Swirl Coaxial Injectors," in *33rd Joint Propulsion Conference and Exhibit, Joint Propulsion Conferences*, Seattle, 1997.
- [39] P.-G. Han, J. Seol, S. Hwang, and Y. Yoon, "The Spray Characteristics of Swirl Coaxial Injectors," in *41st Aerospace Sciences Meeting and Exhibit*, AIAA 2003-490, Reno, Nevada, January 2003.
- [40] D. Kim, P. Han, J.-H. Im, Y. Yoon, and V. G. Bazarov, "Effect of recess on the spray characteristics of liquid-liquid swirl coaxial injectors," *Journal of Propulsion and Power*, vol. 23, no. 6, pp. 1194–1203, November-December 2007.

- [41] T. Inamura and K. Miyata, "Spray Characteristics of Swirl Coaxial Injector and Its Modeling," in *37th AIAA/ASME/SAE/ASEE Joint Propulsion Conference and Exhibit*, AIAA 2001-3570, Salt Lake City, Utah, 2001.
- [42] A. R. Ramezani and A. Ghafourian, "Spray Angle Variation of Liquid-Liquid Swirl Coaxial Injectors," in *41st AIAA/ASME/SAE/ASEE Joint Propulsion Conference and Exhibit*, AIAA 2005-3747, Tucson, Arizona, 2005.
- [43] D. Kim, J.-H. Im, H. Koh, and Y. Yoon, "Effect of Ambient Gas Density on Spray Characteristics of Swirling Liquid Sheets," *Journal of Propulsion and Power*, vol. 23, no. 3, pp. 603–611, 2007.
- [44] S. Moon, C. Bae, and E. Abo-Serie, "Estimation of the Breakup Length for a Pressure-Swirl Spray from the Experimentally Measured Spray Angle," *Journal of Atomization and Sprays*, vol. 19, issue 3, pp. 235–246, 2009.
- [45] V. G. Bazarov and V. Yang, "Liquid Propellant Rocket Engine Injector Dynamics," *Journal of Propulsion and Power*, vol. 14, no. 5, pp. 797–806, 1998.
- [46] J.-H. Im, D. Kim, P. Han, Y. Yoon, and V. G. Bazarov, "Self-Pulsation Characteristics of a Gas-Liquid Swirl Coaxial Injector," *Journal of Atomization and Sprays*, vol. 19, issue 1, pp. 57–74, 2009.
- [47] V. G. Bazarov and B. Kartsev, "New Injector Conception of Low Thrust Liquid Rocket Engine for Spacecraft," in *Proceedings of the Second European Spacecraft Propulsion Conference*, no. 398, Noordwijk, The Netherlands, May 1997.
- [48] J. Calvignac, L. Dang, T. L. Tramel, and L. Passeur, "Design and Testing of Non-Toxic RCS Thrusters for Second Generation Reusable Launch Vehicle," in *39th AIAA/ASME/SAE/ASEE Joint Propulsion*, AIAA 2003-4922, Huntsville, Alabama, July 2003.
- [49] M. J. Bedard, T. W. Feldman, A. Rettenmaier, and W. Anderson, "Student Design/Build/Test of a Throttlable LOX-LCH₄ Thrust Chamber," in *48th AIAA/ASME/SAE/ASEE Joint Propulsion Conference & Exhibit*, AIAA 2012-3883, Atlanta, Georgia, August 2012.
- [50] G. Dressler and J. Bauer, "TRW Pintle Engine Heritage and Performance Characteristics," in *36th AIAA/ASME/SAE/ASEE Joint Propulsion Conference and Exhibit*, AIAA-2000-3871, Redondo Beach, CA, July 2000.
- [51] B. Austin, S. D. Heister, and W. E. Anderson, "Characterization of Pintle Engine Performance for Nontoxic Hypergolic Bipropellants," *Journal of Propulsion and Power*, vol. 21, no. 4, pp. 627–635, July-August 2005.
- [52] J. Gromski, A. Majamaki, S. Chianese, V. Weinstock, and K. T., "Northrop Grumman TR202 LOX/GH₂ Deep Throttling Engine Project Status," in *46th AIAA/ASME/SAE/ASEE Joint Propulsion Conference & Exhibit*, AIAA 2010-6725, Nashville, July 25-28 2010.
- [53] R. D. Ingebo, "Gas Density Effect on Dropsizes of Simulated Fuel Sprays," in *25th Joint Propulsion Conference*, NASA TM-102013, Monterey, California, July 1989.

-
- [54] W. O. Mayer, A. H. Schik, B. Vielle, C. Chauveau, I. Gökalp, D. G. Talley, and R. D. Woodward, "Atomization and Breakup of Cryogenic Propellants Under High-Pressure Subcritical and Supercritical Conditions," *Journal of Propulsion and Power*, vol. 14, no. 5, pp. 835–842, September-October 1998.
- [55] R. J. Kenny, M. D. Moser, J. R. Hulka, and J. G., "Cold Flow Testing for Liquid Propellant Rocket Injector Scaling and Throttling," in *42nd AIAA/ASME/SAE/ASEE Joint Propulsion Conference and Exhibit*, AIAA 2006-4705, Sacramento, California, 2006.
- [56] R. Woodward, K. Miller, V. Bazarov, G. Guerin, and R. S. S. Pal, "Injector Research for Shuttle OMS Upgrade using LOX/Ethanol Propellants," in *34th AIAA/ASME/SAE/ASEE Joint Propulsion Conference and Exhibit*, AIAA 98-3816, Cleveland, 1998.
- [57] M. J. Locke, S. Pal, R. D. Woodward, and R. J. Santoro, "High Speed Visualization of LOX/GH2 Rocket Injector Flowfield: Hot-fire and Cold-Flow Experiments," in *46th AIAA/ASME/SAE/ASEE Joint Propulsion Conference & Exhibit*, AIAA 2010-7145, Nashville, 2010.
- [58] J. Lux and O. Haidn, "Flame Stabilization in High-Pressure Liquid Oxygen/Methane Rocket Engine Combustion," *Journal of Propulsion and Power*, vol. 25, no. 1, p. 15–23, January-February 2009.
- [59] J. Lux and O. J. Haidn, "Effect of Recess in High-Pressure Liquid Oxygen/Methane Coaxial Injection and Combustion," *Journal of Propulsion and Power*, vol. 25, no. 1, pp. 24–32, January-February 2009.
- [60] V. G. Bazarov, "New Class of Porous Injectors for Combustion Chambers and Gas Generators," in *29th AIAA/SAE/ASME/ASEE Joint Propulsion Conference and Exhibit*, AIAA 93-1955, Monterey, June 1993.
- [61] S. A. Striepe, D. W. Way, A. M. Dwyer, and J. Balaram, "Mars Science Laboratory Simulations for Entry, Descent and Landing," *Journal of Spacecraft and Rockets*, vol. 43, no. 2, pp. 311–323, 2006.
- [62] R. S. Baker, A. R. Casillas, C. S. Guernsey, and J. M. Weiss, "Mars Science Laboratory Descent-Stage Integrated Propulsion Subsystem: Development and Flight Performance," *Journal of Spacecraft and Rockets*, vol. 51, no. 4, pp. 1217–1226, 2014.
- [63] J. Gamble, "JSC Pre-Phase A: Study of a Mars Sample Return Mission, Aerocapture, Entry and Landing," NASA CR-23230, 1989.
- [64] A. A. Kozlov, *Liquid rocket engine feed-system choice and main parameters for preliminary design purposes (in Russian)*, Moscow Aviation Institute, Moscow, 1997.
- [65] F. I. Barbosa and M. Niwa, "Estudo Preliminar para Determinacao dos Parametros Principais de um Propulsor Liquido para o Quarto Estagio do VLS-1 (in Portuguese)," IAE, IAE/APE, Technical Report RT 010/ASE/02, October 2002, confidential.
-

- [66] D. C. Morrissey, "Historical Perspective: Viking Mars Lander Propulsion," *Journal of Propulsion and Power*, vol. 8, no. 2, pp. 320–331, 1992.
- [67] J. G. Campbell, D. R. Batha, M. D. Carey, A. R. Nagy, and R. C. Stechman, "Thrust Chamber Cooling Techniques for Spacecraft Engines, Volume 1," The Marquardt Corporation, 1963.
- [68] S. Gordon and B. J. McBride, "Computer Program for Calculation of Complex Chemical Equilibrium Compositions and Applications," NASA Reference Publication 1311, 1996.
- [69] E. W. Lemmon, M. L. Huber, and M. O. McLinden, "NIST Standard Reference Database 23: Reference Fluid Thermodynamic and Transport Properties-REFPROP, Version 9.1, National Institute of Standards and Technology," 2013. Online Available: <https://www.nist.gov/srd/refprop>
- [70] K. W. Gross and S. A. Evans, *JANNAF Rocket Engine Performance Test Data Acquisition and Interpretation Manual*, CPIA Publication 245, 1975.
- [71] L. S. Bender, V. J. Sarli, and B. W. G., "Kinetic Performance Handbook," United Aircraft Research Laboratories, NASA-CR-72601, 1970.
- [72] V. D. Kurpatenkov and J. V. Kessaev, *Design of Liquid Rocket Propellant Engine Chambers (in Russian)*. Moscow Aviation Institute, Moscow, 1993.
- [73] *Atlas of Construction of Liquid Propellant Rocket Engines (in Russian)*, undisclosed authors, confidential. Moscow Aviation Institute, Moscow, 1969.
- [74] V. D. Kurpatenkov, *Calculation of Bell-Shaped Nozzle Profiles (in Russian)*. Moscow Aviation Institute, Moscow, 1975.
- [75] D. K. Huzel and D. H. Huang, *Modern Engineering for Design of Liquid Propellant Rocket Engines*, AIAA Progress in Astronautics and Aeronautics, no. 147, 1992.
- [76] M. Barrere, A. Jaumotte, B. Veubeke, and J. Vandekerckhove, *Rocket Propulsion*. Elsevier Publishers Company, Amsterdam, 1960.
- [77] R. S. Gross, "Combustion Performance and Heat Transfer Characterization of LOX/Hydrocarbon Type Propellants," 1980, Task I Data Dump, Aerojet Liquid Rocket Company.
- [78] S. Omori, K. W. Gross, and A. Krebsbach, "Wall Temperature Distribution Calculation for a Rocket Nozzle Contour," NASA TN D-6825, 1972.
- [79] A. P. Vasiliev, V. M. Kurpatenkov, V. A. Kuznetsov, V. D. Kurpatenkov, A. M. Obelnitsky, V. M. Poliaev, and B. I. Poliaev, *Ochnoviy Teori y racheta GRD (in Russian)*, vol. 1. Moskwa Vischkaia Skola, Moscow, 1993.
- [80] R. T. Cook, "Methane Heat Transfer Investigation," Rocketdyne Division, Rockwell International Corporation, 1984.

-
- [81] R. G. Spencer and D. C. Rousar, "Supercritical Oxygen Heat Transfer," NASA CR-135339, 1977.
- [82] H. Ito, "Friction Factors for Turbulent Flow in Curved Pipes," *Journal of Basic Engineering*, vol. 81, p. 123, 1959.
- [83] F. Bouillon, "Oxidation of Copper and the Solubility of Oxygen in the Metal," *Acta Metallurgica*, vol. 10, no. 7, pp. 647–652, 1962.
- [84] Crane, *Flow of Fluids Through Valves, Fittings and Pipe (Technical Paper No. 410M)*, Metric Edition ed., Crane Valves North America, The Woodlands, 1999.
- [85] R. C. Stechman, J. Oberstone, and J. C. Howell, "Design Criteria for Film Cooling for Small Liquid-Propellant Rocket Engines," *Journal of Spacecraft and Rockets*, vol. 6, no. 2, pp. 97–102, February 1969.
- [86] G. R. Kinney, A. E. Abramson, and J. L. Sloop, "Internal-liquid-film-cooling Experiments with Air-stream Temperatures to 2000 degrees F. in 2- and 4-inch-diameter Horizontal Tubes," NACA-TR-1087, 1952.
- [87] J. G. Campbell, D. R. Batha, M. D. Carey, A. R. Nagy, and R. C. Stechman, "Thrust Chamber Cooling Techniques for Spacecraft Engines, Volume 2," The Marquardt Corporation, 1963.
- [88] A. J. Pavil, "Design and Evaluation of High Performance Rocket Engine Injectors for Use with Hydrocarbon Fuels," NASA TM-79319, 1979.
- [89] G. W. Howell and T. M. Weathers, "Aerospace Fluid Component Designers' Handbook. Volume 1, Revision D," TRW RPL-TDR-64-25, February 1970.
- [90] F. Merrit and L. Dumont, "Supplemental Report - Wide Range Flow Control Program," Air Force Rocket Propulsion Laboratory, Edwards Air Force Base, AFRPL-TR-69-141, 1969.
- [91] T. D. Harrje and F. H. Reardon, *Liquid Propellant Rocket Combustion Instability*, NASA SP-194, Cleveland, Ohio, January 1972.
- [92] V. V. Mikhailov and V. G. Bazarov, *Throttled Liquid Rocket Engines (in Russian)*. Mashinostroenie, Moscow, 1985.
- [93] G. Morrel, "Rocket Thrust Variation with Foamed Liquid Propellants," NACA-RM-E56K27, Washington D.C., February 1957.
- [94] A. A. Kozlov, J. N. Hinckel, J. Koreeda, and A. Comiran, "Payload Evaluation of a Tripropellant Carrier Rocket," *Journal of Propulsion and Power*, vol. 15, no. 2, pp. 304–309, 1999.
- [95] G. W. Howell and T. M. Weathers, "Aerospace Fluid Component Designers' Handbook. Volume 2, Revision D.," TRW RPL-TRD-64-25 (AD874543), February 1970.

Bibliography

- [96] A. I. Edelman, *Propellant Valves of Liquid-propellant Rocket Engines*. Foreign Technology Division, FTD-MT-24-1463-71, Air Force Systems Command, U.S. Air Force, 1970.
- [97] "Space Vehicle Design Criteria, Liquid Rocket Engine Injectors (SP-8089)," NASA SP-8089, Cleveland, Ohio, 1976.
- [98] R. W. Hammock, C. E. Currie, and E. A. Fisher, "Apollo Experience Report-Descent Propulsion System," Washington, D.C., NASA TN D-7143, March 1973.
- [99] G. W. Elverum, "Variable Thrust Bipropellant Rocket Engine," United States of America Patent 3,205,656, September 14, 1965.
- [100] W. A. Tomazic, "Rocket-engine Throttling," NACA RM E55J20, Cleveland, Ohio, 1955.
- [101] G. B. Siniarev and M. V. Dobrovolski, *Liquid Propellant Rocket Engines, Theory and Design (in Russian)*, 2nd ed., Moscow, 1955.
- [102] V. Yang and W. Anderson, *Liquid Rocket Engine Combustion Instability*, AIAA Progress in Astronautics and Aeronautics, no. 169, Washington, DC, 1995.
- [103] A. H. Lefebvre, *Atomization and Sprays*, Combustion Series, Taylor & Francis, New York, 1989.
- [104] S. N. Kazuki, M. Tsue, R. Kanai, K. Suzuki, T. Inagawa, and T. Hiraiwa, "Performance Evaluation of Rocket Engine Combustors using Ethanol/Liquid Oxygen Pintle Injector," in *Propulsion and Energy Forum, 52nd AIAA/SAE/ASEE Joint Propulsion Conference*, AIAA 2016-5080, Salt Lake City, 2016.
- [105] V. Yang, M. Habiballah, J. Hulka, and M. Popp, *Liquid Rocket Thrust Chambers: Aspects of Modeling, Analysis and Design*. AIAA Progress in Astronautics and Aeronautics, vol. 200, Virginia, 2004.
- [106] J. Rupe, "On The Dynamic Characteristics of Free Liquid Jets and a Partial Correlation with Orifice Geometry," Jet Propulsion Laboratory, Pasadena, California, Technical Report 32-207, 1962.
- [107] W. A. Carter and G. S. Bell, "Development and Demonstration of a N_2O_4/N_2H_4 Injector," AFRPL-TR-69-231, TRW Redondo Beach, California, 1969.
- [108] W. A. Carter, "Gas-Liquid Space Storable Propellant Performance," TRW 13462-6001-R0-00, Final Report, TRW Redondo Beach, California, 1970.
- [109] M. Son, K. Yu, K. Radhakrishnan, and J. Koo, "Design Procedure of a Movable Pintle Injector for Liquid Rocket Engines," in *AIAA SciTech, 54th AIAA Aerospace Sciences Meeting*, AIAA 2016-1453, San Diego, California, 2016.
- [110] M. Son, K. Yu, K. Radhakrishnan, B. Shin, and J. Koo, "Verification on Spray Simulation of a Pintle Injector for Liquid Rocket Engine," *Journal of Thermal Science*, vol. 25, no. 1, pp. 90–96, 2016.

- [111] G. Elverum and P. Staudhammer, "The Effect of Rapid Liquid Phase Reactions on Injector Design and Combustion in Rocket Motors," Jet Propulsion Laboratory, Progress Report 30-4, Pasadena, California, August 1959.
- [112] L. Crocco and S. I. Cheng, *Theory of Combustion Instability in Liquid Propellant Rocket Motors*, AGARDograph no. 8, Butterworths Sci. Pub. Ltd., London, 1956.
- [113] G. P. Sutton and O. Biblarz, *Rocket Propulsion Elements*, 7th ed., Wiley, Hoboken, New Jersey, 2001.
- [114] B. B. Vasques and O. J. Haidn, "Uncertainty Analysis as Applicable to a Miniature Cryogenic Test Stand for Rocket Research," in *31st International Symposium on Space Technology and Science*, Matsuyama, Japan, 2017.
- [115] B. Kit and D. S. Evered, *Rocket Propellant Handbook*. The Macmillan Company, New York, 1960.
- [116] K. J. Davidian, "Pretest Uncertainty Analysis for Chemical Rocket Engine Tests," NASA TM-89819, Lewis Research Center, Cleveland, Ohio, 1987.